THE UNIVERSITY OF CHICAGO

HISTOTRIPSY AS AN ADJUVANT THERAPY FOR DEEP VEIN THROMBOSIS

A DISSERTATION SUBMITTED TO

THE FACULTY OF THE DIVISION OF THE BIOLOGICAL SCIENCES

AND THE PRITZKER SCHOOL OF MEDICINE

IN CANDIDACY FOR THE DEGREE OF

DOCTOR OF PHILOSOPHY

COMMITTEE ON MEDICAL PHYSICS

BY

SAMUEL ANDERSON HENDLEY

CHICAGO, ILLINOIS

JUNE 2021

"וָאֶתְּנָה לִבִּי לָדַעַת חָכְמָה וְדַעַת הוֹלֵלוֹת וְשִׂכְלוּת יָדַעְתִּי שֶׁגַּם־זֶה הוּא רַעְיוֹן רוּחַ:"

Ecclesiastes 1:17

Contents

LIST OF FIGURES

LIST OF TABLES

GLOSSARY

CDT (catheter directed thrombolytics): A treatment that uses a catheter to administer therapeutics near the thrombus.

DVT (deep vein thrombosis): A condition where blood clots form in the large vessels of the body.

Fibrin: A protein which serves as the main structural scaffolding of clot tissue.

Erythrocyte: Also known as red blood cells, these cells are present in blood and are responsible for delivering oxygen. When ruptured, they release hemoglobin.

FDP (fibrin degradation product): Debris fragments that are formed when the fibrin mesh is lysed. The smallest fibrin degradation product is D-dimer.

PCI (passive cavitation imaging): An imaging technique that spatially maps the power of acoustic emissions generated by the bubble cloud.

PE (pulmonary embolism): A condition where a portion of a blood clot obstructs the pulmonary artery.

Platelet: Cells that expedite the formation of clots.

rt-PA (recombinant tissue plasminogen activator): A commonly used thrombolytic.

Thrombolytic: A drug which breaks apart the structure of a clot, typically by expediting the breakdown of the fibrin mesh within the clot.

VEGF (Vascular endothelial growth factor): A protein which helps stimulate the genesis of new blood vessels.

VTE (venous thromboembolism): An umbrella term for vascular occlusions which encompasses deep vein thrombosis and pulmonary embolism.

ACKNOWLEDGMENTS

"No man is an island entire of itself"

I would like to thank my advisor, Dr. Kenneth Bader, for his mentorship. He is unwavering and rigorous in his pursuit of science, and is balanced by creativity, curiosity, and commitment to outreach. He has shown me that being a good scientist and being a good person are not mutually exclusive. I also would like to thank the members of my thesis committee: Dr. Zheng Feng Lu, Dr. Jonathan Paul, Dr. Patrick La Riviere, and Dr. Steffen Sammet. In addition to providing invaluable insight into ultrasound techniques, Dr. Lu helped guide me through the path to clinical medical physics. Dr. Paul's expertise as an interventional cardiologist helped ground my research within the reality of clinical possibility. Despite being a successful and busy physician, JP always had the time to answer questions (and crack a few jokes). Dr. La Riviere is one of the most intelligent people I have ever met, and is as likely to teach you about the history of Chicago architecture as he is to teach you the foundations of super-resolution microscopy. His breadth and depth of knowledge helped me find isomorphisms and new approaches in my research. As a physician-scientist, Dr. Sammet helped significantly by bridging the gap between the academic and clinical realms. I could always rely on his honest assessments.

I acknowledge and thank the Human Tissue Resource Center, the Human Immunologic Monitoring Facility (and Yuanyuan Zhang in particular), the University of Chicago Medical Laboratories, Phil Griffin and the Soft Matter Characterization Facility, Elena Solomaha and the Biophysics Core Facility, and David Leclerc and the Cytometry and Antibody Technology facility. This work was supported in part by the National Institutes of Health Grants R01HL133334 and the Paul C. Hodges Alumni Society of the Department of Radiology at the University of Chicago.

I want to offer my special thanks to the many undergraduate workers who have made this work possible. Erin Snoddy helped pave the way for our quantitative histology algorithms, which Danny Mansour was able to complete. Danny's dogged indefatigability coupled with his scientific intuition kept me on my toes! Although this is still in progress, I would be remiss were I not to thank Lily Mansfield, Soo May Wee, Keethan Kommanapalli, and Alexandra "Sasha" Ligay for their work in developing our chronic clot model.

Finally, I wish to thank my family and friends. This has been a process of (literally) blood sweat, and tears, and I could not have done it without their support. I have inherited my dad's grammatical and stylistic proclivities (*utilize* is a useless word; "comprises" or "composed of" but never "comprised of;" and "everything should be written as simply as possible, but no simpler"), but also an appreciation for beauty in the written word. My mom has been a constant source of inspiration, and it's because of her that I have learned to treat everyone with respect, kindness, and grace: "It doesn't matter how smart you are – it matters how you treat other people." In true fraternal form, I will thank my brother for all the good food. And I must thank the community at Living Hope Church, who helped balance the monastic cloister of academia with the spiritual and physical needs of those on Chicago's southside. In the words of a much more capable and puissant physicist than myself, "*Fiat lux*."

ABSTRACT

Deep vein thrombosis encompasses a wide range of morphologies, and a subset of cases require clinical intervention. The current treatment for vessel recanalization, catheter-directed thrombolytics, is effective for acute cases but has a diminished response for chronic disease. An adjuvant approach that is effective for intractable thrombi should therefore improve clinical outcomes. Histotripsy is a focused ultrasound therapy which has been demonstrated to enhance lytic efficacy via the nucleation of bubble clouds in pre-clinical studies. Translating histotripsy from benchtop studies into the clinic is predicated upon three points: 1). The basic mechanism of action should be well characterized, 2) There must be image guidance capable of monitoring the strength and location of the treatment *in situ*, and 3) Outcomes should be improved compared to current treatment methods.

To bridge the gaps identified above, the following aims were executed in this dissertation. In the first aim, the structure and thrombolytic response of ex vivo human venous thrombi were examined to understand the differences between acute and chronic thrombi. Imaging techniques were also tested to gauge sample response to lytic therapy. We found thrombi older than 7 days have substantial changes in the extracellular structure compared younger thrombi (< 7 days old). A positive trend was observed between MR imaging metrics and sample response to thrombolysis.

The second aim of this dissertation tested how medium stiffness, a consideration for heterogeneous thrombi, affects the energy of histotripsy bubble activity necessary to cause ablation. Material stiffness induced minimal changes in bubble dynamics as tracked with acoustic emissions mapped with passive cavitation imaging. Further, a fixed minimal acoustic power was associated with histotripsy liquefaction for media with $E < 142$ kPa.

The third aim of this dissertation examined the mechanisms of clot degradation under the action of histotripsy and systemic administration of thrombolytic. These studies revealed histotripsy bubble activity contributes equally to hemolysis and fibrinolysis. Further, hemolysis and fibrinolysis contribute equally to overall treatment efficacy when employing histotripsy.

Finally, the objective of the fourth aim was to determine how the dose of lytic administration affects the synergy of histotripsy bubble activity. The results of this aim suggest that histotripsy can reduce the lytic dose by tenfold and still cause the same degree of mass loss and fibrinolysis as compared to the current clinical standard. Overall, the work in this thesis shows that histotripsy is an effective adjuvant therapy for deep vein thrombosis. It is my sincere hope that this work will one day help bring this exciting treatment paradigm to the clinic.

CHAPTER 1

INTRODUCTION

1.1 The clinical problem: deep vein thrombosis

Deep vein thrombosis is a condition where portions of the vasculature become obstructed due to coagulation of blood[1], and is a major health issue. Approximately 5% of the United States population (600,000 Americans annually) will experience deep vein thrombosis (DVT) over the course of their lifetime[2], and many DVT cases go undiagnosed[3]. Venous obstruction is associated with significant morbidity, and over 80% of all pulmonary embolisms (PE) are caused by DVT[4]. Thrombi form due to the confluence of innate hypercoagulability, vessel wall damage, and slow blood flow or even stasis[6]. Variability in clotting etiology results in heterogeneity in thrombosis with respect to composition, stiffness, size, and thrombolytic susceptibility (Figure 1.1 and Figure 1.2)[7]. Age is a significant factor in the degree of heterogeneity, and different thrombi may require different therapeutic approaches.

Figure 1.1: Gross comparison of chronic (left) and acute (right) thrombi. The chronic thrombus is white and stiff, but the acute thrombus is red and loose.

Figure 1.2: Clot sample extracted from a patient. Large clots are a significant vascular burden and may require clinical intervention.

1.2 Current treatments for deep vein thrombosis

The standard of care for non-life-threatening acute DVT is anticoagulant therapy, such as heparin followed by oral anticoagulants[8,9]. Although this technique halts further thrombus growth and reduces the risk of recurrent DVT, it does not actively remove the thrombus nor does it avert post-thrombotic syndrome[4]. One treatment that has proven successful in reducing thrombus burden is the administration of thrombolytic therapy. This approach actively promotes the lysis of fibrin networks within thrombi[10]. Recombinant tissue plasminogen activator (rt-PA), which cleaves the fibrin scaffolding of the thrombus[11], is one of the most common thrombolytics for venous thrombosis[10,12–14]. There are significant side effects associated with thrombolytic therapy,

including hemorrhagic bleeding[15]. To reduce these risks, catheter-directed thrombolysis enables delivery of the lytic directly within the thrombus to allow lower overall dose and duration of infusion[16]. Although this treatment technique is effective for acute thrombi, chronic thrombi are highly resistant to thrombolytic therapy and may require higher lytic doses and longer treatment times[17], thereby increasing the risk for bleeding. Thrombi that do not respond to lytic will continue to occlude the vessel, increasing the risk of future thrombotic events, chronic venous insufficiency, and post-thrombotic syndrome[16]. An adjuvant therapy that reduces the thrombolytic dose while still achieving vessel recanalization would likely improve patient outcomes. Recent years have seen the development of intravascular thrombectomy devices such as the ClotTriever and FlowTriever (Inari Medical, Irvine, CA, USA). These devices use mechanical and aspiratory mechanisms to remove clots. However, they are limited by the size of the vessel[18], are not intended for extensive clot burden[19], and cannot be used in complicated cases, such as for patients with thrombosed IVC filters[20].

1.3 Histotripsy as an adjuvant therapy

Ultrasound imaging is a technique that relies on applying high-frequency acoustic waves to form medical images. In addition to imaging, ultrasound has the potential to produce bioeffects within tissue. High intensity focused ultrasound (HIFU) is currently being investigated for ablation in a variety of pathologies including kidney and liver tumors[21,22] and deep vein thrombosis[23–26]. Because of the transducer geometry, most of the acoustic energy is contained within a small focal zone (e.g. 1.5 mm x 1.5 mm x 2.5 mm[27]). Bioeffects are most prominent within the focal zone, and tissue outside of this zone are spared (Figure 1.3).

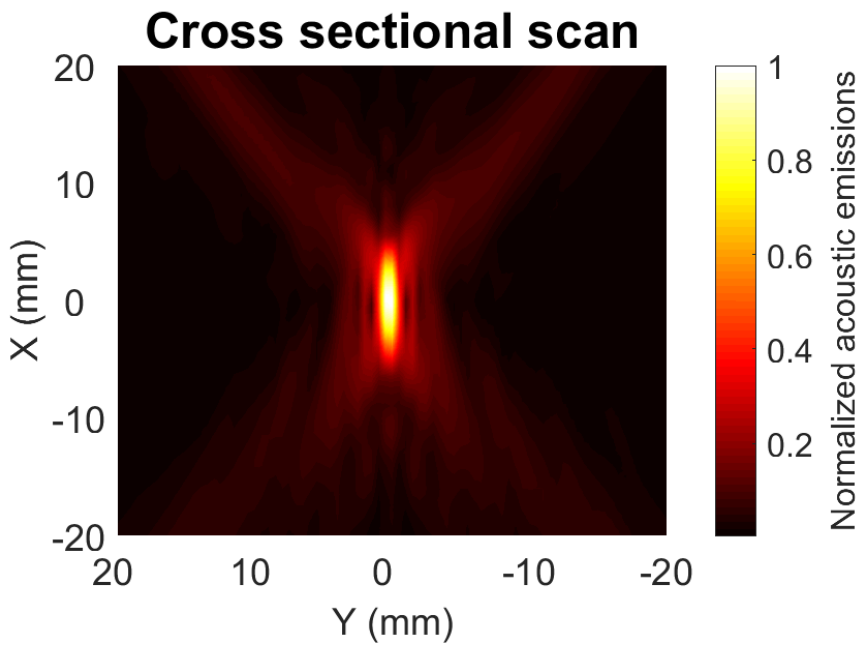

Figure 1.3: Two-dimensional scan of the output waveform from a histotripsy transducer along the axial (x) and lateral (y) dimensions. The hot colormap corresponds to the normalized detected acoustic emissions. There is very little acoustic activity detected outside the focal zone.

As acoustic waves travel through a medium, part of the acoustic energy is deposited locally as thermal energy. Depending on the intensity of the ultrasound beam, its duty cycle, and the total treatment time, thermal effects ranging from mild hyperthermia[28] to thermal necrosis[29] can be induced. Heating is less effective in well-vascularized tissue because of the cooling effect of blood perfusion on thermal diffusion. Moreover, HIFU in some cases may also result in vessel wall disruption and vascular occlusion[30]. Therefore, thermal effects are not desired for treatment for vascular occlusions.

Mechanical action is another bioeffect that can be induced by ultrasound. The application of focused ultrasound to generate cavitation for tissue ablation is known as histotripsy[31] (Figure 1.4). If the peak negative pressure of the ultrasound waveform is sufficiently large, the fluid can undergo a first order phase transformation and cause generation of bubbles[32]. The air-filled bubbles are much more compressible than the surrounding tissue and can undergo large volumetric oscillations

in a processed termed cavitation. This mechanical action is associated with an inertial bubble collapse that can generate free radicals[33], mechanically destroy tissue[34], and induce microstreaming in the surrounding fluid[35,36]. As opposed to thermal HIFU, histotripsy does not rely on heating tissue and is effective when used in vascular tissue. Histotripsy has been used to restore flow in porcine deep vein thrombosis models[26,37]. Further, *in vitro* studies have demonstrated combining histotripsy with lytic yields a more effective treatment than either therapy alone[23]. A deeper understanding of histotripsy and its synergy with thrombolytics will illuminate the path to even more effective deep vein thrombosis treatments.

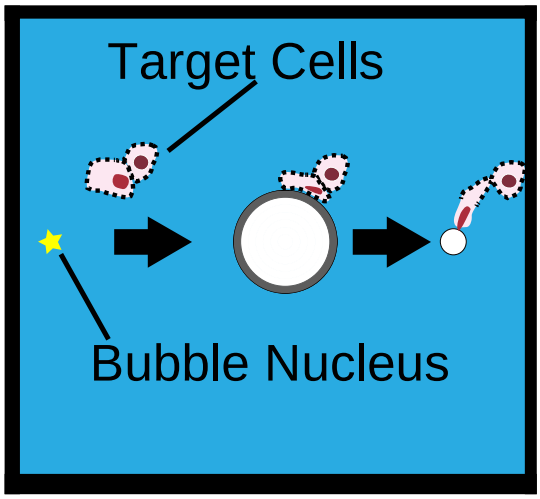

Figure 1.4: Cavitation nucleus being activated by histotripsy insonation. The bubble cloud rapidly expands and exerts a tensile force to permanently deform the surrounding tissue[38].

1.4 Improving image guidance of histotripsy

Image guidance and imaging metrics are essential for an ablative therapy. For histotripsy, the primary metric of efficacy quantifies the mechanical bubble activity. Standard ultrasound imaging sequences can be used to visualize the position of hyperechoic bubble clouds in real time [39–41], but do not provide information about the strength of bubble cloud activity. Passive cavitation imaging, or PCI, spatially maps the power of acoustic emissions generated by the bubble cloud. These

emissions serve as a surrogate for the mechanical activity of the bubble cloud. Recent studies have shown that PCI provides a better predictor for histotripsy ablation than analysis of B-mode ultrasound imaging[42] or magnetic resonance imaging[43]. Thus, passive cavitation imaging can help guide histotripsy and treatment outcome.

1.5 Understanding the mechanisms of histotripsy-aided thrombolysis

Multiple studies have demonstrated that ultrasound is an efficacious adjuvant therapy for thrombolysis[23,24,44]. However, the mechanisms by which histotripsy enhances thrombus degradation in the presence of a lytic remain unclear. It is hypothesized that histotripsy breaks up the thrombus via mechanical hemolysis and promotes enhanced fibrinolysis. Mechanical hemolysis is the result of the bubble cloud exerting sufficient pressure to fractionate erythrocytes[45], effectively ablating the cellular components of the thrombus. Cavitation can cause vigorous fluid mixing[35], which will enable delivery of lytic throughout the thrombus[44,46,47] and will cleave the fibrin mesh into D-dimer[48]. Therefore, hemoglobin is a measure of mechanical hemolysis and D-dimer quantifies fibrinolysis. By understanding the relative contribution of these two mechanisms to clot degradation, treatment parameters can be adjusted to maximize the intended bioeffect.

1.6 Histotripsy and catheter-directed thrombolytics

Catheter-directed thrombolysis (CDT) is the delivery of thrombolytic through an infusion catheter placed within the occluded blood vessel, enabling a higher local drug concentration while lowering the overall systemic dose[16]. The total infusion time of CDT averages between 12-24 hours[49]. However, long exposures to lytic are associated with bleeding complications[15], and extended treatment times exacerbate administrative and financial costs. The goal of using histotripsy as an adjuvant therapy is to increase the efficacy of catheter-directed thrombolytic for lytic-resistant

thrombi. The indwelling catheter may affect the interaction between the bubble cloud and lytic in non-trivial ways compared to a systemic administration route, including altering the clot structure[25], harboring prompt nuclei that serve as a catalyst for cavitation, or breaking down under the action of the histotripsy pulse. These effects should be studied to determine effective histotripsy strategies to enhance catheter-directed thrombolytic.

1.7 Innovation

This work proposes using histotripsy and thrombolytics to disintegrate chronic, intractable thrombi. Current CDT methods are effective for acute thrombi, but have limitations for chronic disease[50]. Aggressive interventions such as mechanical thrombectomies are not justified for chronically ill, bedridden, or aged patients, or those with significant intercurrent disease[51]. Histotripsy offers a non-invasive adjuvant therapy that is applicable for a wider range of patients.

Ablative therapies need useful image guidance and imaging metrics. The BADER Laboratory at the University of Chicago continues to lead the effort on the use of PCI and other imaging metrics to gauge treatment outcomes. Passive cavitation imaging provides both the location and associated energy of acoustic emissions, allowing for image-guided histotripsy treatments. Monitoring histotripsy with PCI will prevent overtreatment and undertreatment, and will thereby improve outcomes for patients.

While histotripsy can destroy clot tissue on its own, it is much more effective when combined with thrombolytics[23]. Our laboratory is at the forefront of histotripsy-augmented thrombolysis research. Combining histotripsy with thrombolytics could enhance thrombolysis for

many patients, and may result in quicker treatment times, shorter hospitalization stays, and lower healthcare costs. For the first time, we have used biomarkers to quantify how histotripsy energy facilitates clot degradation. The work presented in this thesis demonstrates new and clinically relevant results regarding the role of histotripsy-enhancement of lytic in treating chronic thrombo-occlusive disease.

1.8 Dissertation Outline

This dissertation explores the use of histotripsy as an adjuvant therapy for deep vein thrombosis. Chapter 2 investigates the structure of ex vivo human venous thrombi. Chapter 3 examines how passive cavitation imaging can detect histotripsy bubble activity across a wide range of stiffnesses. Chapter 4 studies the relevant mechanisms of histotripsy-enhanced thrombolysis and their relative contribution to overall treatment efficacy. Chapter 5 investigates the treatment efficacy of histotripsy combined with catheter-directed thrombolytics at varying lytic doses. In summary, this pre-clinical work indicates that histotripsy is a promising adjuvant therapy for deep vein thrombosis.

CHAPTER 2

EX VIVO ANALYSIS OF VENOUS THROMBOEMBOLISM

2.1 Introduction

Venous thromboembolism (VTE) is a major health problem, affecting 600,000 Americans annually[52,53]. Pulmonary embolism (PE) and deep vein thrombosis (DVT) are two clinical manifestations of VTE. Pulmonary embolism occurs when a clot obstructs the pulmonary arteries in the lung, with 80% of cases caused by embolization of iliofemoral thrombosis[4]. Obstruction of the pulmonary artery is a clinically significant condition, which carries a 25% mortality rate and a 30-day survival rate of 59%[54]. Deep vein thrombosis is a condition where a blood clot blocks the vasculature of the extremities, typically the legs[1]. Besides the veinous occlusion, there is a prevalent morbidity associated with deep vein thrombosis. Post thrombotic syndrome is characterized by chronic painful leg swelling and venous ulcerations. Phlegmasia cerulea dolens is a circulatory compromise that can be limb-threatening[55,56]. Rapid restoration of flow is required to prevent amputation of the afflicted limb (15%)[57] or patient death (25%)[58]. There is also a significant financial burden for VTE, with healthcare costs exceeding 7 billion dollars annually [59–61]. Together, these data indicate the need for effective treatments for VTE.

The standard of care to recanalize occluded iliofemoral veins is catheter-directed thrombolytics (CDT) administered over the course of several days[16]. Recombinant tissue plasminogen activator (rt-PA) is a fibrin-specific thrombolytic which is efficacious for acute thrombus[62–66]. In the United States, rt-PA is the most common thrombolytic for DVT thrombolysis[67]. Chronic thrombus components are present in 27% to 43% of VTE cases[15,50], and do not respond to lytics[17]. Complete removal of thrombus results in better long-term outcomes than partial removal[68], but administration of thrombolytic drugs increases the risk of bleeding

complications for nonresponsive thrombi [13]. Alternative treatment profiles such as mechanical extraction[18,20] or histotripsy-aided thrombolysis[23] may expedite thrombus resolution for chronic pathologies. Foreknowledge of thrombus susceptibility to lytic therapy will reduce risk of unnecessary exposure to thrombolytic agents and will improve clinical outcomes.

Changes to the thrombus composition might explain the lytic resistive nature of chronic VTE. However, the precise mechanism by which chronic thrombi develop resistance to lytic therapy in VTE patients is lacking. Animal models do not fully replicate the clotting cascade of humans[69–71], and traditional treatment methods leave the sample *in situ*[16,72]. The advent of venous thrombectomy devices has enabled the extraction of samples for to characterize formed elements associated with lytic resistance.

Imaging techniques may provide a means to detect chronic thrombus components. This information may then help guide appropriate treatment schemes. Thrombi become stiffer as the age of the thrombus increases, which can be measured with shear-wave elastography[73,74]. Previous studies have shown that erythrocyte-rich thrombi are more susceptible to lytic therapy than thrombi with few erythrocytes[75,76]. The susceptibility of thrombus structure mapped with MRI can be used to assess its erythrocytic composition[77].

In this study, samples collected from VTE patients were characterized ex vivo. Qualitative and quantitative histological analysis was conducted to assess formed elements within the samples. To provide whole sample analysis, imaging data was collected to determine susceptibility (MRI quantitative susceptibility mapping) and stiffness (ultrasound shear-wave elastography) of the thrombus. Formed elements in the sample were correlated with 1) thrombus age based on the onset of symptoms, and 2) response to lytic therapy using an *in vitro* methodology. Primary findings

indicate that collagen content increases and red blood cell content decreases as clots age, and that quantitative susceptibility imaging may correlate with thrombolytic susceptibility.

2.2 Materials and methods

2.2.1 Thrombus collection

As part of the standard of care, thrombi were extracted from patients undergoing mechanical thrombectomy procedures at the University of Chicago Medical Center and the University of Texas Health Science Center. Samples were subjected to analysis following local internal review board approval and informed consent (University of Chicago IRB #18-0179). Extracted samples were stored in saline solution and processed for analysis within 24 hours of collection. A total of 26 thrombi were examined, of which 11 were deep vein thrombi, and 12 were pulmonary emboli. Samples were sectioned for different types of analyses: One section was embedded in low-gelling temperature agarose (Sigma-Aldrich, USA) for imaging analysis, one section was subjected to rt-PA to assess lytic response, and one section was processed for histology. Not all samples were large enough to conduct each set of analyses (26 histology samples, 9 thrombolysis samples, 9 QSM samples, 12 elastography samples).

2.2.2 Assessment of clot structure via histology

Histology was used to assess the structure of samples. Immediately after collection, thrombi were sectioned (~3 mm thickness) and submerged in 10% formalin for 24 hours. After fixation, thrombus sections were submitted to the University of Chicago Human Tissue Resource Center for paraffin-embedding, sectioning (5 μm thickness), and histochemical staining. Three stains were used: Hematoxylin & Eosin (H&E, Tissue-Tek Prisma H&E Stain Kit #1, Sakura Finetek, USA),

Masson's Trichrome (Trichrome Staining Kit, Hoffmann-La Roche, Switzerland), and CD-61 (CD61, Platelet Glycoprotein IIIa, Agilent, USA).

Stained specimen were scanned at 20x magnification using a ScanScope XT scanner (Leica Biosystems, Germany). Digitized slides were viewed using ImageScope software (Leica Biosystems, Germany), and were analyzed using the Positive Pixel Count algorithm (Leica Biosystems, Germany) to identify red blood cells and fibrin in H&E stains, collagen in Masson's Trichrome stains, and platelets in CD-61 stains. The number of pixels that fall within the designated color parameters (i.e. thrombus component) were quantified and binned into intensity ranges: negative, weak positive, positive, or strong positive. Color thresholds were evaluated and accepted by a board-approved pathologist, and a representative example is shown in Figure 2.1.

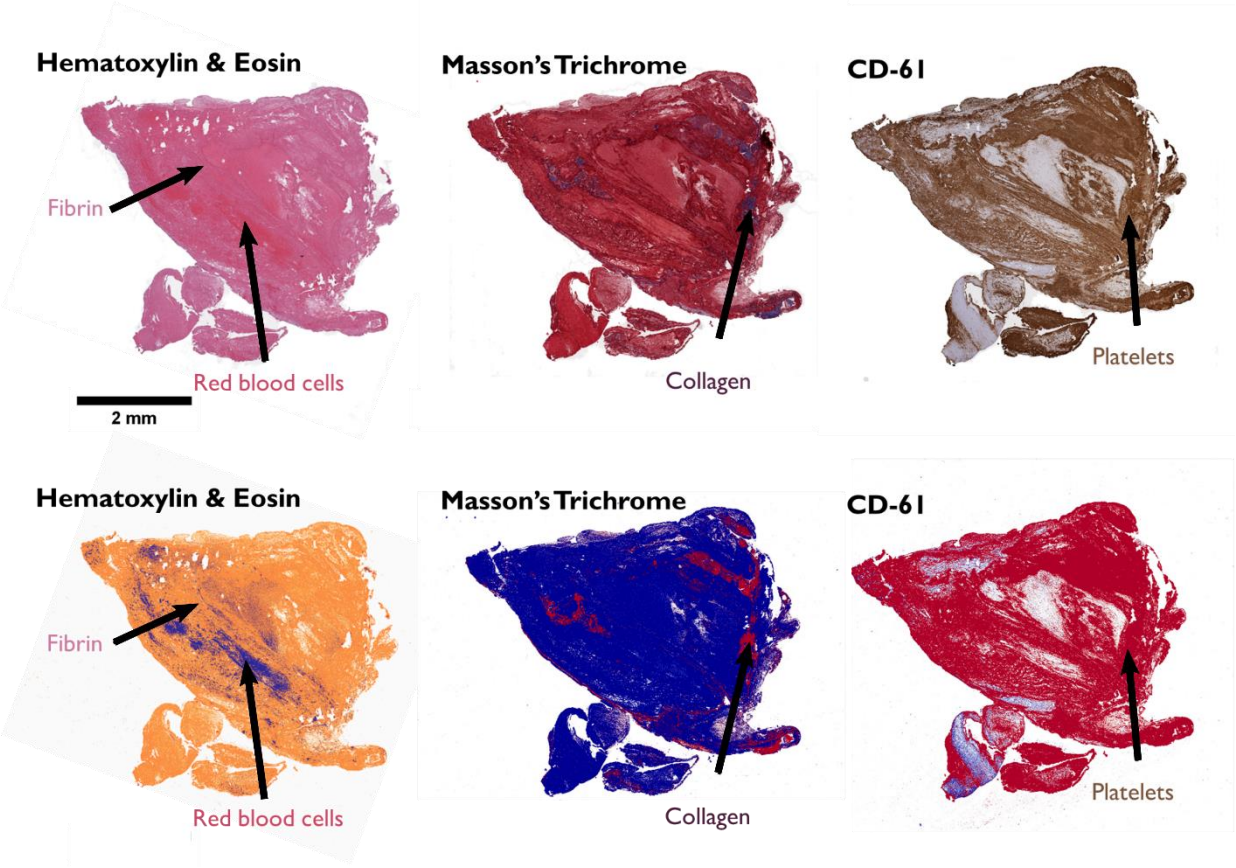

Figure 2.1: Semi-quantitative histological analysis for a representative thrombus sample. The top row indicates sections stained with Hematoxylin & Eosin, Masson's Trichrome, and CD-61. The bottom row indicates the results of the color thresholding algorithm, which counts the number of pixels corresponding to the component of interest.

Four samples were also subjected to immunofluorescent analysis to quantitatively assess formed elements. Fluorescent antibodies were used to examine the co-location of fibrin (MABS2155, Millipore Sigma, USA), collagen, platelets (CD-61, M075301-2, Agilent, USA) vascular endothelial growth factor (VEGF, ab32152, abcam, USA), and plasminogen-activator inhibitor-1 (PAI-1, ab125687, abcam, USA). Red blood cells were examined utilizing their innate autofluorescence and did not require staining. Two samples were stained with PAI-1 and CD31 (ab28364, abcam, USA) to gauge the co-expression of PAI-1 and endothelial cells. Samples were stained using an Opal 7-color manual IHC kit (Akoya Biosciences, USA) and were scanned using

a Vectra Polaris whole slides scanner (Akoya Biosciences, USA). Additional antibody information can be found in Table 2.1.

Table 2.1: Antibody and scanning information. CD61 and CD31 share the same Opal and filter procedures, but CD31 was used exclusively with PAI-1.

Primary antibody	**Antibody dilution**	**Opal**	**Filter**
PAI-1	1:50	540	Cy3
VEGF-1	1:50	570	Cy3
Fibrin	1:100	520	FITC
Pan collagen I-III	1:50	620	Texas Red
CD61	1:40	690	Cy5
CD31	1:200	690	Cy5

2.2.3 Assessment of thrombolytic susceptibility

Human fresh-frozen plasma type O plasma was obtained from a blood bank (Vitalant, Chicago, IL), and was aliquoted and stored at -80°C before use. Lytic was obtained as a lyophilized powder (Activase, Genetech, San Francisco, CA, USA), mixed with sterile water to a concentration of 1 mg/mL, and stored at -80°C before use[25]. Ex vivo thrombi were sectioned into ~1 cm segments and were exposed to either plasma and rt-PA (2.68 μg/mL, consistent with pharmacomechanical VTE treatment) or plasma alone (control). To account for the heat-dependent enzymatic activity of rt-PA[78], thrombus sections were placed in individual latex bags filled with 15 mL of human plasma with or without rt-PA submerged in a water tank heated to physiologic temperature (37°C). Thrombolytic susceptibility was reported as the percent change in mass of the sample before and after exposure to lytic. Physical manipulation of the thrombi and innate thrombolytics within the

plasma may affect the mass of the clot. To account for these factors, the mass loss residual was computed as follows:

$$M_{residual} = M_{lytic} - M_{control} \quad (2.1)$$

where M_{lytic} is the mass loss for clots exposed to lytic and plasma, and $M_{control}$ is the mass loss for clots exposed to plasma alone.

2.2.4 Assessment of hemoglobin content via QSM

Quantitative susceptibility mapping (QSM) is an MRI sequence that maps how easily a sample can become magnetized. Paramagnetic tissues appear hyperintense in QSM images, and diamagnetic tissues appear hypointense[77]. A clinical 3 Tesla (3T) MR system (Ingenia dStream, Philips Healthcare, Best, The Netherlands) with a body transmit coil and a 16-channel head-and-neck receive coil was used to collect QSM images of the agarose embedded samples[79]. A three-dimensional gradient echo recall sequence was employed to acquire multiple echoes. Utilizing the real and imaginary portions of the received signals, magnetic susceptibility was computed via the morphology enabled dipole inversion (MEDI) pipeline[80]. Thrombi were contoured by hand to exclude background QSM values. Positive QSM values (i.e. ppb > 0) were tabulated to gauge the concentration of erythrocytes in VTE samples. This technique exploits the paramagnetic nature of hemoglobin while excluding highly diamagnetic tissues.

2.2.5 Assessment of clot stiffness via ultrasound elastography

Ultrasound elastography was used to assess the stiffness of the agarose-embedded ex vivo samples[81]. Ultrasound images were acquired with a linear array transducer (GE Ultrasound Transducer 9L, 9 MHz nominal frequency) and Logiq E9 scanner (GE Healthcare, Chicago, IL,

USA). The scanner exam protocol "Small Parts" was utilized. Based on the approximate depth of the sample, a 2 cm scan depth and 9 MHz frequency setting provided good resolution of the sample. Standard B-mode images were used to visualize the cross section of the sample (e.g. orthogonal to its *in situ* vascular orientation), and a shear wave elastography sequence was used to map the elastic modulus. Three images (e.g. three measurements of elastic modulus) were recorded for each sample. For each section, regions-of-interest ~ 4 mm in diameter were selected to quantify the elastic modulus (Young's modulus) depending on the diameter of the thrombus (mean diameter 0.7 mm, range 0.3 – 1.4 mm). To avoid surface waves along the thrombus/agarose interface, regions-of-interest were not acquired near the edge of the sample[82].

2.2.6 Statistical analysis

Statistical analysis was performed using the MATLAB Statistical Toolbox (The Mathworks, Natick, MA, USA). Correlations were quantified using the Pearson's correlation coefficient. Wilcoxon ranked-sum tests were used to compare the composition of thrombi across two age groups.

2.3 Results

2.3.1 Histological analysis

Histological analysis of formed elements within the thrombi are shown in Figure 2.2. A wide range in composition was noted, with fibrin exhibiting the highest variability between samples. Fibrin and red blood cells comprised the primary thrombus components (52 ± 26% and 35 ± 23%, respectively). Collagen constituted less than < 2% of the thrombus area on average, though select samples containing more than ~ 2% collagen as depicted in Figure 2.3. The range of fibrin and RBC values observed for DVT samples were smaller in comparison to ranges observed for PE

samples. Median values for collagen, fibrin, RBC, and platelets were not significantly different between PE and DVT samples.

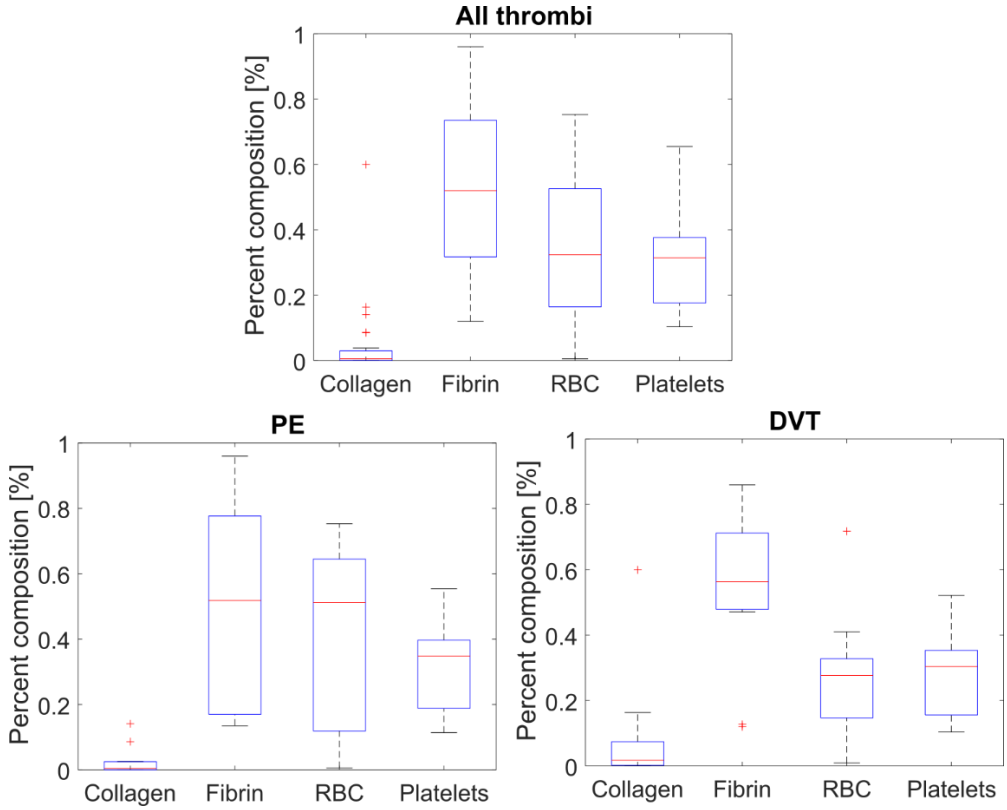

Figure 2.2: Clot composition as a function of area for collagen, fibrin, platelets, and RBC for all thrombi samples (top), exclusively pulmonary embolisms (bottom-left), and exclusively DVT samples (bottom-right). Red crosses indicate outliers and horizontal red lines indicate median values.

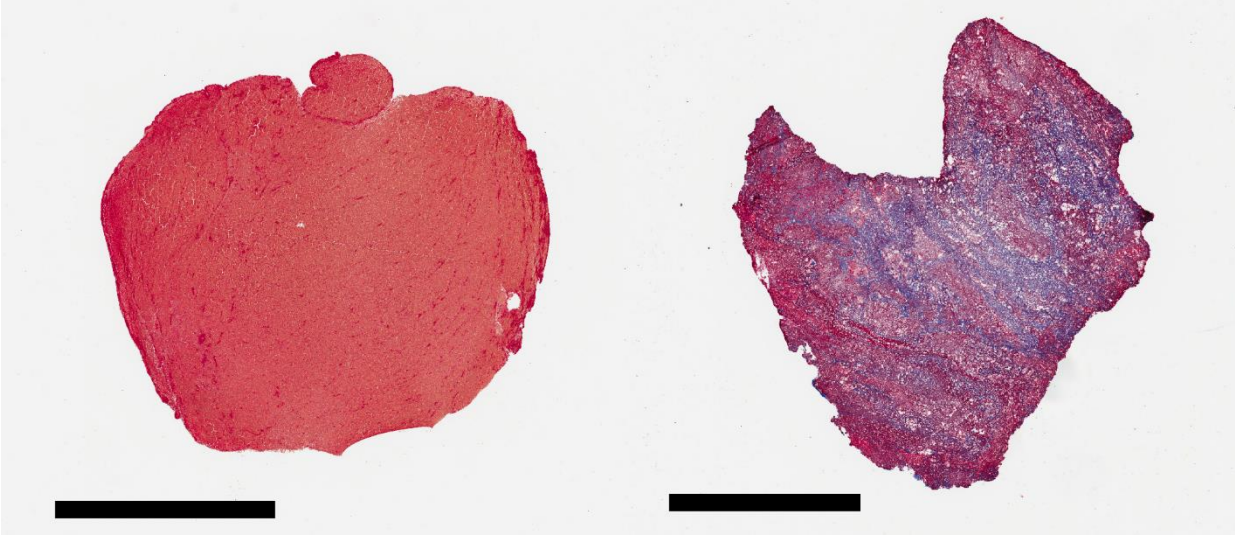

Figure 2.3: Representative thrombus samples stained for collagen, which appears blue, using Mason's Trichrome. Scale bars indicate 2 mm. The thrombus on the right contains 100x more collagen than the thrombus on the left (60% vs. 0.06% collagen by area).

The interdependence of formed elements was also calculated. Trends between collagen, fibrin, red blood cells, and platelets are shown in Figure 2.4. The strongest correlation was between fibrin and red blood cells ($R^2 = 0.827$; $p << 0.001$). A medium-strength correlation was observed between fibrin and platelets ($R^2 = 0.434$; $p = 0.0003$). Significant correlations were also noted between red blood cells and platelets ($R^2 = 0.255$; $p = 0.01$), red blood cells and collagen ($R^2 = 0.223$; $p = 0.02$), and fibrin and collagen ($R^2 = 0.197$; $p = 0.02$). There was no correlation observed between collagen and platelets ($R^2 = 0.0410$; $p = 0.3$).

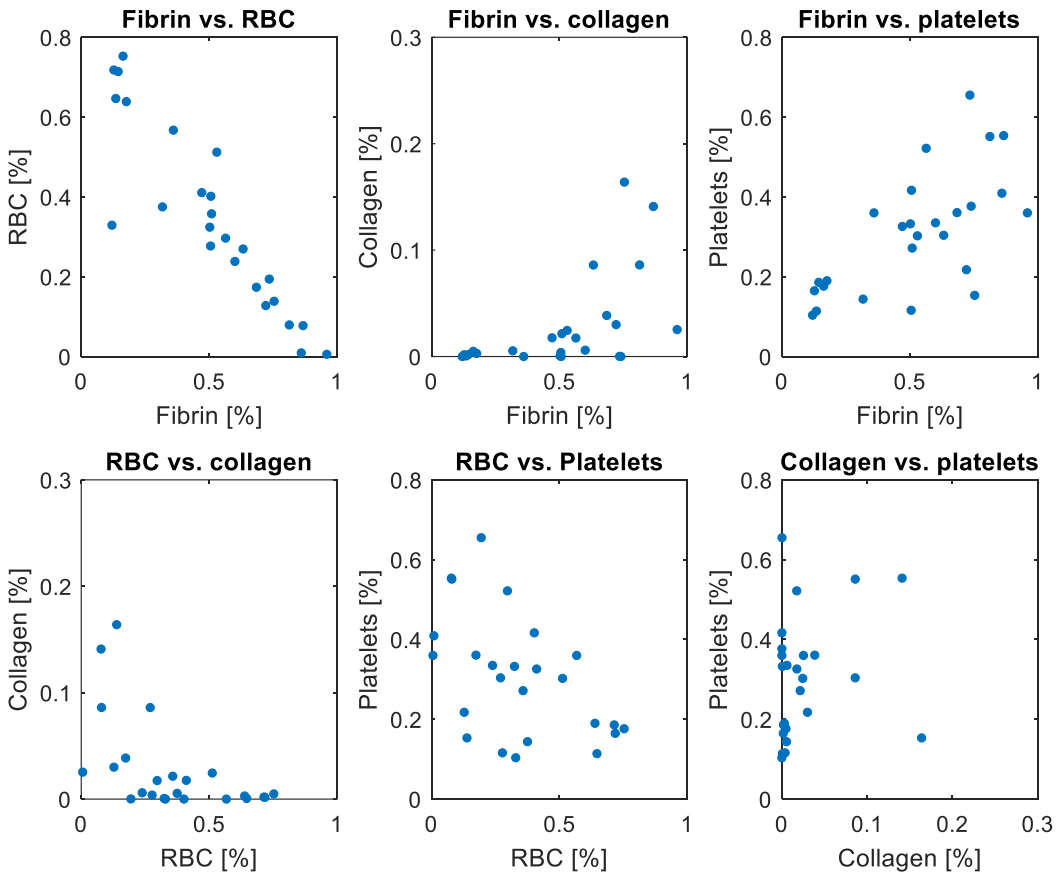

Figure 2.4: Trends in thrombus composition for fibrin, collagen, red blood cells, and platelets. Each datapoint corresponds to one thrombus sample.

2.3.2 Immunofluorescence data

Figure 2.5 depicts a representative sample after immunofluorescence staining and imaging. Unlike standard IHC, immunofluorescence uses multiple antibodies on a single slide to enable direct comparison between the locations of formed elements. Collagen, fibrin, and platelets were usually observed in close proximity to one another. Similar to the observations in Figure 2.4, red blood cells were observed in areas of low fibrin concentration. One marker of neovascularization, VEGF, was not prevalent in these samples. An additional marker of neovascularization and endothelial

cells, CD-31, was used (Figure 2.6). Endothelial infiltration was observed, particularly around the edges of the samples. Furthermore, endothelial cells were typically co-located with PAI-1.

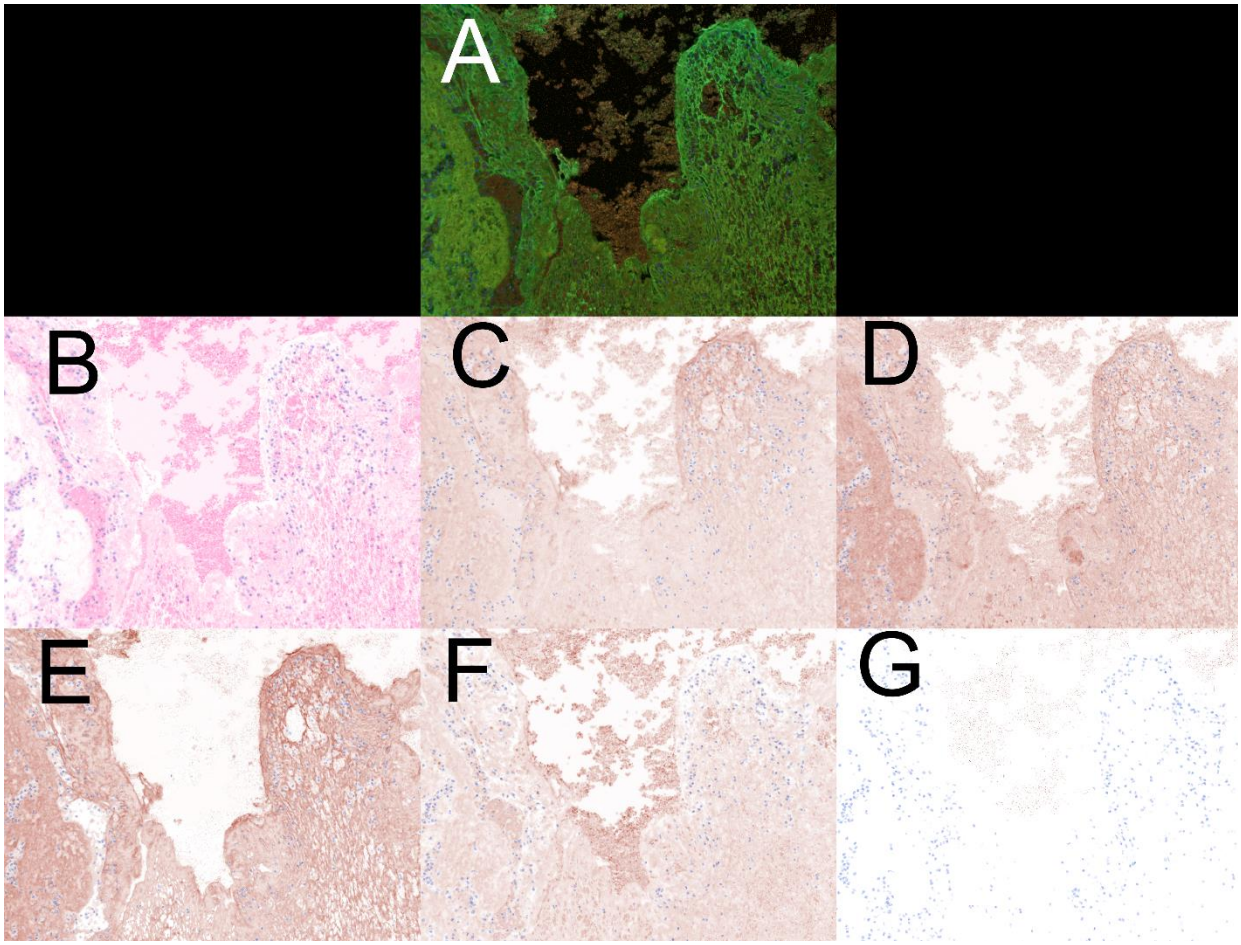

Figure 2.5: (A) Combined overlay and thrombus components analyzed using immunofluorescence, (B) red blood cells, (C) platelets, (D) collagen, (E) fibrin, and (G) VEGF. Images B-G are spectral deconvolutions of the single image A.

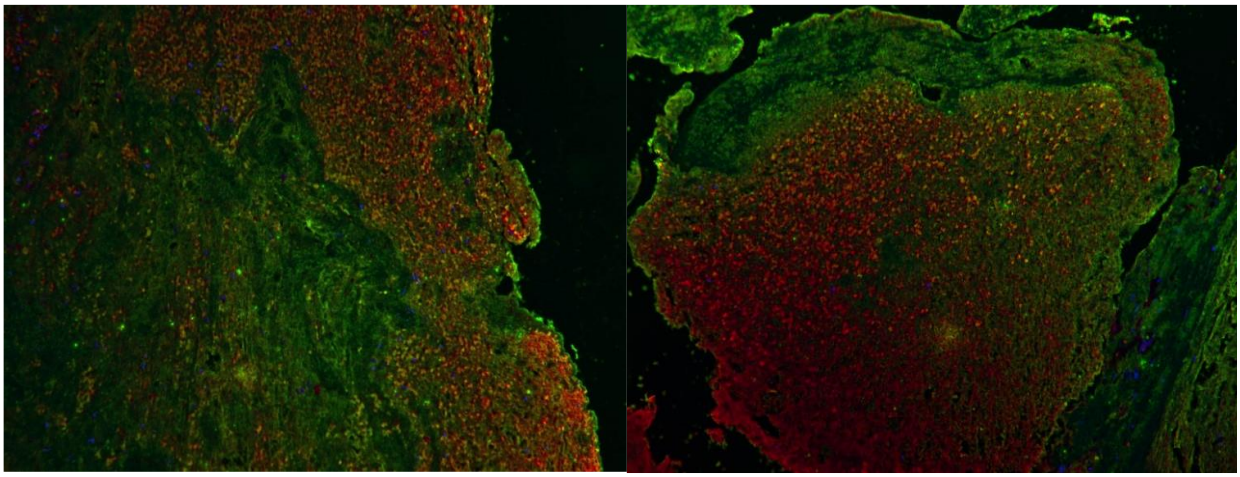

Figure 2.6: Two immunofluorescence images indicating endothelial cells (red, CD31) and PAI-1 (green). The overlap appears dark yellow in color.

2.3.3 Thrombus chronicity

Prior studies indicate significant structural remodeling of VTE after seven days[7,51,83]. Figure 2.7 depicts the histological composition of thrombi based on the seven-day threshold. Wilcoxon ranked sum tests indicated that thrombi more one week old were composed of more collagen ($p = 0.03$) and fewer red blood cells ($p = 0.02$) than for acute thrombi (<7 days). No changes were observed for fibrin ($p = 0.190$) or platelets ($p = 1.00$) with thrombus age.

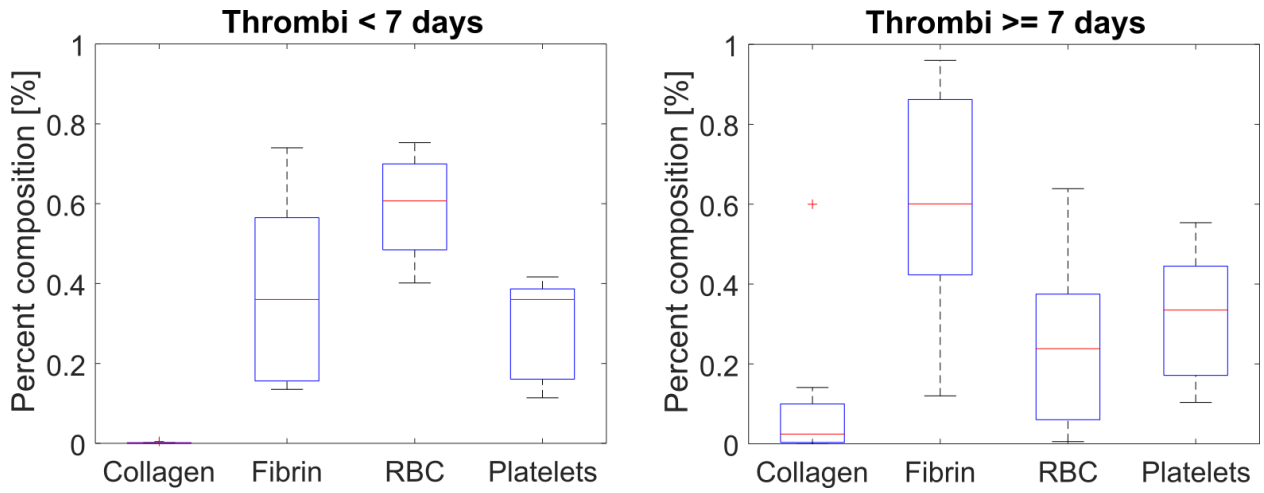

Figure 2.7: Thrombus composition for acute (<7 days old) and chronic (≥7 days old) thrombi.

2.3.4 Thrombolysis

Each thrombus sample exhibited a different sensitivity to rt-PA, with mass losses ranging from under 10% to almost 50%. Samples exposed to plasma alone exhibited a decrease in mass ranging between 0% and under 30%. A two-sample t-test revealed that the lytic group had greater mass loss than the control group ($p < 0.05$). No significant correlation between thrombus components (e.g. fibrin, collagen, platelets, red blood cells) and thrombolysis was observed.

2.3.5 Shear wave elastography

The stiffness of agarose-embedded samples was measured using shear-wave elastography imaging. A wide range of stiffnesses was observed across all clots, varying on average from 53 kPa to 122 kPa. Significant intrathrombus stiffness variation was also observed (Figure 2.8). No trends were observed between stiffness and thrombus composition. Furthermore, no trend was observed between stiffness and thrombolysis.

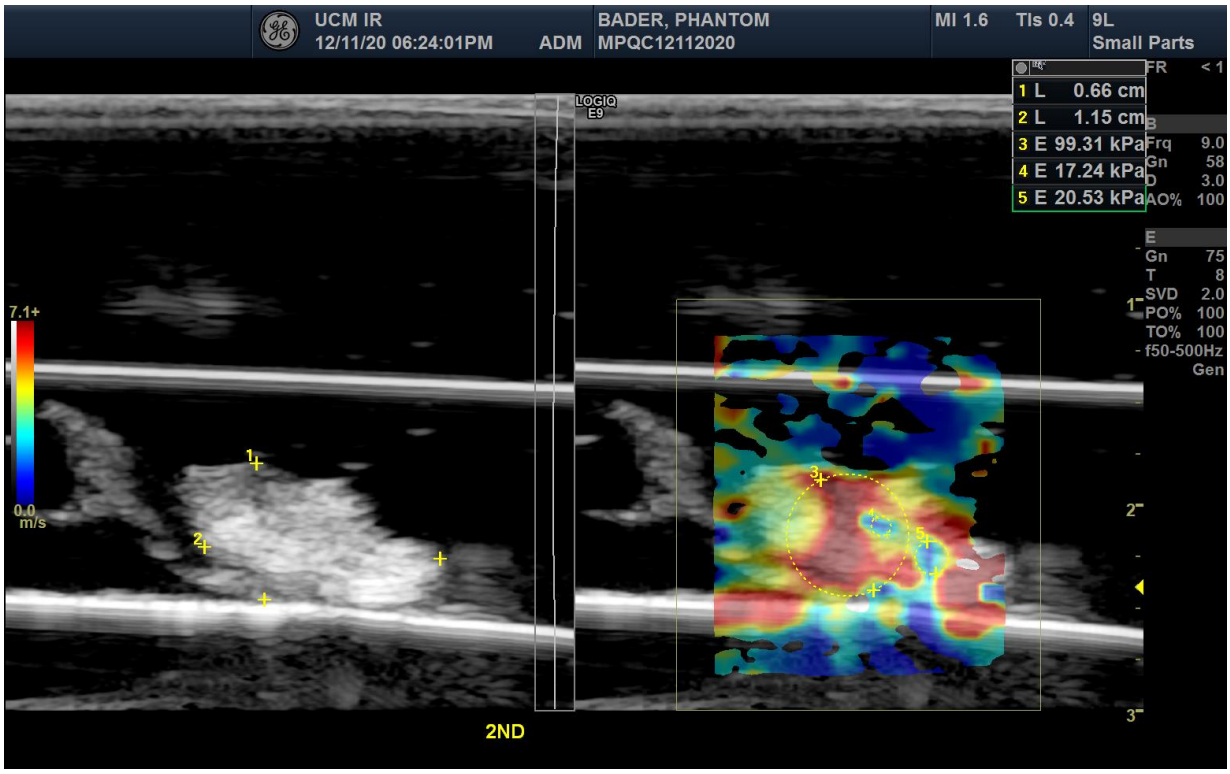

Figure 2.8: Representative B-mode image of thrombus sample (left) and image with elasticity map overlay (right). Red indicates high stiffness, and blue indicates low stiffness. Yellow circles circumscribe ROIs for stiffness calculation.

2.3.6 Quantitative susceptibility mapping

Quantitative susceptibility map (QSM) data were used to compare magnetic susceptibility to thrombolysis and the proportion of thrombus components. Samples were observed to have heterogenous magnetic susceptibilities, as shown in Figure 2.10. Qualitative observation revealed concentrated zones of high and low QSM values throughout the samples. Positive-pixel QSM values were compared to thrombolysis data. Although statistically insignificant, a relationship was observed between thrombolysis and magnetic susceptibility (Figure 2.9, R = 0.66, p = 0.05).

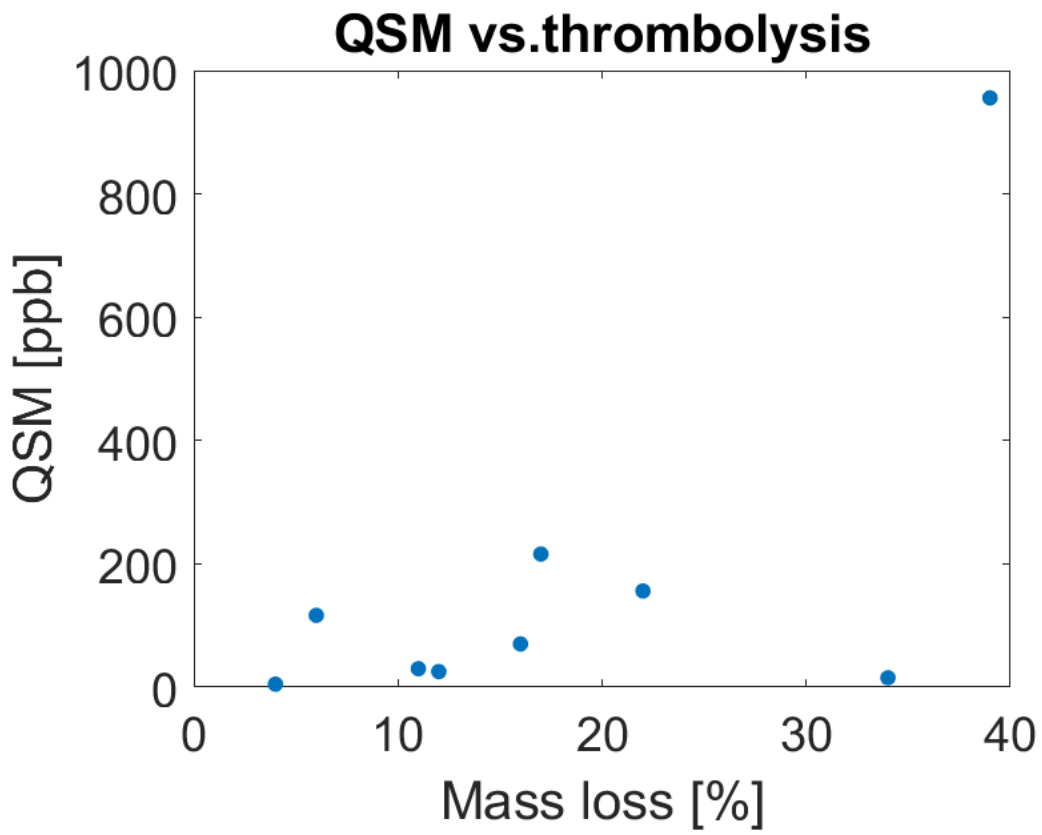

Figure 2.9: Comparison of clot mass loss vs. quantitative susceptibility map data (R = 0.66, p = 0.05).

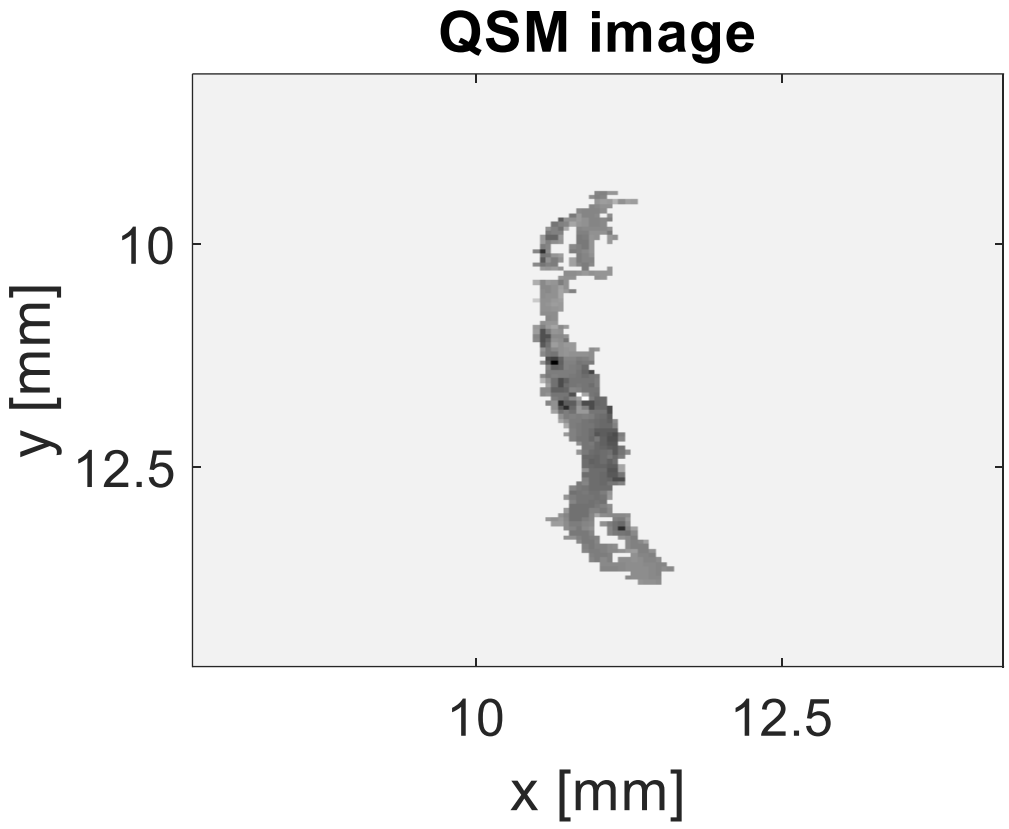

Figure 2.10: Magnetic susceptibility of a representative sample measured via quantitative susceptibility mapping. The gray colormap represents normalized QSM data values. Bright areas indicate high QSM values, and dark areas indicate low QSM values.

2.4 Discussion

2.4.1 Histological observations

A better understanding the structure of thrombi will help pave the way for more effective treatment strategies. Prior studies have indicated that chronic VTE is unresponsive to lytic therapy, though the precise mechanism of lytic resistance remains elusive. One hypothesis is remodeling of the thrombus structure. Because rt-PA is specific to fibrin[84,85], its thrombolytic efficacy will be reduced if collagen constitutes a significant proportion of the extracellular matrix[7]. The results in this study indicate that the extracellular structure was mainly composed of fibrin, not collagen.

This may be due to the method of specimen extraction, as elements attached to the vascular wall (such as collagen) may not have been retrieved.

Thrombus structure may affect the risk of embolization. Cases involving DVT had less variability in fibrin and RBC as compared to PE. This result indicates that thrombi with consistently high amounts of fibrin, such as DVT (Figure 2.2), may be more likely to remain stationary. In extreme cases, the extracellular matrix of the thrombus can even become incorporated into the venous wall[7]. Measuring the dissolution of fibrin could be a way to predict risk of embolization[86].

Chronicity was observed to influence general thrombus composition. A significant decrease in red blood cell composition and a significant increase in collagen content was observed as the thrombus age increased beyond 7 days. *In vitro* experiments have indicated that fibroblasts infiltrate and secrete fibrillar collagen over the course of days[87,88]. Our ex vivo data supports this observation and suggests that older thrombi will contain more collagen.

A final observation in these studies was the correlation between PAI-1 and endothelization of the thrombus. PAI-1 is an important serine protease inhibitor in the thrombolytic pathway and is produced by endothelial cells, megakaryocytes, and fibroblasts, among others[89,90]. Our results indicate that endothelial cells may play a role in the generation of PAI-1. Endothelization was noted primarily along the edges of the thrombus, possibly because as a thrombus ages it will become integrated within the venous wall[7]. Future studies should continue to investigate PAI-1 to understand the connection between thrombus morphology, PAI-1 levels, and overall thrombolysis. Very little amounts of VEGF were detected, most likely due its low concentration (0-115 pg/mL) in the plasma of healthy humans[91].

2.4.2 Thrombolysis and thrombus morphology

No significant trends were observed between thrombolysis and thrombus components (red blood cells, platelets, fibrin, or collagen). This result may be influenced by multiple factors. First, the biological variability between samples might obscure any weak trends. Secondly, histology produces 2-dimensional images whereas thrombolysis is a 3-dimensional measure. Thrombi samples are highly heterogeneous (Figure 2.2), so single sections of thrombi may not be representative of the thrombus as a whole. Third, the histological analysis used in this study detects neither the strength of fibrin cross-linking nor the mean fibrin diameter. Both of these factors have been shown to affect thrombolysis[92,93].

Thrombolysis may be affected by components beyond collagen, red blood cells, fibrin, and platelets. We have found that PAI-1 concentration tends to increase in proximity to collagen, fibrin, and platelets, and that PAI-1 is co-expressed with endothelial markers. The close proximity of PAI-1 to the extracellular matrix may explain why chronic thrombi are more resistant to thrombolysis than acute thrombi.

2.4.3 Variations in thrombus stiffness

Prior studies have indicated that increased stiffness is a hallmark of chronic thrombi[94–96], and correlates with lytic susceptibility[82]. No trends were observed here between the elastic modulus of the samples and thrombus composition or thrombolysis metrics. The lack of trends may be attributed to the large variations in thrombus stiffness. Even within a single thrombus, the stiffness can vary by more than 80 kPa. The average stiffness is not a good metric because of the inhomogeneities seen in samples. Rather than classifying an entire thrombus as acute or chronic, it would be more accurate to describe the samples as thrombi with acute and chronic portions.

Alternatively, the maximum stiffness could be used as an accurate thrombus metric. If stiffness limits the efficacy of lytic[82], then the maximum stiffness could help the physician prescribe an effective treatment course.

2.4.4 Predicting thrombolysis in situ

Thrombus composition and thrombolysis is highly variable. A primary goal of this study was to determine if imaging metrics (i.e. QSM and shear wave elastography) can be used to predict thrombolytic susceptibility. Our data shows that stiffness, measured with shear wave elastography, does not correlate with thrombolysis. However, a possible trend was noted between magnetic susceptibility and thrombolysis. Deoxygenated hemoglobin has high magnetic susceptibility[97] and can be tracked using QSM[77]. Because erythrocytes contain hemoglobin, our data indicates that increases in red blood cell composition might be associated with increases in thrombolysis. This agrees with our observation that older thrombi typically contain fewer red blood cells than acute thrombi, especially considering that older thrombi are less susceptible to thrombolytics[7]. Thus, QSM may be a good predictor for thrombolysis *in situ*. It should be noted that although there is a qualitative trend, this trend is not statistically significant. Nevertheless, the data is promising and warrants further examination with regards to thrombolysis and QSM values.

2.4.5 Limitations

The samples examined in this study may not reflect the true structure of the thrombi *in vivo*. Mechanically extracting the thrombi may have added bias by either by including extraneous non-thrombi elements or by leaving behind essential thrombi elements. Sample handling, such as using tweezers to move samples, may have also affected the shape and integrity of the samples. However, this most likely would only have a small effect, as most of the thrombi samples appeared intact

upon gross observation. Thrombolysis measurements may not reflect thrombolysis *in vivo* because samples were exposed to plasma, not whole blood. The blood chemistry for chronic samples may be different and could affect the thrombolysis cascade. Due to the retrospective nature of this study, the ages of the thrombi are estimates based on the onset of symptoms and are not exactly known. Most thrombi were below two weeks in age. The data may not be representative in extremely old thrombi (>30 days old). Due to the limited size of some of the thrombus samples, not all thrombi could be analyzed with our full testing panel (i.e. thrombolysis, QSM, and elastography).

2.5 Conclusions

In conclusion, we have shown that thrombi are significantly inhomogeneous. Age of the thrombus affects composition and leads to increases in collagen content and a decrease in red blood cells. Although shear wave elastography is not able to predict thrombolysis, QSM showed a promising trend with thrombolysis that warrants further investigation.

CHAPTER 3

IN VITRO ASSESSMENT OF STIFFNESS-DEPENDENT HISTOTRIPSY BUBBLE CLOUD ACTIVITY IN GEL PHANTOMS AND BLOOD CLOTS

The work in this chapter is a preliminary submission and was conditionally accepted for publication. The fully accepted article has been published as: S.A. Hendley, V. Bollen, G.J. Anthony, J.D Paul, K.B. Bader, *In vitro* assessment of stiffness-dependent histotripsy bubble cloud activity in gel phantoms and blood clots, Phys Med Biol **64**(14), 145019 (2019).

3.1 Introduction

It is important to understand the influence of medium stiffness on the bubble cloud activity necessary for uniform tissue liquefaction. Tissue is liquefied not as a direct result of the incident pulse, but due to the nucleation and resultant mechanical action of bubble clouds[99]. The type of mechanical activity that can be initiated is dependent on the type of histotripsy pulse[100]. For shock-scattering histotripsy, a bubble cloud is formed when the nonlinear, multi-cycle pulse scatters from a microbubble activated within the focal zone[101]. Expansion of bubbles within the focal zone imparts lethal strain on the surrounding cellular and extracellular tissue[102,103]. Pre-clinical studies have demonstrated the efficacy of histotripsy ablation for healthy tissues[98]. Chronically pathologic tissue, including deep vein thrombosis[104], is stiff compared to healthy tissue[105,106]. The medium stiffness can have a significant influence on histotripsy-induced bubble dynamics[103,107], and therefore ablation efficacy.

Passive cavitation imaging maps the power of acoustic emissions generated by the mechanical oscillations of bubbles[108,109]. Previous studies have employed passive ultrasound imaging techniques to monitor thermal ablation with focused ultrasound[110–112], ultrasound-mediated drug

delivery[113–116], histotripsy bubble clouds[117], and clot liquefaction with histotripsy[118]. In a recent study, passive cavitation imaging provided a better predictor for histotripsy liquefaction than plane wave B-mode hyperechogenicity in a tissue-mimicking phantom with a fixed stiffness [119].

The objective of this study was to determine the medium stiffness dependence of the bubble cloud activity necessary for liquefaction *in vitro*. Acoustic emissions generated by histotripsy-induced bubble clouds in agarose phantoms of varied Young's moduli were processed to form passive cavitation images. Additionally, the bubble cloud grayscale was also tracked with plane wave B-mode images. The threshold acoustic emissions or grayscale for phantoms were assessed via receiver operating characteristic (ROC) curve analysis. Bubble activity was also assessed in clots formed *in vitro* with varying degrees of retraction, and therefore varying clot stiffnesses [120]. The degree of clot liquefaction was assessed histologically, and the power of bubble cloud emissions generated by the histotripsy pulse was recorded. Finally, an analytic model was utilized to assess the influence of medium stiffness on histotripsy-induced bubble expansion for the conditions considered in this study.

3.2 Materials & Methods

3.2.1 Porcine red blood cell phantom preparation

Red blood cell phantoms composed of alternating layers of agarose and porcine red blood cell/agarose mixtures were manufactured following Maxwell et al.[121]. Briefly, 50 mL of unspecified CPD porcine blood was obtained from a commercial vendor (Lampire, Pipersville, PA) and centrifuged at 3,000 RPM for 10 minutes. The plasma and buffy coat supernatant were removed, leaving behind a volume of red blood cells. Agarose powder (1.48, 2.00, 3.60, 4.00, or 5.80 g) and 3.6 g NaCl (Sigma-Aldrich, St. Louis, MO, USA) were dissolved into 400 mL of 0.2-

μm filtered, deionized water by heating in a microwave (700 W power) in 30 second increments until clear. The resulting concentrations of agarose reported in w/v (g/mL) were 0.37%, 0.50%, 0.90%, 1.00%, and 1.45%. The agarose mixture was then transferred to an ultrasonic cleaning bath heated to 55 °C while continuously evacuating (50 kPa) over the course of 30 minutes. After degassing, approximately 47 mL of the agarose mixture was poured into a rectangular acrylic phantom mold and allowed to solidify. A 5% v/v red blood cell/agarose mixture was pipetted onto the solidified agarose slab to form a layer approximately 500 μm thick. This process was repeated to generate three red blood cell layers separated by 1.5 cm, after which the phantom was placed in a 4 °C refrigerator overnight.

3.2.2 Human blood clot phantom production

Human whole blood clots were manufactured following an established protocol[120,122]. After local institutional review board approval and informed written consent, venous human whole blood was drawn from five patients undergoing invasive catheterization procedures at the University of Chicago Medicine cardiac catheterization laboratory (patient demographics in Table 3.1). Patients on medications that would alter the clotting cascade (e.g. platelet inhibitors, etc.) were screened out of the study *a priori*. Blood aliquots of 2 mL were transferred to Pasteur pipettes composed of either borosilicate or flint glass (14.6 cm length, 2 mL capacity, Fisher Scientific, Hanover Park, IL, USA) to produce clots of high or mild retraction, respectively[120,122]. The pipettes were submerged in a water bath at 37 °C for 3 hours, and allowed to retract over the course of three days at 4 °C. After three days, the clots were suspended in a 2% w/v low-gelling temperature agarose (product number A0701, Sigma-Aldrich, St. Louis, MO, USA) phantom prior to histotripsy insonation or retained for assessment of elastic properties.

Table 3.1: Demographics for the five patients from whom blood was drawn.

Clot number	Sex	Age	Race
1	F	61	African American
2	F	72	White
3	M	77	African American
4	M	64	White
5	M	56	White

3.2.3 Young's modulus measurements

The Young's modulus of each phantom layer was determined with a shear-wave elastography imaging sequence using an L11-4v imaging array (Verasonics, Inc., Kirkland, WA, USA) driven by a research ultrasound system (Vantage 128, Verasonics, Inc. Kirkland, WA, USA)[123]. Images were processed offline[124] to assess the shear wave speed. The Young's modulus was related to the shear wave speed assuming an isotropic material:

$$S = \sqrt{\frac{E}{3\rho}} \tag{1}$$

where S is the shear wave speed, E is the elastic or Young's modulus, and ρ is the density.

The shear wave elastography ultrasound sequence was compared to measured stiffnesses of agarose phantoms with a dynamic mechanical analyzer (DMA) (RSA-G2, TA Instruments, New Castle, DE, USA). Uniform cylindrical phantoms of varying concentrations of agarose were made for this dynamic mechanical analysis. The test comprised a uniaxial stress-strain compression

measurement assuming cylindrical geometry with a constant linear compression rate of 0.02 mm/s. Stress-strain data were analyzed using commercial software (Trios, TA Instruments, New Castle, DE, USA). The linear slope of the stress-strain curves was reported as the Young's modulus. Over the range of stiffnesses considered (12.3 – 142 kPa) the two measurements agreed on average within 15 kPa.

In comparison to the red blood cell layers, the clot specimen have a finite area whose assessment of stiffness may be confounded by the shear wave elastography technique. Therefore, the stiffness of clots formed from each donor's blood were assessed via the dynamic mechanical analysis protocol as outlined above. For each donor, the Young's modulus was measured on three clots (n = 15 total for each clot type).

3.2.4 Histotripsy insonation

A 1-MHz annular array with a 10-cm aperture and a 9-cm focal length was used to generate histotripsy pulses (Imasonic, Voray sur l'Ognon, France). Each element was driven in parallel by a custom-built class D amplifier and matching network[125]. A total of 4,000 histotripsy pulses of 5-μs duration were delivered to each phantom layer or clot location at a pulse repetition frequency (PRF) of 100 Hz (20 ms total histotripsy exposure time). The focal peak negative pressure of the pulse was 12, 18, or 24 MPa for phantom studies[126]. For the clot study, a fixed peak negative pressure of 18 MPa was employed.

3.2.5 Passive cavitation and plane wave B-mode imaging

Passive cavitation images were used to map the power of acoustic emissions generated by histotripsy-induced bubble clouds. Emissions were passively recorded during the histotripsy insonation with a 128-element L11-4v imaging array connected to an ultrasound research scanner

(Vantage 128, Verasonics, Inc., Kirkland, WA, USA). The imaging array was oriented to monitor cavitation activity along the acoustic axis of the histotripsy transducer (azimuthal axis of the imaging array, Figure 3.1). The received passive cavitation waveforms were processed offline with a frequency-domain delay, sum, and integrate beamformer[127]. To assess bubble cloud echogenicity, the same imaging array was employed to acquire plane wave B-mode images 1 ms following the histotripsy excitation[128]. Due to the data transfer acquisition rate, passive cavitation and plane wave images were acquired every 10th histotripsy pulse (10 Hz acquisition rate, 400 total frames per data set). For a given data set, the acoustic power or grayscale was summed pixel-wise across all frames to generate cumulative passive cavitation or plane wave images, respectively.

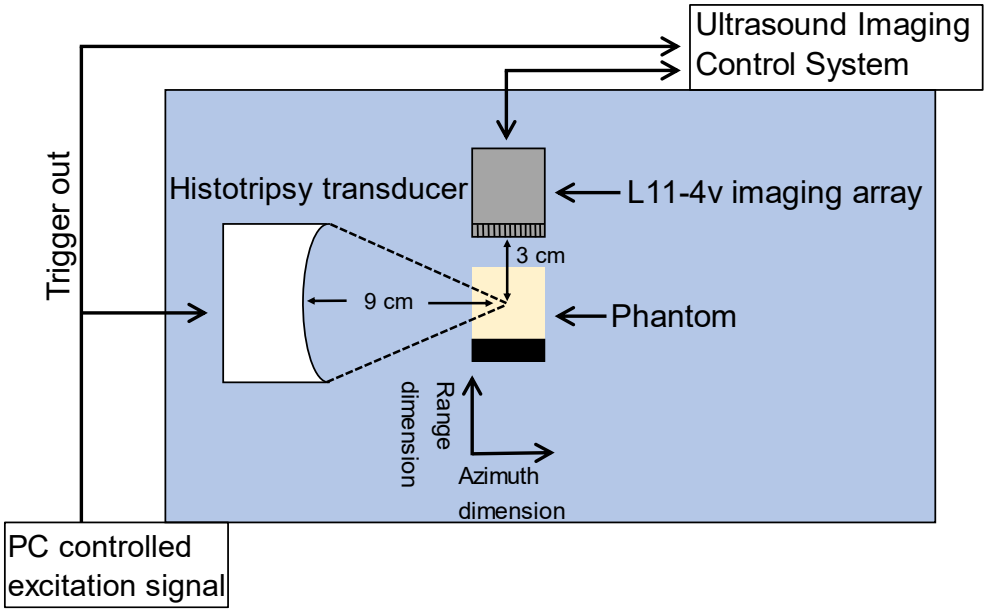

Figure 3.1: Side view of the experimental set up for histotripsy insonation of the agarose phantom, or the clot embedded in the agarose phantom. The L11-4v imaging array was oriented to monitor bubble cloud activity along the azimuthal axis of the histotripsy source.

3.2.6 Experimental protocol

Phantoms were degassed for two hours in an isotonic solution at a partial pressure of 50 kPa, after which they were affixed to a three-axis position system (Thorlabs Inc. Newton, New Jersey, United States) immersed in a tank of degassed (20% dissolved oxygen), filtered (10-μm pore size) deionized water, as noted in Figure 3.1. The distance between the histotripsy focus and the imaging array was fixed at 3 cm. The histotripsy source focal location was determined in the imaging plane by visualizing bubble cloud generation in degassed water. Once located, the focus was then positioned at a depth of 2 cm into the phantom along one of the red blood cell layers (3 layers per phantom). For each phantom, the exposure conditions were randomized for each layer. For clot samples, test pulses were applied to locations lateral (into or out of page for Figure 3.1) to the target zone to ensure uniform bubble activity within the clot. In total, 75 liquefaction zones were generated in 25 different phantoms, and 30 liquefaction zones were generated in ten clots.

3.2.7 Phantom liquefaction and bubble dynamics analysis

After insonification, the phantoms were sectioned and photographed with a DSLR camera (Nikon D3400, 24 MP resolution, Minato, Tokyo, Japan) to visualize liquefaction. Gross images were converted to grayscale and segmented using a grayscale thresholding algorithm[129] to delineate liquefied and intact regions. Cumulative passive cavitation and plane wave B-mode images were co-registered with the gross phantom observation using a custom geometric transformation in MATLAB based on hyperechoic nylon filaments embedded in the phantom (Figure 3.2). Receiver operator characteristic (ROC) analysis was performed to compare passive cavitation and plane wave B-mode images to gross observation of the phantom. The analysis was performed for all

pixels in the image at a fixed depth location of 30 mm. Data was only analyzed across this central line due to the documented limited range resolution of the delay, sum, and integrate beamformer for a linear array geometry (see bottom panel, Figure 3.2)[130].

For the ROC analysis, a pixel was assigned true positive (false positive) when it corresponded to a location with liquefied phantom and the acoustic power or grayscale value was greater than (less than) a pre-defined threshold value. A pixel was assigned a true negative (false negative) value when it corresponded to intact phantom and the acoustic power or grayscale value was less than (greater than) a pre-defined threshold value[110,111] (Figure 3.2). The optimal liquefaction classification based on grayscale or acoustic power was extracted from the ROC curve at the point following Zweig and Campbell[131] for each phantom.

For each phantom layer, the area of the liquefaction zone was tabulated. To quantify the histotripsy bubble dynamics, the maximum pixel value (i.e. acoustic power or grayscale) and the azimuthal location of the maximum pixel were extracted for each data set. Differences in these values were assessed via a one-way analysis of variance test utilizing a Bonferroni correction.

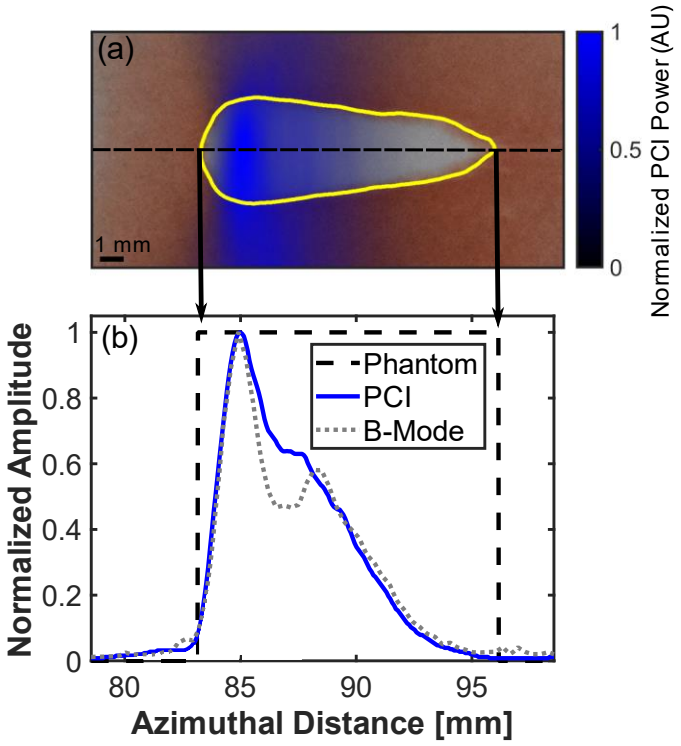

Figure 3.2: (a) The blue colormap overlay represents the passive cavitation imaging (PCI) power registered with processed phantom image. The liquefaction zone is outlined in yellow. The phantom image was analyzed along the entire azimuth through the liquefaction zone (black dashed line) (b) Comparison of PCI acoustic power and plane wave B-mode image grayscale along the dashed line in panel (a) and binary phantom image. For the phantom, values of 1 indicate liquefaction and values of 0 indicate intact phantom. The histotripsy pulse was propagating from left to right in the image. The geometric focal distance of the source is 90 mm.

3.2.8 Blood clot analysis

Following histotripsy exposure, agarose/clot samples were stained with hematoxylin and eosin (H&E) to identify locations of clot liquefaction. Scanned processed slides were assessed via Otsu's method[129] to identify intact and ablated clot. During processing, agarose and liquefied clot sections lost their *in situ* orientation which prohibited registration of processed sections with passive cavitation or plane wave images. Therefore, qualitative analysis was performed of the influence of clot structure on histotripsy ablation. The degree of clot liquefaction was computed as:

$$100 \times \frac{A_C\text{-}A_T}{A_C} \quad (2)$$

where A_T is the area of the residual, treated clot, and A_C is the area adjacent to the histotripsy focal zone (i.e. control sample). A one-sample Student's t-test was used to test if clot loss was significantly greater than 0% (a fully intact clot). The averaged acoustic power or grayscale of the bubble cloud within the clot was assessed with passive cavitation or plane wave imaging, respectively. Clot area loss and averaged acoustic power/grayscale were also analyzed via a paired-sample Student's t-test for differences between clot types.

3.2.9 Statistical analysis

A one-way ANOVA multiple comparisons test using the Bonferroni method was applied to identify significant differences between phantom stiffnesses for maximum passive cavitation/plane wave B-mode values, the location of maximum passive cavitation/plane wave B-mode values, and liquefaction areas. The Pearson's correlation coefficient and its level of statistical significance were calculated for passive cavitation and plane wave B-mode liquefaction threshold values as a function of phantom stiffness. The area under the curve was tabulated for each arm, and the significance relative to 0.5 (i.e. guessing) was determined according to DeLong *et al.*[132]. The sensitivity, specificity, positive predictive value, and negative predictive value were extracted from the ROC curve at the optimal operating point. Paired-sample t-tests were used to test for significant differences in clot metrics (area loss, area-averaged plane wave B-mode value, and area-averaged acoustic emissions) between clot types.

3.2.10 Analytic model

The maximum size of a bubble nucleus exposed to a shocked histotripsy pulse of one cycle duration in an elastic medium can be computed as:

$$R_{MAX} = \left[R_0 + \sqrt{\frac{2P_0\xi}{9\rho}}\tau\right]\left[\frac{\xi \mathrm{P}_0}{3p_{EFF}} + 1\right]^{1/3} \quad (3)$$

where P_0 is the ambient pressure of the medium (0.1 MPa) and ρ is the fluid density (1000 kg/m^3). The parameters ξ and τ incorporate the effects of surface tension, viscosity, and medium inertia[133]. The medium stiffness is also incorporated into these terms assuming a Kelvin-Voight model, which has been validated for soft tissues in the 3-13 MHz range[134]. The initial bubble radius R_0 was set to 20 nm, which will provide an upper estimate to the maximum bubble size[126]. For a shock-scattering pulse, the effective pressure, p_{EFF}, can be defined as the magnitude of the peak negative pressure, $|p_N|$[126].

3.3 Results

3.3.1 Phantom liquefaction

For all insonation conditions, phantom liquefaction was initiated (Figure 3.3). The liquefaction zone was continuous, resembling a tadpole shape with a large head and a tail that narrows distally[111,119]. For a given phantom stiffness, the liquefaction area increased with peak negative pressure of the histotripsy pulse ($p < 0.05$). The area of liquefaction was independent of the phantom Young's modulus for a given peak negative pressure of the histotripsy pulse ($p > 0.05$) (Figure 3.4).

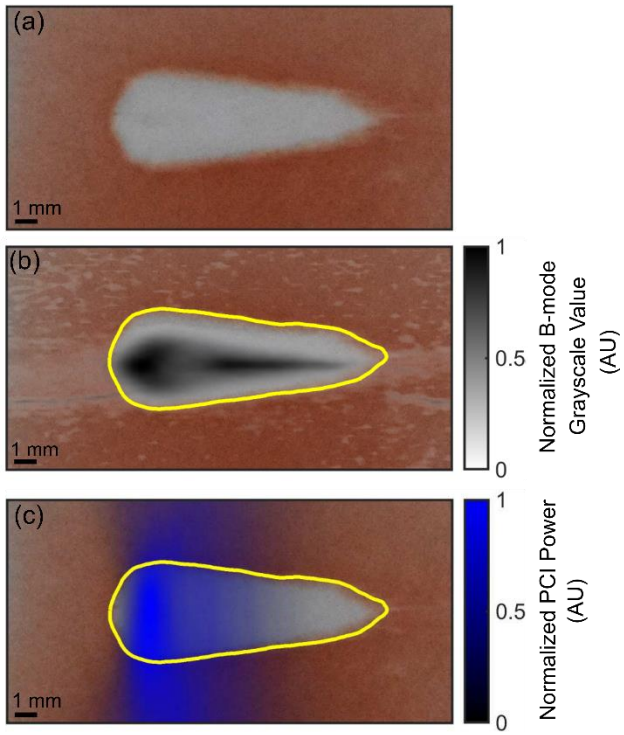

Figure 3.3: (a) Phantom liquefaction zone (white) generated by histotripsy insonation. (b) Comparison of co-registered plane wave B-mode image (black & white colormap overlay) and processed phantom image. (c) Comparison of co-registered passive cavitation imaging (PCI) and processed phantom image. Both the passive cavitation and plane wave B-mode images were summed over the duration of the histotripsy insonation to create cumulative images. For panels (b) and (c), the liquefaction zone borders are outlined in yellow. The histotripsy pulse (24 MPa peak negative pressure) propagated from left to right in the image. The bar in the lower left corner of each image corresponds to 1 mm.

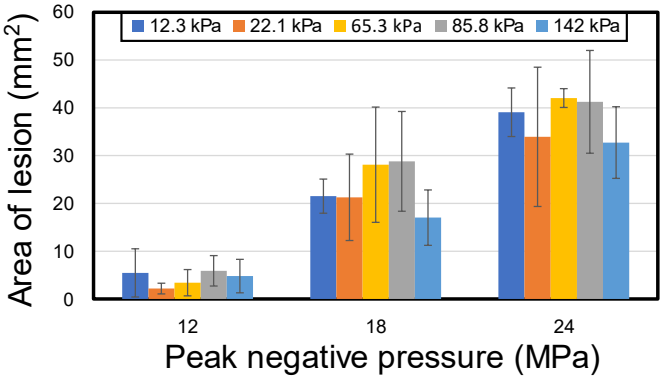

Figure 3.4: Area of phantom liquefaction as a function of peak negative pressure and phantom stiffness. No significant differences were observed between liquefaction areas for a given peak negative pressure.

3.3.2 Correlation of imaging with phantom liquefaction

The resulting ROC curves comparing the ability of plane wave B-mode image (grayscale) or passive cavitation imaging (acoustic power) to predict the phantom liquefaction zone are shown in Figure 3.5. For each phantom stiffness, the area under the ROC curve (AUROC) was significantly greater than 0.5 for both plane wave and passive cavitation imaging. The AUROC generally increased with increasing stiffness.

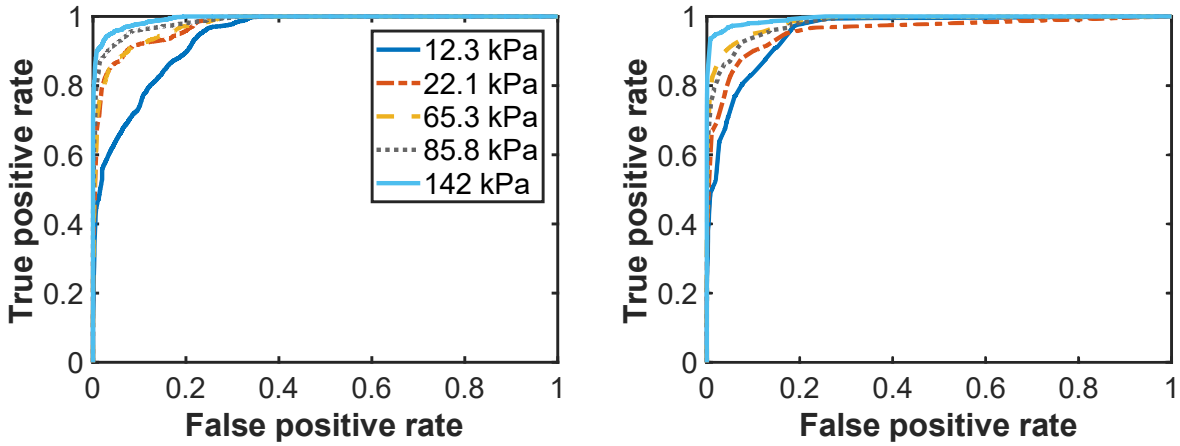

Figure 3.5: Receiver operator characteristic curve across stiffnesses for plane wave B-mode imaging (left) and passive cavitation imaging (right). The legend applies for both sub-figures and denotes the Young's modulus for each phantom.

Statistics extracted from the ROC curves at the optimal operating point (e.g. AUROC, sensitivity, specificity, accuracy, positive predictive value, and negative predictive value) are shown in Table 3.2. The predictive ability of passive cavitation and plane wave B-mode imaging for phantom liquefaction were similar for most categories. A strong increase in liquefaction sensitivity was observed with the phantom stiffness, from 0.512 – 0.877 for plane wave B-mode imaging and from 0.582 – 0.915 for passive cavitation imaging.

Table 3.2: Comparison of statistics extracted from receiver operator characteristics for plane wave B-mode (top) and passive cavitation imaging (PCI, bottom) grouped by stiffness (all peak negative pressures), including the area under the receiver operator characteristic (AUROC), accuracy, specificity, positive predictive value (PPV), and negative predictive value (NPV).

B-mode						
Young's modulus	**AUROC**	**Accuracy**	**Sensitivity**	**Specificity**	**PPV**	**NPV**
12.3 ± 3.7 kPa	0.940 ± 0.041	0.939 ± 0.020	0.512 ± 0.181	0.990 ± 0.007	0.845 ± 0.126	0.945 ± 0.020
22.1 ± 7.7 kPa	0.975 ± 0.027	0.963 ± 0.018	0.772 ± 0.209	0.986 ± 0.006	0.858 ± 0.025	0.974 ± 0.024
65.3 ± 8.5 kPa	0.976 ± 0.012	0.968 ± 0.009	0.718 ± 0.071	0.992 ± 0.005	0.891 ± 0.057	0.974 ± 0.009
85.8 ± 11.9 kPa	0.982 ± 0.015	0.972 ± 0.016	0.698 ± 0.328	0.994 ± 0.005	0.948 ± 0.048	0.975 ± 0.015
142 ± 22 kPa	0.993 ± 0.006	0.986 ± 0.006	0.877 ± 0.036	0.995 ± 0.003	0.935 ± 0.034	0.990 ± 0.004
PCI						

Table 3.2, continued:

Young's modulus	AUROC	Accuracy	Sensitivity	Specificity	PPV	NPV
12.3 ± 3.7 kPa	0.958 ± 0.021	0.948 ± 0.015	0.582 ± 0.090	0.991 ± 0.006	0.884 ± 0.094	0.952 ± 0.010
22.1 ± 7.7 kPa	0.958 ± 0.026	0.959 ± 0.014	0.657 ± 0.098	0.993 ± 0.003	0.918 ± 0.028	0.962 ± 0.014
65.3 ± 8.5 kPa	0.985 ± 0.007	0.978 ± 0.004	0.799 ± 0.033	0.994 ± 0.004	0.929 ± 0.044	0.982 ± 0.003
85.8 ± 11.9 kPa	0.980 ± 0.011	0.967 ± 0.006	0.727 ± 0.117	0.992 ± 0.007	0.886 ± 0.145	0.972 ± 0.012
142 ± 22 kPa	0.994 ± 0.006	0.991 ± 0.005	0.915 ± 0.055	0.998 ± 0.002	0.968 ± 0.026	0.993 ± 0.006

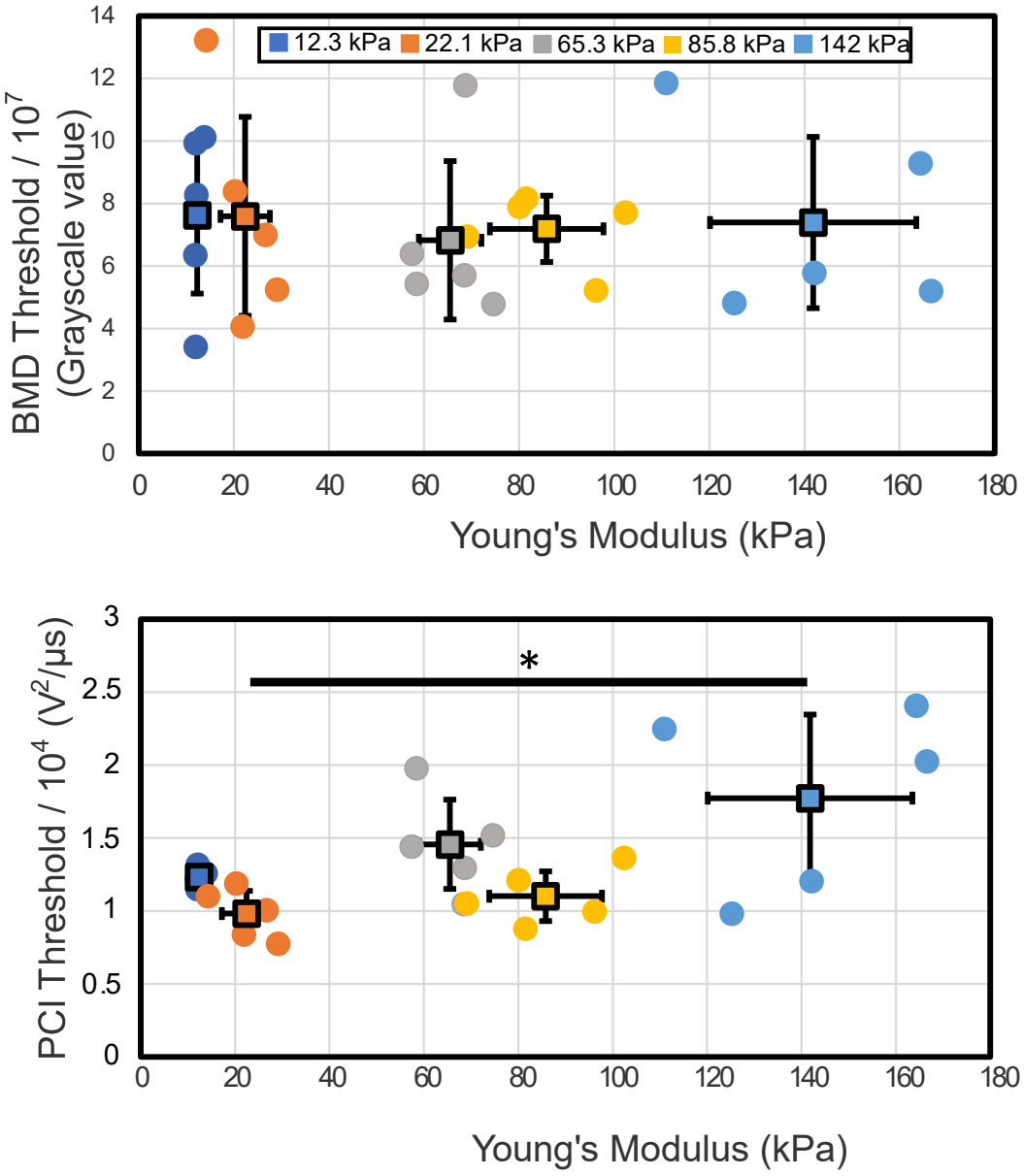

Figure 3.6: (Top) plane wave B-mode grayscale and (Bottom) passive cavitation imaging acoustic power liquefaction threshold as a function of Young's modulus. Circles denote thresholds for individual phantoms, and squares denote the average for a given concentration of agarose. The legend is the same for both panels. The bar with asterisk denotes a significant difference between threshold values for different stiffness groups.

The optimal operating point on the ROC curve used to determine the threshold acoustic power or grayscale for phantom liquefaction is reported in Figure 3.6. No trend was observed in the grayscale value with the phantom stiffness ($p > 0.05$), and there was no difference in the threshold when grouped by agarose concentration. For passive cavitation imaging, a weak but significant trend was observed in the acoustic power threshold for phantom liquefaction ($R^2 = 0.522$, $p = 0.01$). When grouped by agarose concentration, only two arms displayed a significant difference in the liquefaction threshold based on acoustic power (142 and 22.1 kPa, Figure 3.6).

3.3.3 Phantom bubble cloud activity

Within the liquefaction zone, bubble cloud activity indicated by hyperechogenicity and acoustic emissions was observed for all experimental conditions (Figure 3.3). For the 12 MPa peak negative pressure histotripsy exposures, bubble activity was noted to be more sporadic than for larger peak negative pressure pulses. Limited trends were observed between the bubble cloud activity and the phantom stiffness. For a given peak negative pressure, no significant difference was observed in peak acoustic power or peak grayscale value across stiffnesses except in two instances, as noted in Figure 3.7 (grayscale values generated in phantoms with 12.3 kPa and 142 kPa Young's modulus for the 12 MPa peak negative pressure insonations, and acoustic emissions generated in phantoms with 22.1 and 142 kPa Young's modulus for the 18 MPa peak negative pressure insonations).

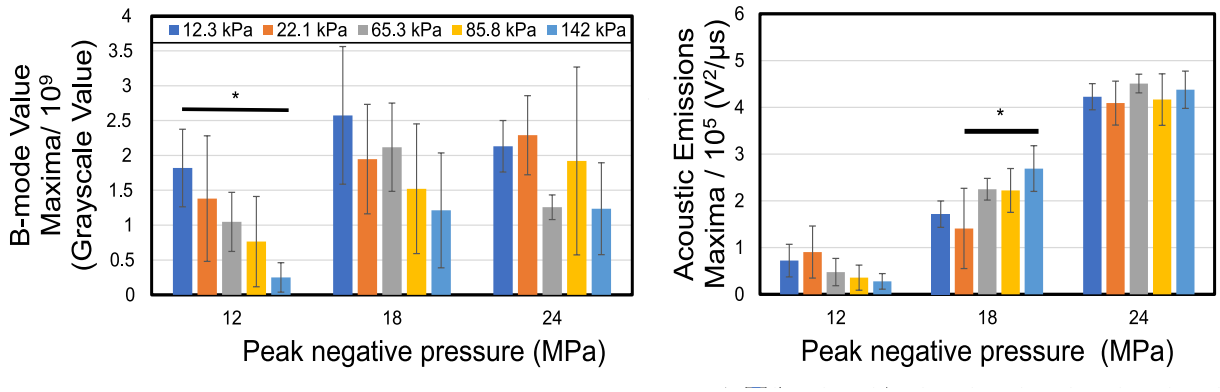

Figure 3.7: (Left) Maximum plane wave B-mode grayscale and (right) maximum passive cavitation imaging acoustic power as a function of peak negative pressure and stiffness. Asterisk with bar denotes statistically significant difference between the maxima of two stiffnesses within a pressure group. The legend denoting phantom stiffness is the same for both panels.

The azimuthal positions of the maximum bubble cloud emissions and maximum plane wave B-mode values were independent of the phantom stiffness for a given peak negative pressure of the histotripsy pulse (Figure 3.8). For a given phantom stiffness, the location of maximum bubble cloud emissions shifted closer to the histotripsy source as the peak negative pressure increased. The most hyperechoic portions of the bubble cloud were not dependent on the peak negative pressure of the histotripsy source.

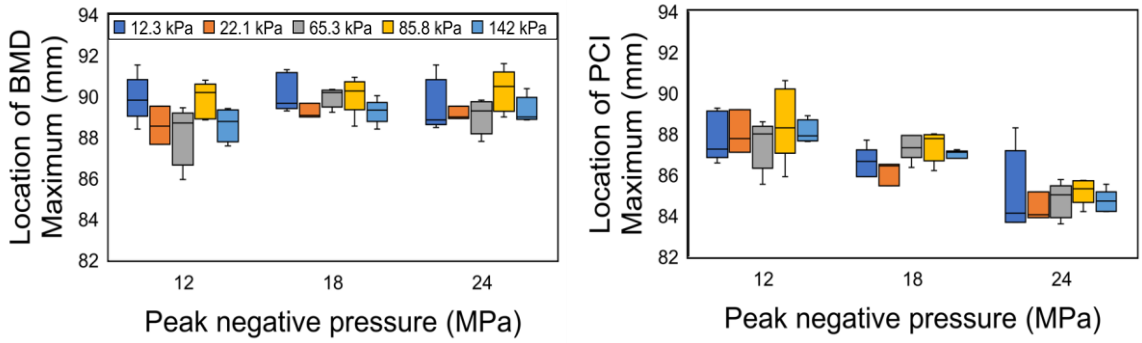

Figure 3.8: Azimuthal location of (left) plane wave B-mode grayscale and (right) passive cavitation imaging acoustic power maxima. Horizontal lines denote the median. Smaller values indicate positions closer to the histotripsy source while larger values indicate positions farther from the histotripsy source. The legend denotes phantom stiffness. The geometric focus corresponds to 90 mm.

3.3.4 In vitro clot histotripsy exposure

The Young's modulus of mildly-retracted and well-retracted clots was found to be 2.94 ± 0.95 kPa and 4.26 ± 1.30 kPa, respectively. Histotripsy exposed sections of both clot models were characterized by a marked reduction in red blood cells and moderate reduction in the extent of the fibrin mesh and platelets (Figure 3.9). There was no observed difference in the area of histotripsy ablation between the clot models (Table 3.3) ($p > 0.05$).

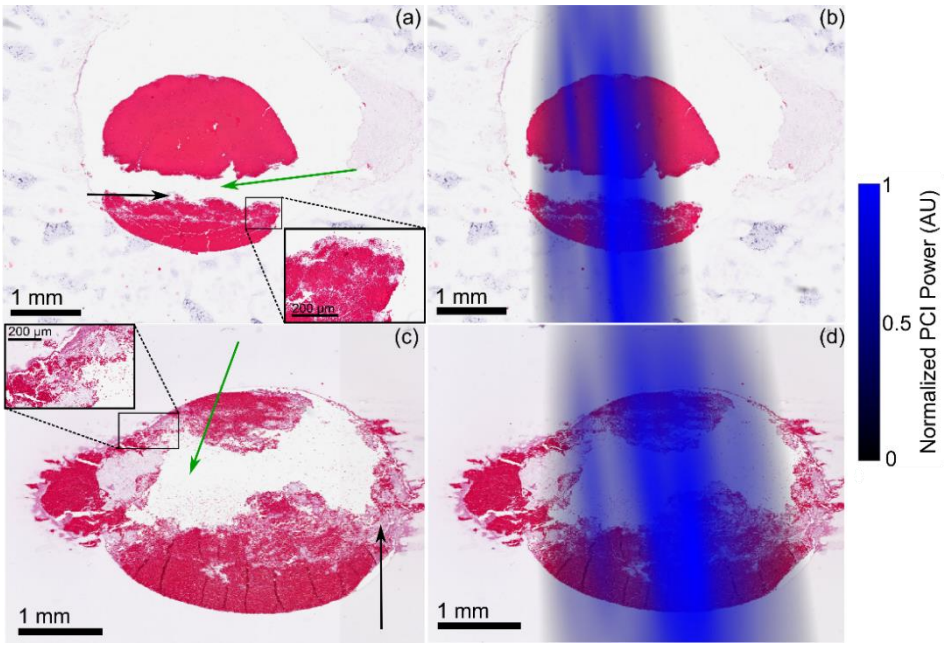

Figure 3.9: Hematoxylin and eosin stained clot sections. (a) Flint clot sample (b) Flint clot sample with passive cavitation image overlay (c) Borosilicate clot sample (d) Borosilicate clot sample with PCI overlay. The black bars denote a length of 1 mm. The histotripsy pulse propagated from left to right in the image. The black arrows mark representative areas of residual fibrin, and the green arrows mark areas of complete liquefaction. The purple areas outside of the clot in subfigures (a) and (b) are histological artifacts.

Table 3.3: Clot area loss measured for flint clots and borosilicate clots, and area-averaged grayscale value and acoustic emissions contained within the clot. A clot loss of 0% signifies the clot was unaffected by the histotripsy pulse relative to control samples. Bold font indicates a significant difference between clot types.

Clot type	Clot loss (% area)	Grayscale averaged over area (grayscale/mm^2)	Emissions averaged over area ($V^2/\mu s\ mm^2$)
Flint glass	32.8 ± 23.4	**189** ± 9	$9.59 \times 10^7 \pm 0.56 \times 10^7$
Borosilicate glass	33.1 ± 12.8	**177** ± 17	$9.15 \times 10^7 \pm 2.69 \times 10^7$

Strong bubble activity was noted inside the clot for all insonifications (Figure 3.9). On occasion, bubble activity was also noted in the agarose surrounding the clot. The area-averaged power of acoustic emissions for bubble cloud activity within the clot cross section was not significantly different between the two models ($p > 0.05$). An increase in bubble cloud echogenicity was noted in the flint glass (mildly retracted) clots relative to the borosilicate glass (well retracted) clots ($p < 0.05$) (Table 3.3).

3.3.5 In silico model

Analytic computations of the maximum bubble size as a function of the medium stiffness are shown in Figure 3.10. As the medium stiffness increased beyond 20 MPa, the maximum bubble size decreased rapidly as a function of the Young's modulus for a fixed peak negative pressure of the histotripsy pulse. For medium stiffnesses between 1 and 142 kPa (the range of phantom stiffness considered in this study), the maximum bubble size is predicted to decrease by 0.46%, 0.31%, and 0.23% at 12 MPa, 18 MPa, and 24 MPa peak negative pressure, respectively.

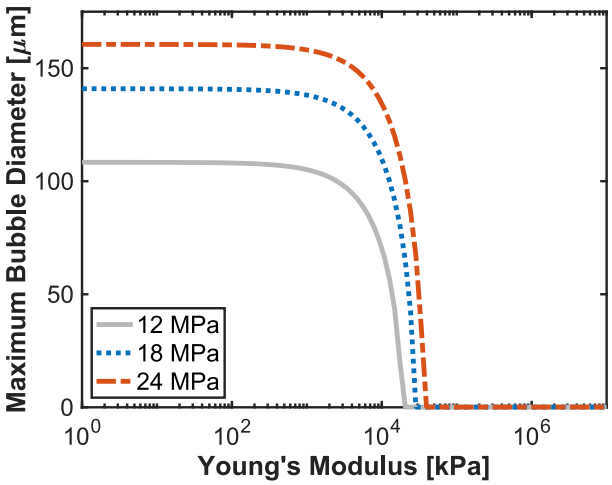

Figure 3.10: Analytic computation for the maximum bubble diameter as a function of Young's modulus and peak negative pressure.

3.4 Discussion

3.4.1 Liquefaction threshold dependence on material stiffness

In this study, the histotripsy bubble activity necessary for liquefaction was only mildly dependent on agarose stiffness. Over the Young's modulus range 12.3–85.8 kPa, there was no change in the bubble activity necessary for phantom liquefaction. No change was observed in the degree of liquefaction for well and mildly-retracted clots, despite the variation in stiffness between the two models. These results are consistent with a previous study that found minimal changes in the degree of histotripsy-induced erosion over the range of Young's moduli considered here[135]. The lack of change in the bubble dynamics for less-stiff phantoms may be in part due to the shocked pulses employed in this study. If the medium's Young's modulus is less than 1.5 MPa, analytic computations indicate the positive pressure of the shock wave has a larger influence on bubble expansion than the medium elastic properties[103]. The observations in this study may not extend to

the intrinsic-threshold regime of histotripsy where the compressional phase of the acoustic excitation has little influence on the bubble dynamics[136,137].

Only two groups of phantoms displayed a significant difference in the emission threshold associated with liquefaction tracked with passive cavitation imaging (142 ± 22 kPa and 22.1 ± 7.7 kPa phantoms). A weak but significant correlation was noted between the phantom stiffness and the liquefaction threshold tracked with passive cavitation imaging ($p < 0.05$). These observations may reveal that the material stiffness has a mild influence on the overall outcome for histotripsy therapy over the range of Young's moduli considered in these studies. Analytic calculations of bubble expansion indicated that the medium stiffness has a small, but observable, influence on the bubble dynamics (Figure 3.10). The increase in liquefaction threshold with phantom stiffness may be a reflection of the ultimate tensile strength dependence on agarose concentration[138,139]. The relationship between true tensile stress and agarose concentration has a steeper slope for low-frequency assessment than that observed here (1.2 slope for low frequency assessment of true strain[138] vs. agarose concentration in comparison to 0.5 for acoustic power liquefaction threshold vs. agarose concentration observed here). The variation in slopes may reveal the difference in behavior of the agarose between the high strain rates induced by the microsecond time scale of the bubble cloud and the aforementioned low-frequency assessment of stress and strain.

It is important to make a distinction between the threshold peak negative pressure for bubble cloud nucleation and the acoustic emission threshold associated with liquefaction measured in this study. The peak negative pressure necessary for bubble cloud formation increases significantly over the Young's modulus range of 1.5 – 38 kPa[135]. In contrast, the acoustic power threshold for phantom liquefaction did not change significantly for Young's moduli less than 85.8 kPa in this study. The power of acoustic emissions can be taken as an indication of the bubble cloud

mechanical activity. The findings here indicate that, following nucleation, the degree of bubble cloud mechanical activity necessary for liquefaction is largely independent of the material stiffness.

3.4.2 Imaging modality for prediction of histotripsy liquefaction

The AUROC values were similar for passive cavitation and plane wave B-mode imaging, in contrast to previous observations[110]. The discrepancy between the two studies may in part be due to the experimental design. The current study used an agarose phantom with a thin red blood cell layer, whereas studies demonstrating better prediction of liquefaction with passive cavitation imaging utilized ex vivo liver or an evaporated milk phantom[110,119]. The latter materials are more attenuating compared to the agarose phantoms in this study which will reduce bubble cloud visualization on plane wave images[128,140]. Medium attenuation also alters the shape of the structure of histotripsy bubble activity. Liquefaction zones appeared continuous in this study, whereas two disjoint zones were generated in the attenuating phantom[119]. A lower pulse repetition frequency was used in the previous study in comparison to this study (20 Hz vs. 100 Hz), which would minimize the likelihood of persistent bubble clouds[141]. The application of histotripsy pulses at a high rate would activate mechanical activity at discrete locations in the focal zone. While passive cavitation and plane wave B-mode imaging had similar predicative abilities in this phantom study, passive cavitation imaging maintains robust liquefaction prediction in clinically relevant attenuating media.

For both PCI and plane wave B-mode imaging, the AUROC and sensitivity for predicting phantom liquefaction increased with the Young's modulus. The increased sensitivity to liquefaction can be attributed to a decrease in the number of false negatives with increasing phantom stiffness (Figure 3.11). It is unknown why the false negatives decreased with the phantom

stiffness. A more uniform distribution of acoustic emissions throughout the liquefaction zone would lead to a decrease in false negatives, although no strong changes are observed in the bubble cloud dynamics with the phantom stiffness (Figure 3.7 and Figure 3.8). Nevertheless, these data indicate both PCI and plane wave imaging are sensitive to the liquefaction of stiff tissues.

Due to variant response of the agarose and clot, reliable registration between passive cavitation images and clot samples could not be performed. Therefore, qualitative parameters were extracted to gain insight on the bubble response in a varying stiffness tissue model. There was no difference in the clot loss metric or the area-averaged acoustic emissions between the clot models. This indicates that the degree of bubble cloud mechanical activity necessary for liquefaction is similar between the two clot models. A significant difference was observed in the area-averaged grayscale values between mildly and well-retracted clots (Table 3.3).

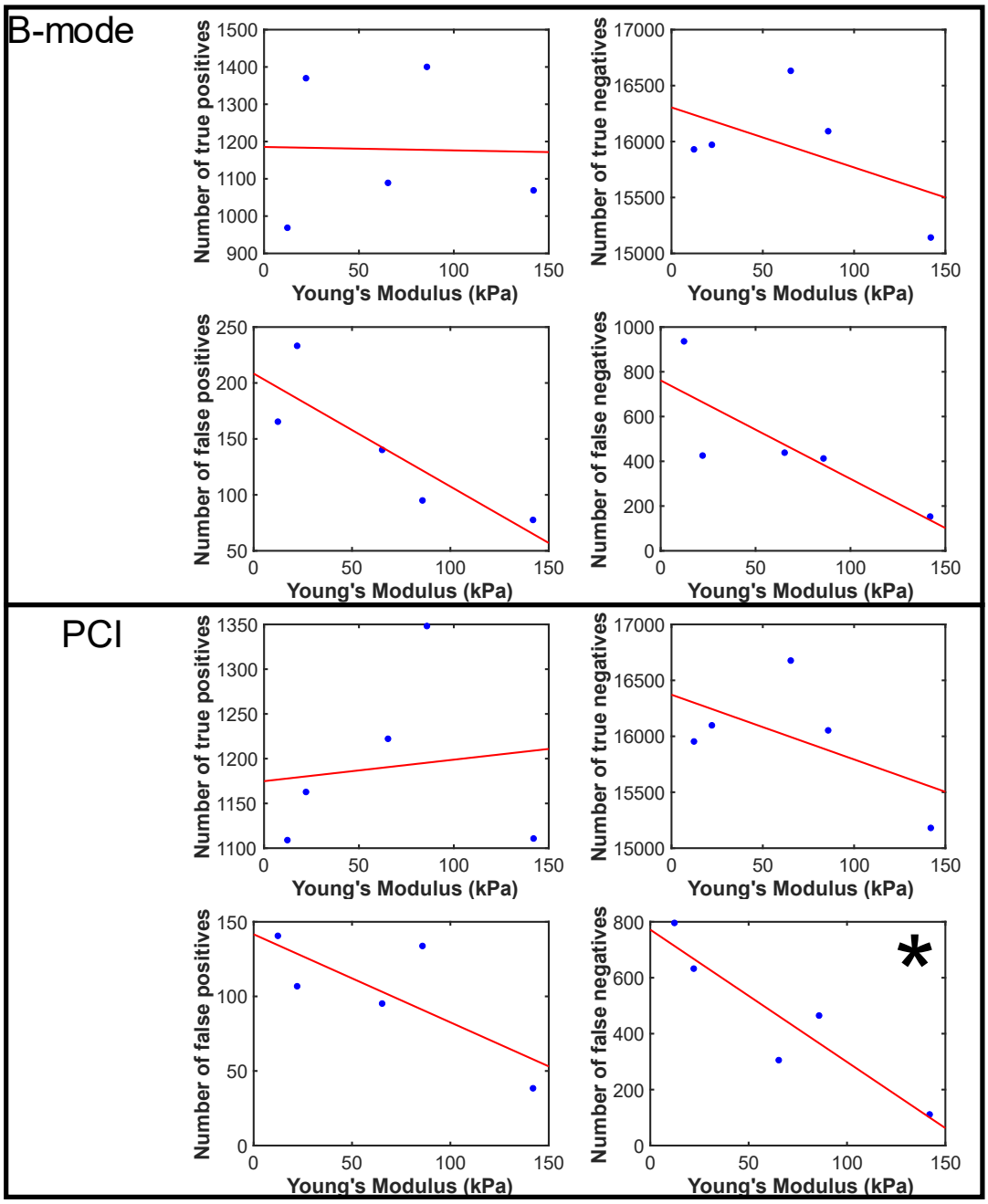

Figure 3.11: Number of true positives, true negatives, false positives, and false negatives detected by plane wave B-mode (top) and passive cavitation imaging (bottom) as a function of Young's modulus (blue dots) with a best fit line (red line). Only the PCI false negative trend (noted with asterisk) was significantly correlated with elasticity, with a Pearson's correlation coefficient of -0.9230 ($p < 0.05$). There was no significant trend with plane wave B-mode imaging ($p > 0.05$).

The variation in bubble cloud echogenicity may be in part due to the structural differences between the clots, rather than a change in bubble dynamics. Indeed, a significant difference was observed in the clot stiffness between the two models, indicating structural differences which may be reflected as changes in echogenicity on the plane wave B-mode images. Chronic thrombi with collagen or calcifications would further alter the clot echogenicity[142], heightening the need for a medium-independent assessment of ablation with a modality like PCI.

3.4.3 Limitations

Agarose phantoms were used to provide consistent, specified mechanical and acoustic properties. However, there are important differences between agarose and tissue. Agarose phantoms were degassed prior to histotripsy exposure. Thus, the total amount of dissolved gases, and therefore bubble dynamics, within the agarose phantoms may not be representative of *in vivo* conditions[143]. Likewise, the clots for this study were formed *in vitro*. While medium stiffness can be used as a criterion in delineating acute from chronic clots, the clotting cascade and formation of stiff, chronic thrombi is a complex process[144,145]. With the current *in vitro* model, there is neither fibroblast infiltration for collagen nor calcification present to model a chronic thrombus[144]. Features of chronic clots besides stiffness were not considered in this study and should be investigated further.

Ultrasound images and gross observations of liquefaction were analyzed in a two-dimensional plane, whereas the liquefaction zone occupies a three-dimensional volume. Furthermore, the range resolution of the delay, sum, and integrate algorithm is limited, and ROC curves were constructed based on phantom, passive cavitation, and plane wave B-mode data at a fixed range position. Future studies should consider a modified receiver geometry or an alternative beamforming algorithm for improved resolution of the passive cavitation image[115,146]. The acoustic power or

grayscale threshold for phantom liquefaction reported here will vary based on the array sensitivity and the depth of the histotripsy excitation. Such issues can be overcome with system-independent assessment of the acoustic power based on the element-by-element sensitivity[147] or by compensating for the attenuation of the acoustic path[148]. Current approaches to quantitate scattering also do not account for dense bubble clouds, such as those generated during histotripsy[115]. In addition, the optimal operating points may vary between the phantom and living tissue due to differences in structural composition, and may be tissue specific.

In this study, phantom liquefaction occurred over the course of approximately 40 s (4000 pulses delivered at 100 Hz). This may be excessive for complete liquefaction of the focal zone. Passive cavitation imaging in the future may be used to monitor cavitation emissions, which can then be used as a decision-making tool to determine the optimum treatment length. Preventing excessive liquefaction will reduce treatment time and mitigate off-target or critical structure damage.

3.5 Conclusions

In this study, histotripsy pulses were generated in agarose phantoms of Young's moduli ranging from 12.3 to 142 kPa, and *in vitro* clot models with mild and strong platelet-activated retraction. The acoustic power (mapped with passive cavitation imaging) associated with phantom liquefaction was weakly correlated with the phantom stiffness. No change in the acoustic power associated with agarose liquefaction was observed for phantom stiffnesses over the range 12.3 to 85.8 kPa. No general change in the bubble cloud grayscale or power of acoustic emissions was observed over the range of phantom stiffnesses used in this study. Despite the variation in clot retraction, there was no change in the bubble cloud dynamics or degree of liquefaction between

the two clot models. Overall, these results indicate that a fixed dose of bubble activity can be utilized to predict histotripsy liquefaction over a wide range of media stiffnesses.

CHAPTER 4

CLOT DEGRADATION UNDER THE ACTION OF HISTOTRIPSY BUBBLE ACTIVITY AND A LYTIC DRUG

The work presented in this chapter has been accepted for publication as: S.A. Hendley, J.D. Paul, A.D. Maxwell, K.J. Haworth, C.K. Holland, K.B. Bader, *Clot degradation under the action of histotripsy bubble activity and a lytic drug*, IEEE-TUFFC (2021).

4.1 Introduction

Histotripsy bubble activity can also be used to break up clots in the absence of a lytic[23]. There are advantages, however, to combining thrombolytic approaches with the mechanical destruction caused by histotripsy insonation schemes. Thrombolytic approaches have limited efficacy for clots nonresponsive to lytic[122]. In the absence of lytic, histotripsy bubble activity may undertreat clot near the vessel wall[159]. Combing histotripsy with a lytic therapy may therefore provide an effective means to promote clot degradation. Preclinical studies have demonstrated that histotripsy combined with lytic significantly enhances overall treatment efficacy[23,24]. Two primary mechanisms are hypothesized to contribute to combined histotripsy and lytic therapy: 1.) Hemolysis due to the mechanical strain of bubble cloud expansion within the clot [157,160], and 2) Enhanced fibrinolysis caused by increased penetration of lytic into the thrombus due to vigorous bubble cloud oscillations[35].

The aim of this study was to gauge the contributions of hemolysis and fibrinolysis to the overall treatment efficacy for the combination therapy. Clots were exposed to rt-PA and histotripsy pulses using a venous flow model, as described previously[24]. A transducer designed for the treatment of deep vein thrombosis was used to deliver histotripsy pulses. The range of insonation conditions (i.e. peak negative pressure and pulse duration) span those explored in other histotripsy clot ablation studies[24,159]. The percent change in clot mass was used as the overall metric of

treatment efficacy. Assays to measure hemoglobin and D-dimer within the perfusate following histotripsy and lytic exposure were used to quantify the contribution of mechanical and fibrinolytic effects, respectively. A secondary aim of this study was to determine the role of bubble activity in promoting hemolysis or fibrinolysis. To quantify bubble activity, passive cavitation imaging was used to map the pressure generated by histotripsy bubble cloud activity[127]. Linear regression analysis was conducted to assess the relationship between hemolysis, fibrinolysis and overall treatment efficacy. Additional linear regression analysis was conducted to compare the effect of bubble activity on mechanical hemolysis and chemical fibrinolysis. Findings were also compared to gross histological observation of the histotripsy zone in the clot.

4.2 Materials & Methods

4.2.1 Venous whole-blood model

Human whole-blood clots were manufactured following an established Internal Review Board-approved protocol (University of Chicago IRB #19-1300)[24,82]. Briefly, venous human whole blood was drawn from 11 volunteer patients undergoing invasive catheterization procedures at the University of Chicago Medicine cardiac catheterization laboratory following informed consent. Aliquots of blood (2 mL volume) were transferred to borosilicate Pasteur pipettes (Fisher Scientific, Pittsburg, PA, USA), heated at 37°C for 3 hrs., stored for a minimum of 3 days at 4°C to ensure full retraction[161], and used within 2 weeks.

4.2.2 Preparation of recombinant tissue-type plasminogen activator and human fresh-frozen plasma

Lytic (rt-PA) was obtained from the manufacturer (Activase, Genetech, San Francisco, CA, USA) as lyophilized powder. Each vial was mixed with sterile water to a concentration of 1 mg/mL, aliquoted into 0.5 mL centrifuge tubes, and stored at −80°C. Aliquots were thawed within 3 years of freezing and used within 4 h of thawing for each experiment. When stored in this manner, rt-PA is stable over the course of at least seven years[162]. Human fresh-frozen type O plasma was procured from a blood bank (Vitalant, Chicago, IL, USA), aliquoted, and stored at −80 °C prior to use.

4.2.3 Histotripsy insonation

Histotripsy pulses were generated by a custom-made eight-element, elliptically-focused transducer (9 cm major axis, 7 cm minor axis and 6 cm focal length)[163]. The fundamental frequency of the transducer was 1.5 MHz, and the resultant focal zone under typical driving conditions had a -6 dB focal width of 4.27 mm x 0.66 mm x 0.70 mm for the axial direction, and the major and minor axes, respectively, relative to the transducer. An L11-5v imaging array (Verasonics, Inc., Kirkland, WA, USA) was placed through a co-axial opening on the histotripsy transducer to provide image guidance using a research ultrasound scanner (Vantage 128, Verasonics, Inc., Kirkland, WA, USA). The histotripsy transducer elements were excited in parallel by a custom designed and built class D amplifier and matching network[125,164].

4.2.4 Experimental procedure

Prior to histotripsy exposure, the clot was cut to 1 cm in length and introduced into a venous flow model[24] (Figure 4.1). The model was composed of a syringe pump (EW-74900-20, Cole-Parmer,

Vernon Hills, IL, USA) that drew plasma through 6.35-mm-inner-diameter and 0.79-mm wall thickness latex tubing (McMaster-Carr, Elmhurtst, IL, USA) at a rate of 0.65 mL/min. This flow rate was chosen to mimic the flow observed for a partially occluded iliofemoral vessel[165]. The plasma was maintained at physiologic temperature by submerging it in a bath of degassed (20% dissolved oxygen), reverse osmosis water heated to 37.3 ± 0.5 °C. The flow channel was perfused with plasma alone, or plasma and rt-PA (2.68 μg/mL) five minutes before insonation began[166]. This lytic concentration was chosen to correspond to previous pharmacomechanical studies[166].

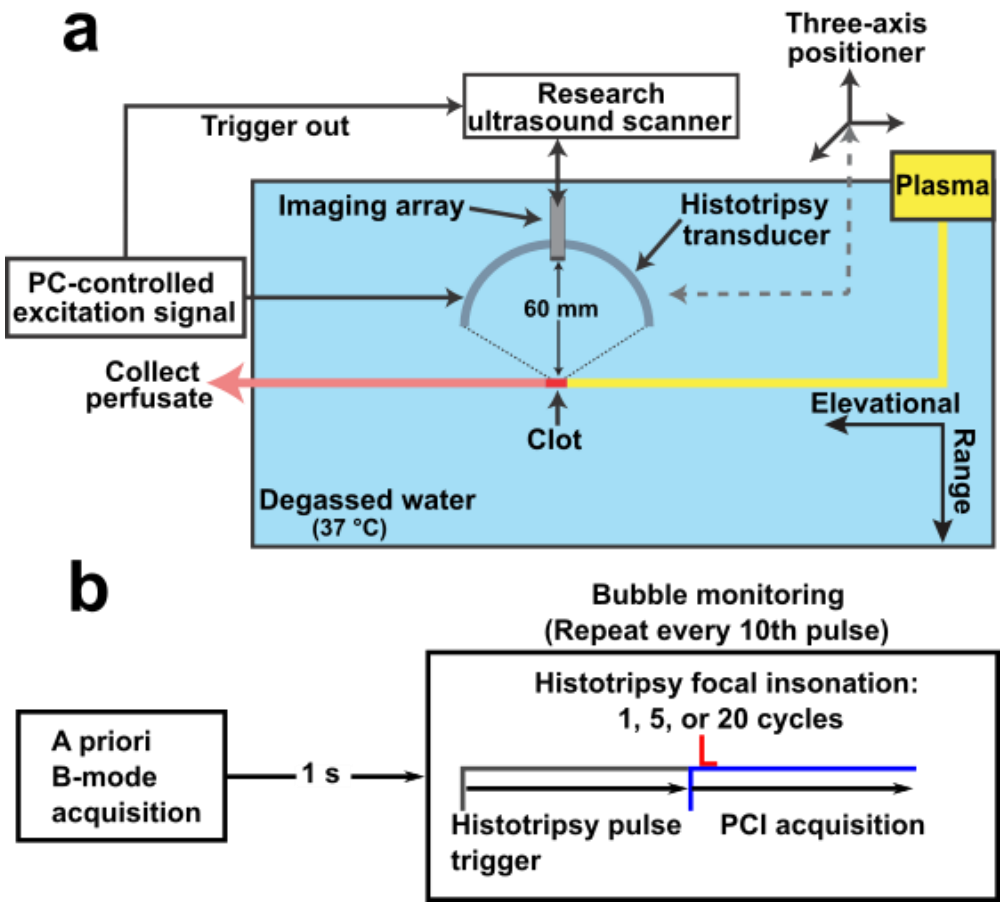

Figure 4.1: Experimental setup. (a) Schematic of the flow channel setup. The flow was from right to left in this diagram. The histotripsy source moves along the direction of flow. (b) Timing diagram for histotripsy insonation and image data acquisition. To identify the clot location, a B-Mode ultrasound image was taken prior to the application of the histotripsy therapy. During the application of histotripsy, acoustic emissions generated by the bubble could were acquired passively and beamformed to generate passive cavitation images (PCI) offline (see Figure 4.2).

Translation of the histotripsy source along the length of the clot was achieved with three orthogonal motorized linear stages (BiSlide, Velmex Inc., Bloomfield, NY, USA). The clot was targeted as described previously[24,37]. Briefly, the location of the transducer focus in the plane of the confocal imaging array was determined by generating histotripsy pulses in the degassed water outside the lumen. The bubble cloud appeared hyperechoic in the imaging plane as described previously[24,37,167]. Once the location of the focus was determined, the transducer was aligned with the distal end of the clot relative to the pump (far right, Figure 4.1). Waypoints (i.e. positions of the motors where the bubble cloud was contained within the clot) were set every 5 mm along the length of the clot. A custom script interpolated an automated path for the transducer along the length of the clot with a 0.5 mm step size (~ 20 steps per clot). The step size distance was smaller than the -6 dB width of the focal zone along the dimension of transducer translation. At each location, 2000 pulses were applied at a 40 Hz rate, consistent with other thrombotripsy studies[23,24,26]. The total treatment time was 25 minutes per clot. The insonation pulse had a duration of one, five, or twenty cycles (0.67, 3.33, or 13.33 μs, respectively). For one-cycle pulses, peak negative pressures of 0, 25, 30, or 35 MPa were explored. A 35 MPa peak negative pressure was used for five and twenty cycle arms. A minimum of 8 clots were used for each treatment arm (122 total).

4.2.5 Imaging assessment of bubble activity

At each insonation location, a B-mode ultrasound image (128 elements, 7.81 MHz center frequency) was acquired prior to histotripsy exposure and segmented manually to denote the area of the clot (Figure 4.2). During the insonation, acoustic emissions from the bubble cloud were acquired passively with the array and processed offline to form passive cavitation images using the robust Capon beamformer[115]. Because of data transfer rate limitations, acoustic emissions were

acquired once every 10 histotripsy pulses (200 frames per location). All 200 frames were averaged pixel-wise to generate a cumulative image for each waypoint (21 waypoints per clot). To calculate the total emitted pressure within the clot, the cumulative passive cavitation image was co-registered with the B-mode image and summed spatially over the clot area:

$$P_{clot} = \sum_{i=1}^{21} \sum_{r}^{\forall\, r \in clot} P_i(r) \quad (1)$$

where $P_i(r)$ is the PCI emitted pressure at location r for a waypoint i.

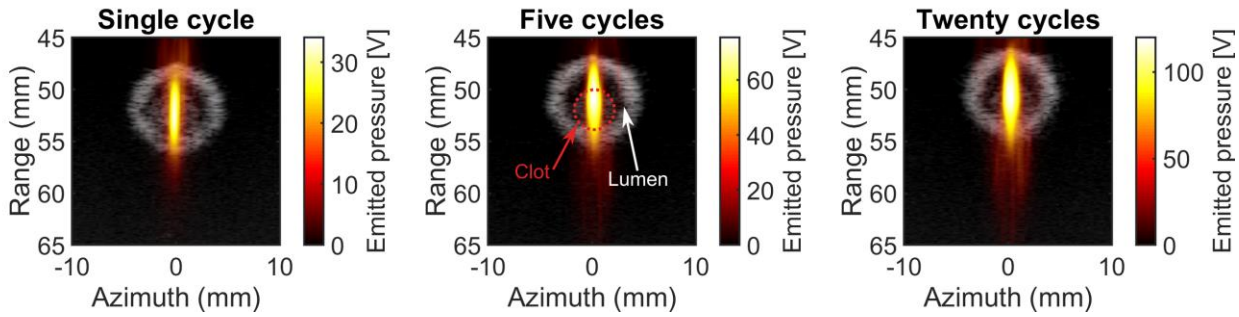

Figure 4.2: B-mode overlaid with passive cavitation data for single cycle, five cycle, and twenty cycle pulses (35 MPa peak negative pressure). In each image, the histotripsy pulse propagates from the top to the bottom. Although the focal length of the histotripsy transducer is 60 mm, the imaging array protrudes slightly beyond the opening of the transducer. This positioning of the imaging array explains why the focus appears before 60 mm relative to the imaging array.

4.2.6 Quantification of hemolysis and fibrinolysis

Within one minute of the end of treatment, the lumen was drained and the perfusate was transferred to microcentrifuge tubes for subsequent analysis. One end of the lumen was opened and tilted to allow for the extraction of the remaining clot segment via gravity. Clot mass loss was measured using a digital balance before and after treatment[23,24,161,168]. The concentration of hemoglobin and D-dimer in the perfusate were assayed to gauge hemolysis and fibrinolysis, respectively. Perfusate samples were stored at 4 degrees Celsius for no more than 4 hours between sample collection and subsequent analysis. Preliminary studies indicated samples were stable over this period, with no

significant change in the estimated hemoglobin or D-dimer. Drabkin's reagent assay (Sigma-Aldrich, St. Louis, MO, USA) was used to quantify hemoglobin, a marker of hemolysis[169]. A 1 mL sample of the perfusate was centrifuged at 610 RCF (3500 RPM) for 10 minutes, after which the supernatant and Drabkin's reagent were combined in a one-to-one ratio (0.5 mL each). The optical absorbance of the solution was measured at 540 nm using a plate reader (Synergy Neo HST, BioTek, Winooski, VT, USA), which was converted to hemoglobin concentration using a standard curve. An additional 1 mL sample of the perfusate was mixed with 0.1 mg/μL of 6-aminocaproic acid (Sigma-Aldrich, St. Louis, MO, USA) to halt fibrinolysis, and was subjected to a latex immuno-turbidimetric assay (STA R Max, Stago, Asnières sur seine, France) to quantify the D-dimer molecule concentration, a marker of fibrin degradation by rt-PA[11,48,151]. To examine structural changes, select clots were fixed in formalin, embedded in paraffin, sectioned, stained with Hematoxylin & Eosin, and digitally scanned.

4.2.7 Statistical analysis

Statistical analysis was performed using MATLAB 2017b (The Mathworks, Natick, MA, USA). A one-way analysis of variance (ANOVA) test was performed to determine differences in mass loss, hemoglobin concentration, or D-dimer concentration between arms ($\alpha = 0.05$)[170]. The Tukey honest significant difference test was employed to account for multiple comparisons[171]. Linear regression coefficients, reported as β values, were calculated to quantify the relationship between hemoglobin or D-dimer and mass loss. Linear regression coefficients were also calculated to determine the relationship between PCI pixel values and hemoglobin or D-dimer. Confidence intervals of the β-values ($\alpha = 0.05$) were calculated via the Wald method[172]. Similar analysis was performed to compare the effect of bubble activity on hemoglobin and D-dimer concentration.

Differences in D-dimer concentrations between lytic and non-lytic arms were analyzed using a two-tailed paired Student's t-test.

4.3 Results

4.3.1 Treatment efficacy

The clot mass loss was used as the overall metric of treatment efficacy and is reported in Figure 4.3. The relationship between clot mass loss and the peak negative pressure of single cycle pulses is indicated in Figure 4.3a, and the relationship between pulse duration and clot mass loss in Figure 4.3b. Trends indicating increases in clot mass loss were observed with increasing peak negative pressure, pulse duration, or lytic concentration. Overall, clots exposed to the combination of rt-PA and peak negative pressures of 30 MPa or greater resulted in significantly more mass loss than clots exposed to lytic alone (i.e., expected treatment efficacy with current standard of care).

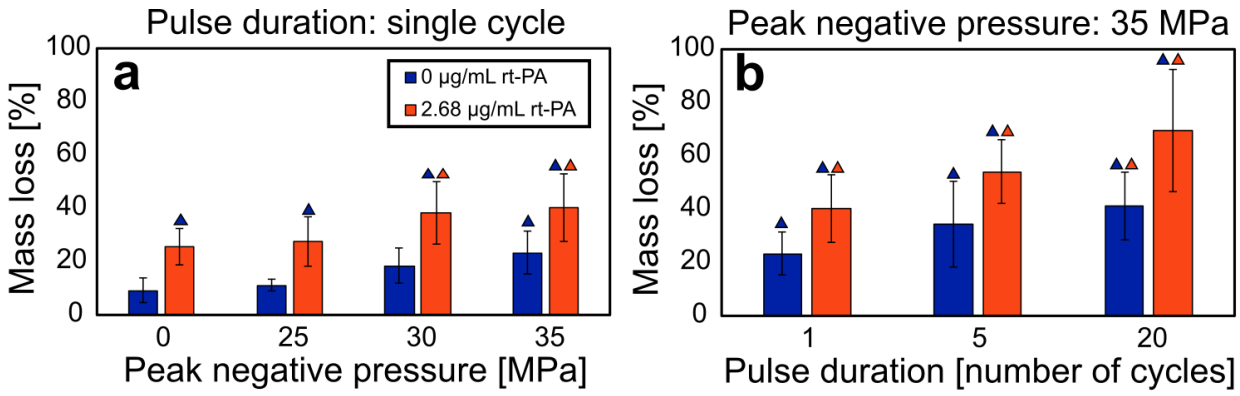

Figure 4.3: Clot mass loss for each experimental arm. Each experimental arm comprises at least eight samples. Error bars represent standard deviations. (a) Mass loss as a function of peak negative pressure for single-cycle pulses. (b) Mass loss as a function of pulse duration for 35 MPa peak negative pressure pulses. Orange (blue) triangles denote a significant difference from control arms at 0 MPa peak negative pressure with (without) lytic. Single-, five-, and twenty-cycle pulses correspond to 0.67 µs, 3.33 µs, and 13.3 µs pulse lengths, respectively.

4.3.2 Quantification of hemolysis and fibrinolysis

For each histotripsy insonation scheme, the resultant hemoglobin concentration was not statistically different for arms with and without lytic. These results indicate that rt-PA does not result in hemolysis and that free hemoglobin can be used a metric of the mechanical effects of histotripsy. The magnitude of clot fractionation increased with increasing peak negative pressure and pulse duration (Figure 4.4).

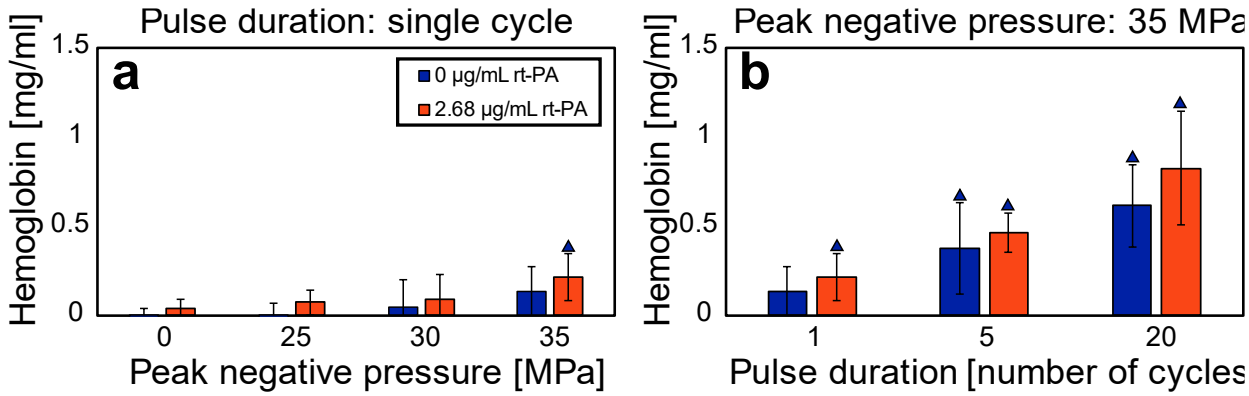

Figure 4.4: Hemoglobin concentration for each experimental arm indicating the degree of hemolysis. Each experimental arm comprises at least eight samples. Error bars represent standard deviations. (a) Hemoglobin as a function of peak negative pressure of the histotripsy pulse (single-cycle pulse duration only). (b) Hemoglobin as a function of the histotripsy pulse duration (35 MPa peak negative pressure only). Blue triangles denote a significant difference from control arms at 0 MPa peak negative pressure without lytic. For each insonation condition, the addition of rt-PA did not significantly change the amount of free hemoglobin. Single-, five-, and twenty-cycle pulses correspond to 0.67 µs, 3.33 µs, and 13.3 µs pulse duration, respectively.

To quantify the fibrinolytic component of clot degradation, D-dimer was measured. As shown in Figure 5, histotripsy in the absence of rt-PA generated D-dimer concentrations equivalent to clots exposed to plasma alone (no rt-PA and no histotripsy insonation). This data shows histotripsy insonation does not produce D-dimer directly from mechanical fractionation. Therefore, D-dimer can be used to quantify the contribution of rt-PA fibrinolysis to overall treatment efficacy. Increased fibrinolysis was observed for clots treated with rt-PA and

histotripsy compared to plasma alone (Figure 5). Increased D-Dimer compared to rt-PA alone (clinical standard) was observed for histotripsy arms with 35 MPa peak negative pressures pulses combined with lytic.

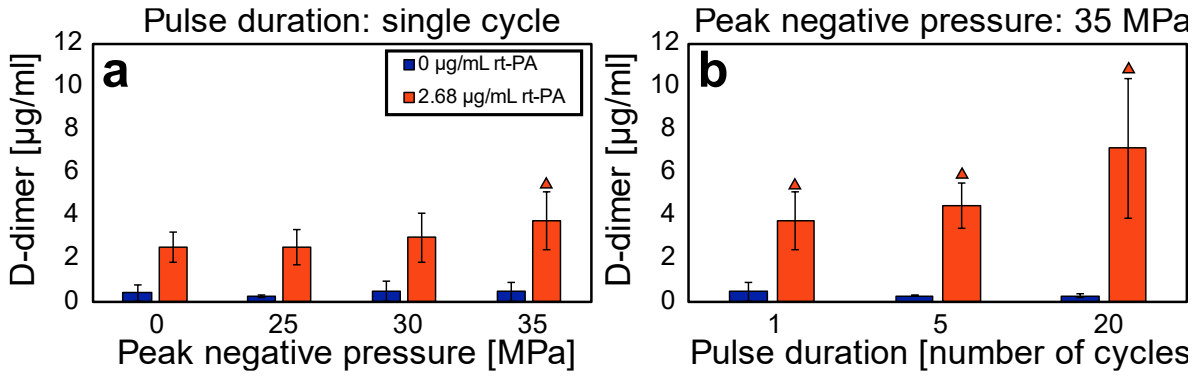

Figure 4.5: Figure 5: D-dimer concentration for each experimental arm. Each experimental arm comprises at least eight samples. Error bars represent standard deviations. (a) D-dimer as a function of peak negative pressure. (b) D-dimer as a function of cycles per pulse. Orange triangles denote a significant difference from control arms at 0 MPa peak negative pressure with lytic. For each histotripsy insonation condition, the addition of lytic significantly increase the D-dimer concentration in the perfusate compared to arms without rt-PA. Single cycle, five cycle, and twenty cycle pulses correspond to 0.67 µs, 3.33 µs, and 13.3 µs pulse durations, respectively.

Linear regression analysis was performed to assess the relationship between hemoglobin, D-dimer, and clot mass loss. Standard score (z-score) values were computed for hemoglobin and D-dimer concentrations in order to compare the change of each variable relative to the change in mass loss directly. As a result, these normalized values are unitless, and the slopes of the linear regression have units of percent mass loss [%]. The change was quantified by the slope $\beta_{M\text{-}X}$, where the subscript M refers to mass loss, and X refers to the paired variable for regression analysis (H for hemoglobin, D for D-dimer). In the absence of lytic, $\beta_{M\text{-}H}$ = 13.6% [11.4%, 15.8%] (Figure 4.6a), and $\beta_{M\text{-}D}$ = 3.6% [1.2%, 5.6%] (Figure 4.6c). Bracketed values denote the 95% confidence intervals of the slope, indicating a significant difference between $\beta_{M\text{-}H}$ and $\beta_{M\text{-}D}$ in the absence of

rt-PA. For clots exposed to lytic, $\beta_{M\text{-}H}$ = 9.5% [6.0%, 13.0%] (Figure 4.6b) and $\beta_{M\text{-}D}$ = 10.4% [6.9%, 13.8%] (Figure 4.6d). The slopes $\beta_{M\text{-}H}$ and $\beta_{M\text{-}D}$ calculated in the presence of lytic were not significantly different. Note that raw values for the concentration of hemoglobin and D-dimer are presented in Figure 4.6, not z-scores.

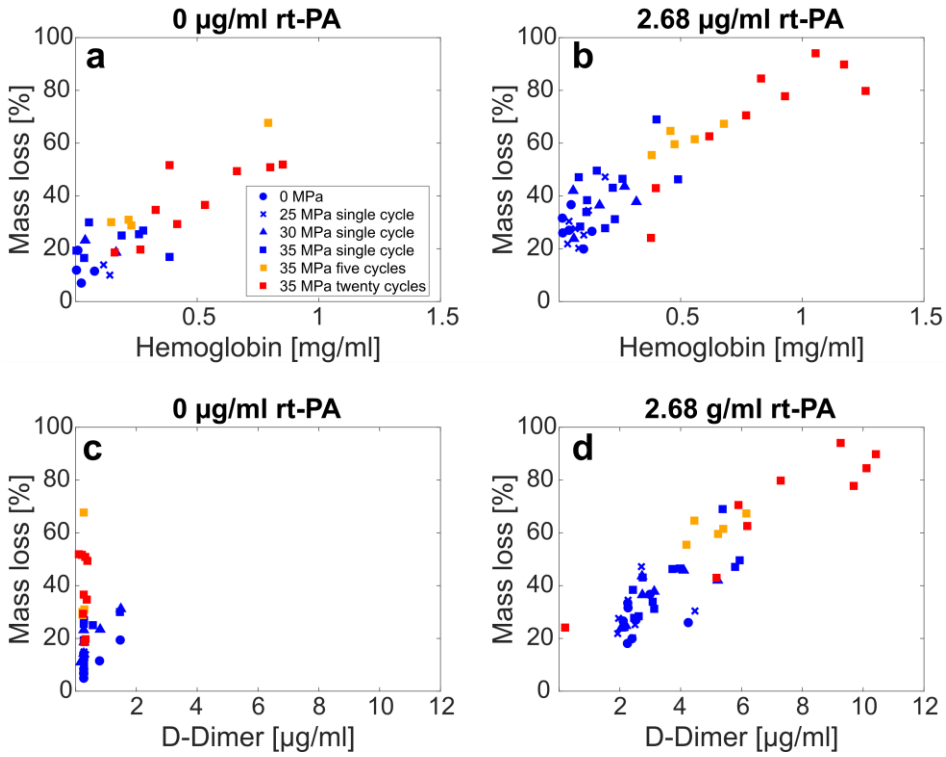

Figure 4.6: For all histotripsy insonation conditions, the relationship between (a) clot mass loss and hemoglobin without lytic, (b) clot mass loss and hemoglobin with lytic, (c) clot mass loss and D-dimer without lytic, and (d) clot mass loss and D-dimer with lytic. The legend in panel a indicating the histotripsy insonation parameters applies to all subfigures

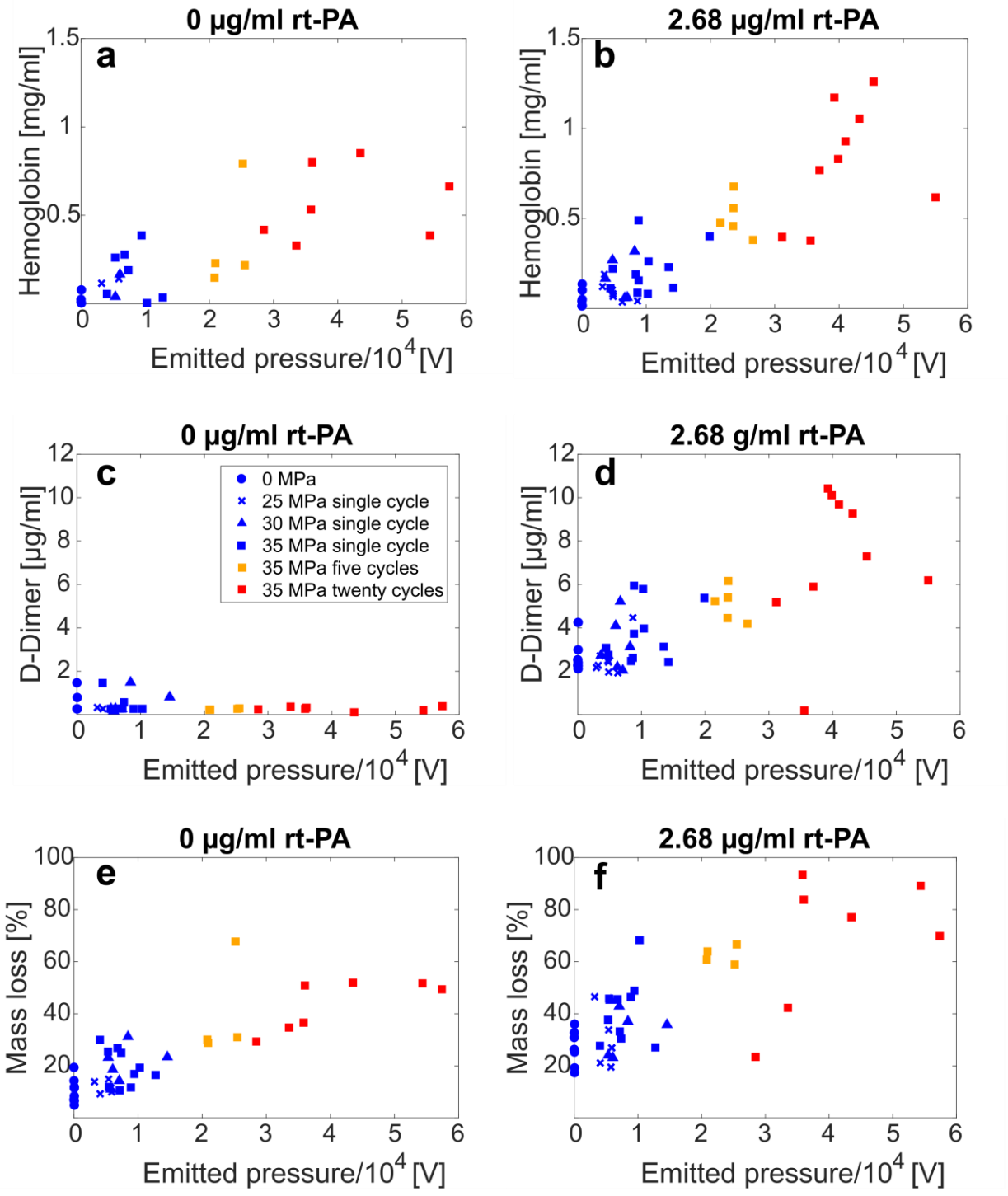

Figure 4.7: The relationship between acoustic emissions tracked with passive cavitation imaging and (a) hemoglobin for clots not exposed to lytic, (b) hemoglobin for clots exposed to lytic, (c) D-dimer for clots not exposed to lytic, (d) D-dimer for clots exposed to lytic, (e) mass loss for clots not exposed to lytic, and (f) mass loss for clots exposed to lytic. Histotripsy exposure conditions indicated in the panel c legend applies for all subfigures.

4.3.3 Bubble cloud emissions

A secondary aim of this study was to gauge the contribution of histotripsy bubble cloud activity to hemolysis and fibrinolysis. For each experiment, the tabulated acoustic emissions generated by the oscillations of the bubble cloud are compared to hemoglobin and D-dimer production in Figure 4.7. The acoustic emissions are the coherent summation of the pressure field originating from histotripsy bubble activity and incident on the imaging array[24,42,43,173]. These emissions induce voltages across each element of the imaging array in passive receive mode and are reported in volts. The reported voltage signal is proportional to the pressure incident on the imaging array and is the coherent summation of the bubble cloud acoustic emissions[174]. Linear regression analysis was used to compute the slopes of hemoglobin with acoustic emissions ($\beta_{H\text{-}A}$), and D-dimer with acoustic emissions ($\beta_{D\text{-}A}$). Standard score (z-score) values were computed for hemoglobin and D-dimer values prior to computing β. Acoustic emissions are reported in units of volts [V], and therefore, $\beta_{H\text{-}A}$ and $\beta_{D\text{-}A}$ have units of V^{-1}. For treatment arms without lytic, $\beta_{H\text{-}A}$ = 0.051 V^{-1} [0.039 V^{-1}, 0.064 V^{-1}] (Figure 4.7a) and $\beta_{D\text{-}A}$ = -0.013 V^{-1} [-0.034 V^{-1}, 0.008 V^{-1}] (Figure 4.7c). The 95% confidence interval of $\beta_{D\text{-}A}$ includes zero, indicating the majority of bubble cloud activity contributed to hemolysis in the absence of rt-PA. The slope between mass loss and acoustic emissions was also computed and found to be $\beta_{M\text{-}A}$ = 0.81 $\frac{\%}{V}$ [0.63 $\frac{\%}{V}$, 0.99 $\frac{\%}{V}$] (Figure 4.7e). For clots exposed to lytic, $\beta_{H\text{-}A}$ = 0.059 V^{-1} [0.049 V^{-1}, 0.069 V^{-1}] (Figure 4.7b), and $\beta_{D\text{-}A}$ = 0.050 V^{-1} [0.036 V^{-1}, 0.063 V^{-1}] (Figure 4.7d). The $\beta_{H\text{-}A}$ and $\beta_{D\text{-}A}$ values were statistically not different. For lytic arms, $\beta_{M\text{-}A}$ = 1.1 $\frac{\%}{V}$ [0.83 $\frac{\%}{V}$, 1.32 $\frac{\%}{V}$] (Figure 4.7f).

4.3.4 Histological analysis

To ascertain the qualitative effect of histotripsy and lytic on clot structure, samples were carefully removed from the flow channel, and sectioned and stained with Hematoxylin & Eosin. Damage to clot was primarily restricted to the center of the structure, as indicated by a reduction in red blood cells and fibrin mesh (Figure 4.8a). A sharp separation (less than 40 μm) was observed between intact and ablated portions of the clot. Smaller fibrin clusters were observed at the edge of the treatment zone for clots exposed to histotripsy and rt-PA compared to histotripsy alone (Figure 4.8). The reduced size and limited presence of the fibrin clusters was attributed to action of lytic. For the treatment arms with rt-PA, the extent of fibrin near the treatment zone decreased as the pulse duration increased, with no observable fibrin for the 20 cycle pulses. Though significant damage was observed within the center of the clot, fibrin structure along the perimeter of the damage zone appeared unaffected by the histotripsy insonation parameters for arms without lytic.

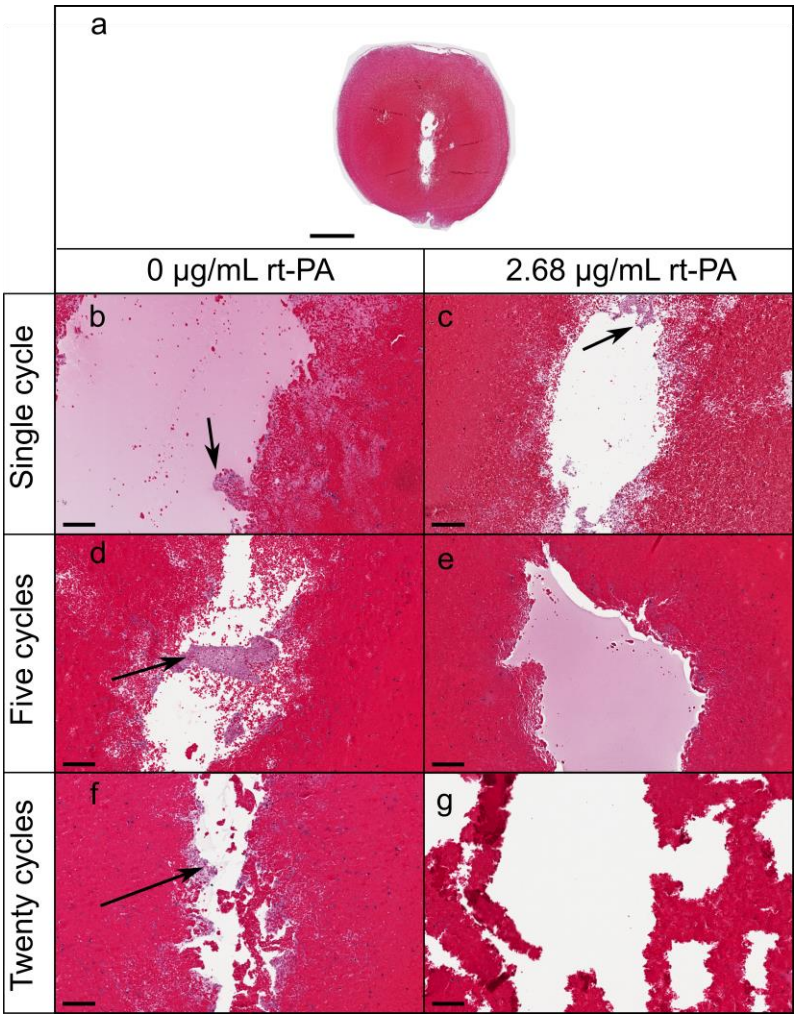

Figure 4.8: Representative histological sections of clots exposed to varying pulse durations (35 MPa) with and without lytic. In all cases, the histotripsy pulse propagated from the top to the bottom of the image. (a) Low-magnification image of a clot exposed to lytic and single cycle pulses (scale bar denotes 1 mm). Damage was contained almost entirely within the clot. (b-g) High-magnification images of clots post-treatment (scale bar denotes 100 µm). Black arrows point to residual fibrin clusters. Generally, clots exposed to histotripsy alone contained more fibrin within the treatment zone in comparison to clots exposed to histotripsy and lytic.

4.4 Discussion

4.4.1 Quantification of clot dissolution

Previous studies have demonstrated effective clot dissolution when combining histotripsy bubble cloud activity with a lytic therapy[23,24]. Here, the nature of clot degradation under this combination therapy, and how bubble cloud oscillations contribute to hemolysis and fibrinolysis, were investigated. Hemolysis was a contributing factor for all insonation schemes (Figure 4.6a,b), and was the primary contributor to mass loss in the absence of lytic (Figure 4.6a,c). Erythrocyte disruption would be expected based on the well-established correlation between histotripsy and tissue ablation at the cellular level[175]. Interestingly, $\beta_{M\text{-}H}$ (the slope comparing changes in hemoglobin to changes in mass loss) was not significantly different for arms with and without rt-PA, indicating the contribution of hemolysis to mass loss occurred independently of any concurrent fibrinolysis.

A strong increase was noted for the slope between D-dimer and mass loss, $\beta_{M\text{-}D}$, for arms with lytic compared to without lytic (Figure 4.6c,d). Further, almost no D-dimer was detected for arms without rt-PA. Histological analysis of the clots following histotripsy exposure demonstrated significant disruption of the fibrin network at the center of the ablation zone for all arms, including clots not exposed to lytic (Figure 4.8). These results indicate that though the fibrin network is damaged by histotripsy exposure, it is not reduced to D-dimer by histotripsy alone. In the presence of lytic, histotripsy may contribute to fibrinolysis as indicated by the production of D-dimer in several ways. Fluid mixing induced by bubble oscillations may increase rt-PA penetration into the clot[161]. Maxwell et al. have previously shown that cavitation can enhance streaming and generate vortices[153]. Bubble cloud-induced vortices in the perfusate may entrain lytic and plasminogen

within the clot, thereby increasing the likelihood of interaction with the fibrin mesh. Mechanical fractionation will erode and alter the clot shape, including the potential formation of channels within its structure (Figure 4.8). This damage will increase the surface area exposed to a lytic relative to the volume, promoting favorable lytic-to-clot interactions.

Clot mass loss may also occur through detachment of intact erythrocytes from the clot. Histotripsy and lytic both weaken the fibrin mesh, which can lead to the shedding of erythrocytes. Although intact erythrocytes were not analyzed in this study, numerous studies have demonstrated tissue debris following histotripsy exposure is primarily subcellular in size[23,24,159,176].

A further finding of note was the statistical equivalence between $\beta_{M\text{-}H}$ and $\beta_{M\text{-}D}$ for arms combining histotripsy and rt-PA. The equivalence of these slopes indicates that increasing hemoglobin by one standard deviation yielded the same mass loss as increasing D-dimer by one standard deviation. That is, hemolysis and fibrinolysis contribute equally to the overall thrombolytic efficacy in the presence of lytic, and are both critical for the success of this combination therapy. This finding may be specific to the clot model used in these studies, which is rich in both fibrin and erythrocytes. As a thrombus ages *in vivo*, the cellular structure is gradually replaced with more extensive extracellular components besides fibrin[7]. For such samples, fibrinolysis and hemolysis may have a reduced effect on treatment efficacy due to the thrombus composition. It should also be noted that 2000 histotripsy pulses were applied at each location in the clot, which likely resulted in overtreatment[136]. Therefore, the relative contribution of hemolysis and fibrinolysis to overall treatment efficacy may shift upon the development of future insonation schemes that avoid overtreatment. Regardless, hemolysis and fibrinolysis are both significant contributors to the efficacy of this approach.

4.4.2 Influence of insonation parameters on hemolysis and fibrinolysis

Over the range of insonation parameters explored here, the duration of the histotripsy pulse had a stronger influence on clot dissolution metrics (mass loss, hemoglobin, and D-dimer) compared to the peak negative pressure. This result may in part be due to the volume of the bubble cloud, and the relative proximity between bubbles and rt-PA. The influence of peak negative pressure was investigated for single-cycle histotripsy pulses, an approach known to produce very precise, small ablation zones within the clot[159]. Preliminary qualitative analysis of bubble cloud localization based on hyperechogenicity with B-mode imaging indicated confinement of the bubble cloud within the clot for single cycle pulses. The actual degree of hemoglobin generated may be underestimated for highly localized bubble clouds if these products are generated in the center of the clot, and unable to diffuse through viable portions of the clot into the perfusate. Lytic was infused in the plasma surrounding the clot, and was thus not in close proximity to bubble cloud activity contained within the center of the clot for single cycle pulses. In contrast, bubble clouds generated by multicycle pulses encompassed a larger portion of the lumen (Figure 4.2), resulting in robust degrees of hemolysis and fibrinolysis. These observations may indicate the need for bubble activity to be in close proximity to the lytic to promote fibrinolysis. The lytic infusion scheme used in this study mimics the administration of systemic rt-PA. In contrast, catheter directed thrombolytics are the preferred treatment method for iliofemoral venous thrombosis[16,177], which may promote strong fibrinolysis with single cycle histotripsy pulsing schemes.

4.4.3 Bubble cloud emissions

A secondary objective of this study was to assess the contribution of histotripsy-induced bubble cloud activity to hemolysis and fibrinolysis. Passive cavitation imaging was used to track the acoustic emissions, a surrogate for the degree of mechanical activity. Previous studies have

demonstrated a strong relationship between bubble activity tracked with passive cavitation imaging and hemolysis[40,178]. The data collected here indicate the change in hemolysis with bubble activity ($\beta_{H\text{-}A}$) was not different for arms with and without rt-PA. Hence, the presence of rt-PA did not influence erythrocyte degradation under the action of histotripsy bubble cloud activity.

Similar to the contributions to mass loss, the presence of rt-PA was necessary for bubble activity to promote fibrinolysis (i.e., $\beta_{D\text{-}A} > 0$). Prior studies established that acoustic emissions can be used to gauge overall thrombolytic efficacy[24], hemolysis[45], or histotripsy ablation[42,43,173]. Our data extend upon those previous findings to establish a direct connection between acoustic emissions and rt-PA activity to promote fibrinolysis. The contributions of bubble activity to hemolysis and fibrinolysis in the presence of rt-PA, reported by the slopes $\beta_{H\text{-}A}$ and $\beta_{D\text{-}A}$ respectively, were statistically equivalent. It should be noted that bubble activity depends nonlinearly on the type and concentration of bubble nuclei and medium[179], and on the insonation scheme[24]. Therefore, the findings here related to bubble contributions to overall treatment efficacy may not extend to other histotripsy-based treatment schemes.

4.4.4 Limitations

There are several aspects of this *in vitro* study that limit the generalizability of these findings. The primary metric of fibrinolytic activity in this study was D-dimer. The interaction between rt-PA and fibrin was assumed to occur in close proximity to the clot. It is possible that histotripsy bubble activity released fibrin strands from the clot that subsequently interacted with lytic. Degradation of released fibrin strands via rt-PA would result in an overestimate of the overall fibrinolytic contribution to clot mass loss. The contribution of histotripsy bubble activity in generating ejected fibrin strands will be the focus of future studies. A partially occlusive clot model was employed in

this study, whereas there would be limited lytic delivery for total vascular occlusion for the administration scheme employed in this study. The flow rate was fixed, and neglects the contribution of increased flow rate and shear stress as the clot lyses[180]. Retracted human whole blood clots were employed in this study, whereas several thrombus phenotypes have been identified in vascular occlusions[7,51]. Though clot mass loss was the primary metric of treatment efficacy in this study, recanalization (i.e. flow) is the primary clinical metric of treatment efficacy for venous thromboembolism[10,72]. Overall, these results indicate that histotripsy is a useful adjuvant therapy that enhances the current standard of care (lytic therapy) while providing the benefit of an effective ablative therapy.

4.5 Conclusions

For the acoustic parameters considered here, we have shown that clot degradation in the presence of rt-PA is caused by fibrinolysis and hemolysis. Additionally, we have shown that histotripsy bubble activity contributes equally to fibrinolysis and hemolysis. These results indicate that histotripsy is a promising adjuvant to thrombolytic therapy.

CHAPTER 5

THE INTERACTION OF CATHETER-DIRECTED THROMBOLYTICS AND HISTOTRIPSY IN VITRO

5.1 Introduction

Recombinant tissue-plasminogen activator is the most common thrombolytic in the United States for critical DVT thrombolysis[67,177]. Thrombolytics can be administered via a catheter, enabling higher local drug concentrations while lowering overall systemic dose[16]. Although rt-PA is effective at cleaving the fibrin mesh and extracellular framework within the thrombus, the incidence of severe hemorrhagic side effects nevertheless increases with lytic dose[15]. Chronic thrombi are less likely to respond to thrombolytic therapy and may require higher thrombolytic doses[7]. Another significant downside to catheter-directed thrombolysis is the long infusion time, which increases the likelihood of bleeding, as well as administrative and financial burdens. An adjuvant for CDT will enhance thrombolytic therapy while mitigating patient risk for critical and intractable DVT cases. Pharmacomechanical therapies that combine thrombolytics with mechanical fragmentation are a promising therapy for DVT[72].

Histotripsy used in combination with systemic lytic destroys red blood cells via mechanical ablation and enhances fibrinolytic activity[25]. Moreover, histotripsy is a vessel sparing technique[135] and may lessen the risk of undue bleeding as compared to using high doses of thrombolytic. The indwelling catheter used in CDT may affect the interaction between the bubble cloud and lytic in non-trivial ways compared to a systemic administration route. Such differences include altering the clot structure[25], harboring prompt nuclei that serve as a catalyst for cavitation, or breaking

down under the action of the histotripsy pulse. These effects should be studied to determine effective histotripsy strategies to enhance catheter-directed thrombolytic.

Here, clot degradation under the action of histotripsy and CDT was assessed. The change in clot mass was used as a metric of treatment efficacy. Hemoglobin acted as a marker for mechanical hemolysis, and D-dimer and fibrin degradation products were used to gauge fibrinolysis. Viable red blood cell concentration was measured in addition to hemoglobin because erythrocytes are a major cellular component of clots. Platelet concentration, a major factor in the clotting process[181], was assessed to gauge the risk of future thrombotic events. Additionally, passive cavitation data was collected during treatment to quantify the acoustic emissions generated by the bubble cloud.

5.2 Methods and materials

5.2.1 In vitro clot model

Clots were formed following an established Internal Review Board-approved protocol (University of Chicago IRB #19-1300). Whole blood was drawn from 9 volunteer patients at the University of Chicago Medicine cardiac catheterization laboratory. Immediately after collection, 4 mL aliquots of whole blood were transferred to borosilicate test tubes (#2378T43, McMaster-Carr, USA) and were incubated at 37 ℃ in a water bath for 3 hours. Clots were then moved to a 4 ℃ refrigerator for 3 days to allow for full retraction[161], and used within 2 weeks of formation.

5.2.2 Preparation of human plasma and recombinant tissue-type plasminogen activator

Human fresh-frozen plasma was obtained from a blood bank (Vitalant, Chicago, IL), thawed, divided into 35 mL aliquots, and stored at -80 ℃. Recombinant tissue-type plasminogen activator (1 mg/mL) was transferred to 0.5 mL aliquots and stored at -80 ℃. Lytic used in this manner is stable for at least 7 years[162].

5.2.3 Histotripsy insonation

Histotripsy pulses were generated by an eight-element, elliptically focused transducer (9 cm major axis, 7 cm minor axis) driven by a custom-designed class D amplifier and matching network[164,182]. The transducer was designed specifically for the treatment of iliofemoral DVT via histotripsy, and had a focal length of 6 cm with a -6-dB focal width of 4.27 mm x 0.66 mm x 0.70 mm (axial direction, major axis, and minor axis). A coaxial L11-5v array (Verasonics, Inc., Kirkland, WA, USA) inserted within a central opening in the histotripsy transducer was used to provide image guidance. A total of 2000 pulses were applied at a 40 Hz rate at each treatment location. Each pulse had a twenty cycle duration and peak negative pressures of 0 or 35 MPa. These parameters have been shown previously to nucleate strong bubble cloud and promote clot dissolution[25].

5.2.4 Experimental procedure

To model venous obstruction, clots were section to 1 cm length and introduced into a flow channel. The channel consisted of a syringe pump (EW-74900-20, Cole-Parmer, Vernon Hills, IL, USA) that drew plasma through 12.7-mm-inner-diameter and 1.6-mm wall thickness latex tubing (McMaster-Carr, Elmhurst, IL, USA) at a rate of 0.65 mL/min. This flow rate mimics the movement of blood in a partially occluded iliofemoral vein[165]. The flow channel was submerged

in a tank of degassed (< 20% dissolved oxygen), reverse osmosis water heated to 37.3℃ ± 0.5 ℃. A 5F Cragg-McNamara infusion catheter (Medtronics, Minneapolis, Minnesota, USA) was perfused with lytic and was used to cross the clot. Using this method, the catheter is used to penetrate the length of the clot (Figure 5.1).

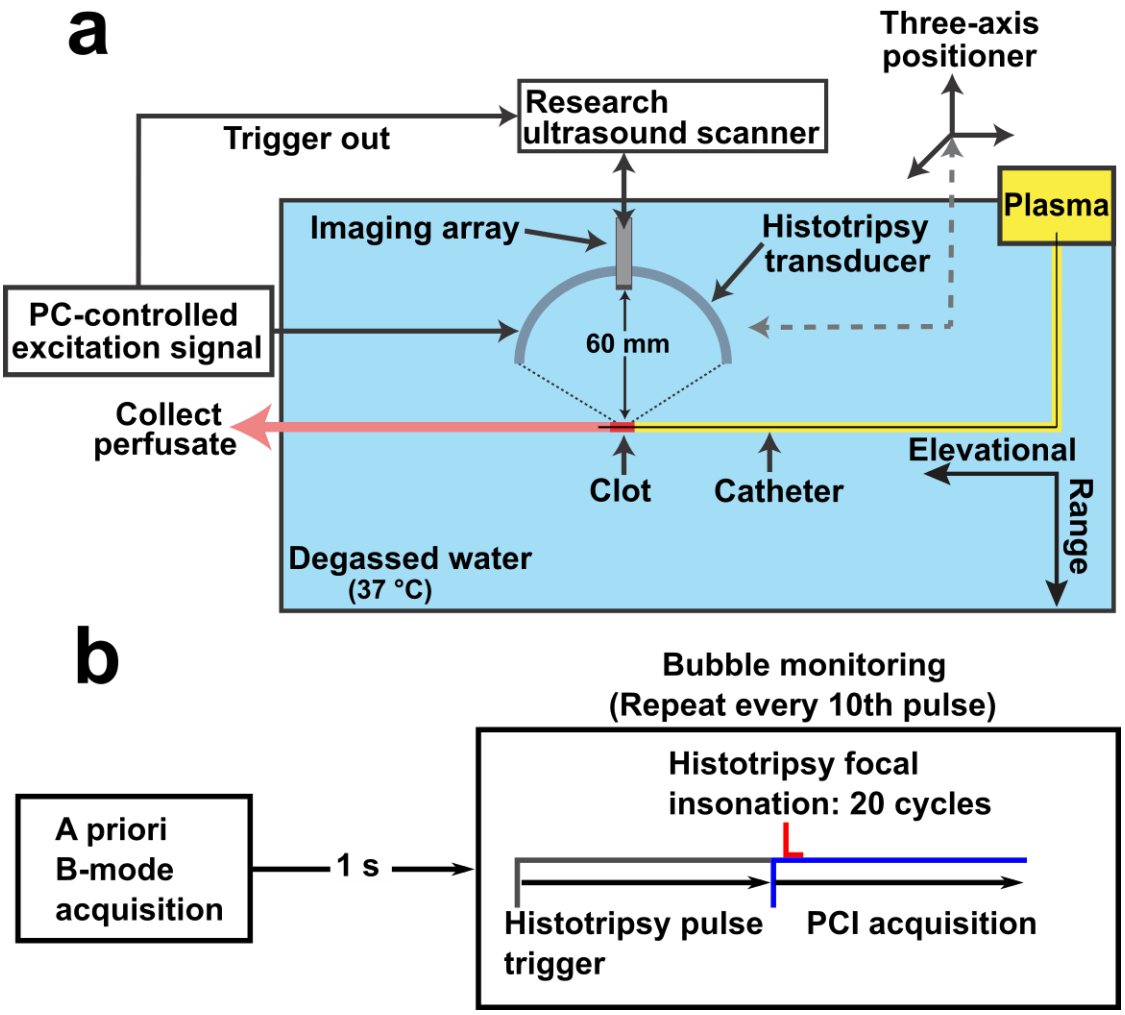

Figure 5.1: Experimental setup. (a) Overview of flow channel system. Fluid flow and the histotripsy source moves from right to left. The clot is punctured and lytic is delivered locally via catheter. (b) Timing diagram for histotripsy generation and image acquisition. Imaging and therapy pulses were interleaved to avoid interference.

During treatment, lytic was infused at a constant rate of 230 μL/min for approximately 21 minutes. The overall lytic concentrations were 0, 0.23, 2.25, or 4.54 μg/mL with corresponding infusion rates of 0, 0.02, 0.20, or 0.41 mg/h, respectively. The highest lytic dose is slightly less than that used CDT protocols, and the second-highest dosage corresponds to that seen in pharmacomechanical therapy[24,166].

Pre-treatment planning was performed as described previously[24,25]. Briefly, three orthogonal motorized linear stages (BiSlide, Velmex Inc., Bloomfield, NY, USA) were used to position the histotripsy source along the length of the clot. Short test insonations (< 20 pulses) were used to ensure the positioning of the histotripsy bubble cloud within the clot, and waypoints were placed in 5 mm increments along the length of the clot (3 in total). A path was interpolated from the waypoints to generate 21 treatment points with 0.5 mm spacing.

5.2.5 Perfusate assays

Clot disruption was investigated by assaying the perfusate to assess hemoglobin, D-dimer, general fibrin degradation products, red blood cells, and platelets. Hemoglobin and D-dimer concentrations were measured as described previously to assess hemolysis and fibrinolysis resulting from histotripsy exposure[25]. Briefly, hemoglobin was assessed via Drabkin's reagent assay (Sigma-Aldrich, St. Louis, MO, USA), and D-dimer was quantified using a latex immune-turbidimetric assay (STA R Max, Stago, Ansières sur seine, France). Fibrin degradation products (FDP) were measured using a semi-quantitative assay (Diagnostica Stago Inc., USA) to complement to D-dimer assays. FDP assays are more sensitive to fibrinolysis than D-dimer tests but have a lower resolution than true quantitative D-dimer assays. Due to the semi-quantitative nature of the assay, FDP concentrations were grouped into three bins: 0-10 μg/mL, 10-20 μg/mL, and 20-40 μg/mL. Aminocaproic acid (100 μg/mL) was added to the D-dimer and fibrin

degradation product aliquots directly after treatment in order to halt further thrombolytic activity. Viable red blood cells and platelets were measured using an automated five-part differential hematology analyzer (XN-350, Sysmex, Lincolnshire, IL, USA).

5.2.6 Imaging analysis

The location and strength of bubble cloud activity was recorded using passive cavitation imaging. Standard B-mode ultrasound images were acquired prior to histotripsy insonation at each treatment location. Acoustic emissions generated by the bubble cloud were passively recorded with the coaxial imaging array during the histotripsy insonation and processed offline using the Robust Capon Beamformer[24,25,183]. Each pixel value in the beamformed image corresponds to the acoustic pressure emitted by the bubble cloud at that location. (Figure 5.2). Due to data transfer rate limitations, acoustic emissions were recorded only once every ten histotripsy pulses (200 total frames per treatment location). Within each treatment location, the 200 individual frames were averaged pixel-wise to generate a cumulative image.

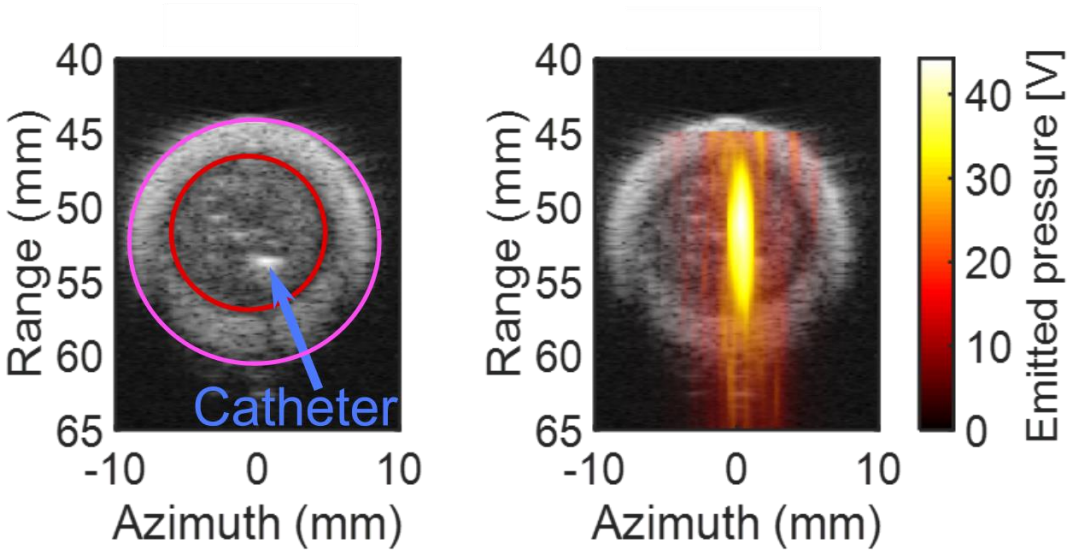

Figure 5.2: (Left) B-mode cross-sectional image of lumen, clot, and catheter. The lumen is outlined in pink, the clot is outlined in red, and the catheter is marked by the blue arrow. (Right) B-mode image with PCI overlay indicating acoustic emissions generated by the bubble cloud.

5.2.6 Statistical methods

Statistical analysis was performed using MATLAB 2017b (The Mathworks, Natick, MA, USA). Statistical differences within mass loss, hemoglobin concentration, D-dimer concentration, platelet count, and red blood cell count were tabulated using a Wilcoxon ranked-sum test[184] with Bonferroni correction for multiple comparison[185]. Clot components were compared to mass loss using multiple linear regression. The coefficients of the regression were reported as β values. The β-values are reported as confidence intervals. All statistical tests used a significance level of 0.05.

5.3 Results

5.3.1 Histotripsy increases treatment efficacy

Treatment efficacy was measured as a function of mass loss for clots exposed to a range of thrombolytic concentrations with and without histotripsy (Figure 5.3). Histotripsy significantly increased treatment efficacy ($p < 0.05$) for clots exposed to low and moderate levels of lytic (0.23 µg/mL and 2.25 µg/mL, respectively). Treatment efficacy for clots exposed to the combination of histotripsy and at least 0.23 µg/mL of lytic were non-inferior to the current standard of care dosage for catheter-directed thrombolytics (4.54 µg/mL). Histotripsy alone (0 µg/mL rt-PA) did not result in greater treatment efficacy compared to control.

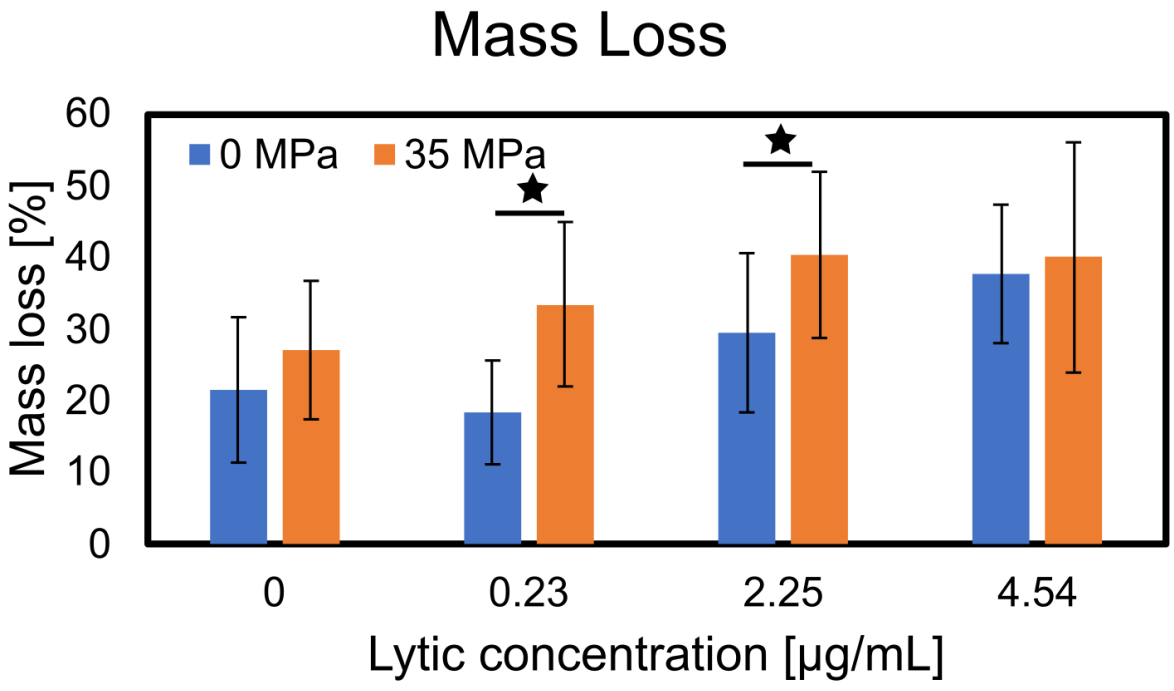

Figure 5.3: Clot mass loss as a function of lytic concentration and histotripsy exposure. Stars indicate statistically significant increases in mass loss ($p < 0.05$). Blue bars indicate clots not exposed to histotripsy, and orange bars indicate clots exposed to histotripsy.

5.3.2 Assessment of cellular components following histotripsy exposure

Hemoglobin, red blood cell, and platelet content in the perfusate following exposure to histotripsy and lytic are reported in Figure 5.4. Paired one-tailed ranked-sum tests revealed that histotripsy increased the amount of hemoglobin ($p < 0.05$) when clots were not exposed to any lytic (0 µg/mL). For clots exposed to lytic, histotripsy did not result in increased hemoglobin within any lytic group. The concentration of red blood cells was highly variable and was not significantly different for any treatment arm. Histotripsy resulted in slightly higher platelet concentrations, but this difference was not statistically significant ($p > 0.05$).

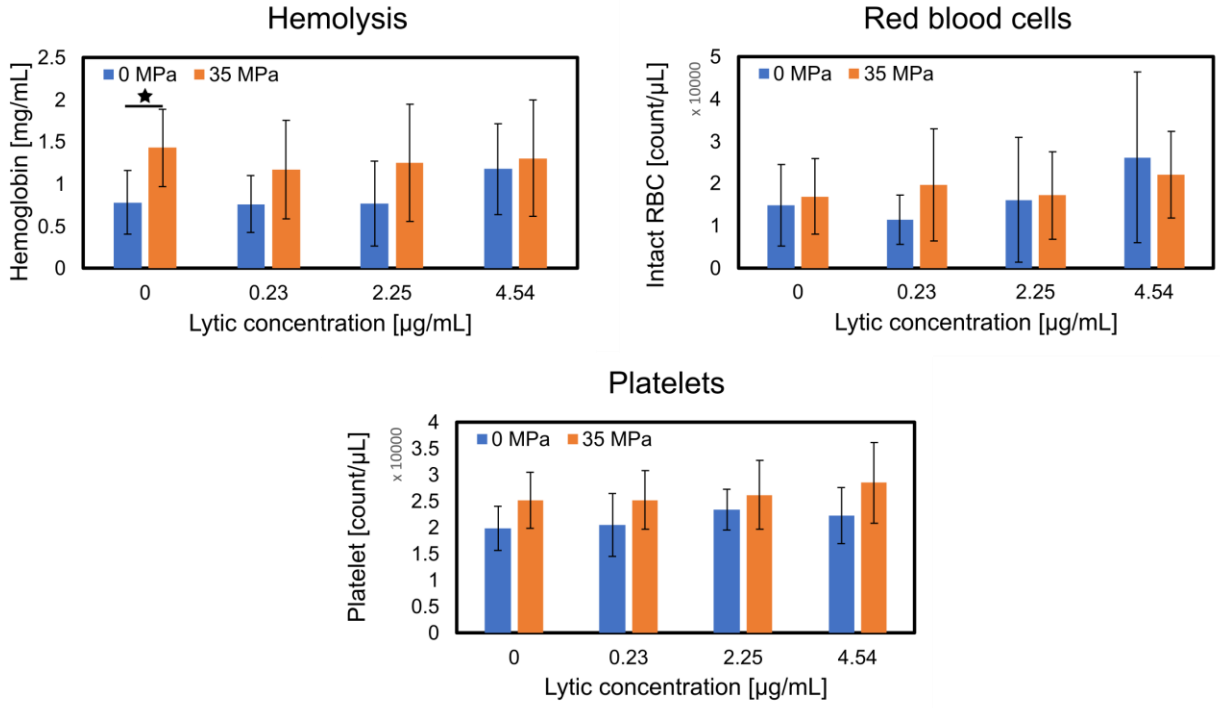

Figure 5.4: Hemolysis, red blood cell count, and platelet count as a function of lytic dose and histotripsy exposure. Stars indicate a statistically significant difference ($p < 0.05$). Blue bars indicate clots not exposed to histotripsy, and orange bars indicate clots exposed to histotripsy

5.3.3 D-dimer and fibrin degradation products

The concentration of D-dimer following exposure to all treatment arms is reported in Figure 5.5. Lytic doses 0.23 μg/mL and greater combined with histotripsy resulted in non-inferior D-dimer levels when compared to clots exposed to 4.54 μg/mL alone (CDT standard of care). For clots exposed to 2.25 μg/mL of rt-PA, histotripsy significantly increased the amount of D-dimer measured. For clots exposed to histotripsy, D-dimer was correlated with lytic dose ($R = 0.73$, $p < 0.05$)

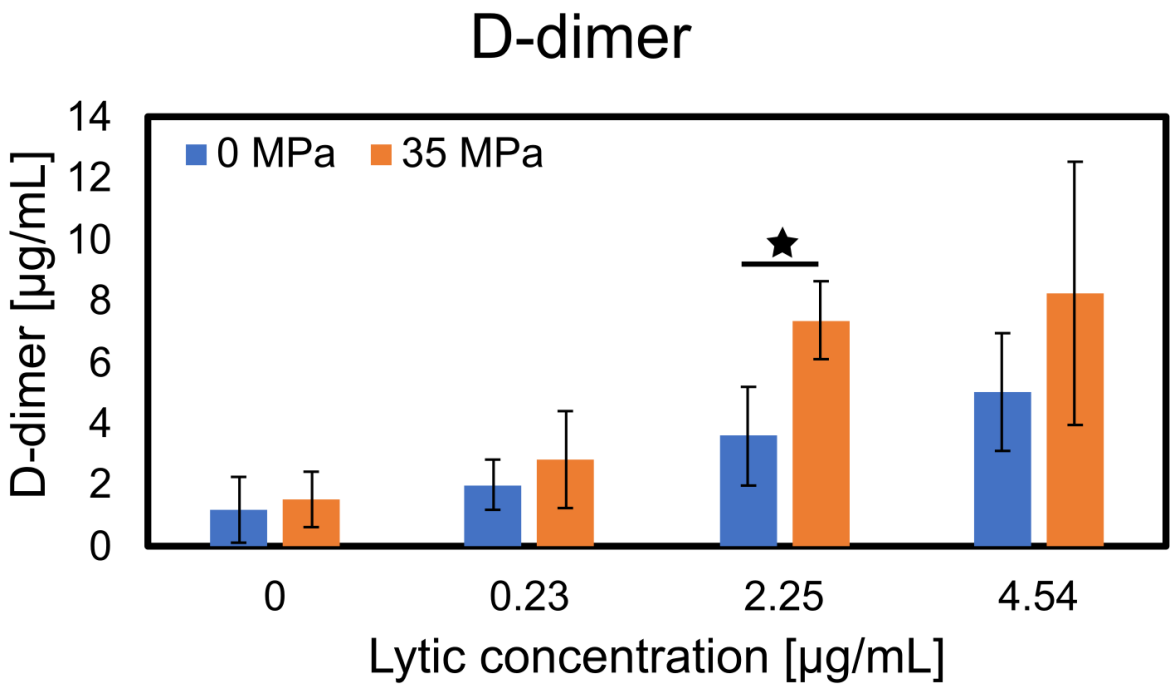

Figure 5.5: D-dimer as a function of lytic concentration and histotripsy exposure. Stars indicate statistically significant increases in mass loss ($p < 0.05$). Blue bars indicate clots not exposed to histotripsy, and orange bars indicate clots exposed to histotripsy

Fibrin degradation products were assayed to gauge general fibrinolysis with a high degree of sensitivity. Histotripsy appears to affect the distribution of FDP levels for the two highest dosages (Figure 5.6). The histograms of the two highest lytic-only arms are skewed right in comparison to the corresponding histotripsy histograms. These two histotripsy arms were more likely to contain high concentrations of FDP as compared to the lytic-only arms.

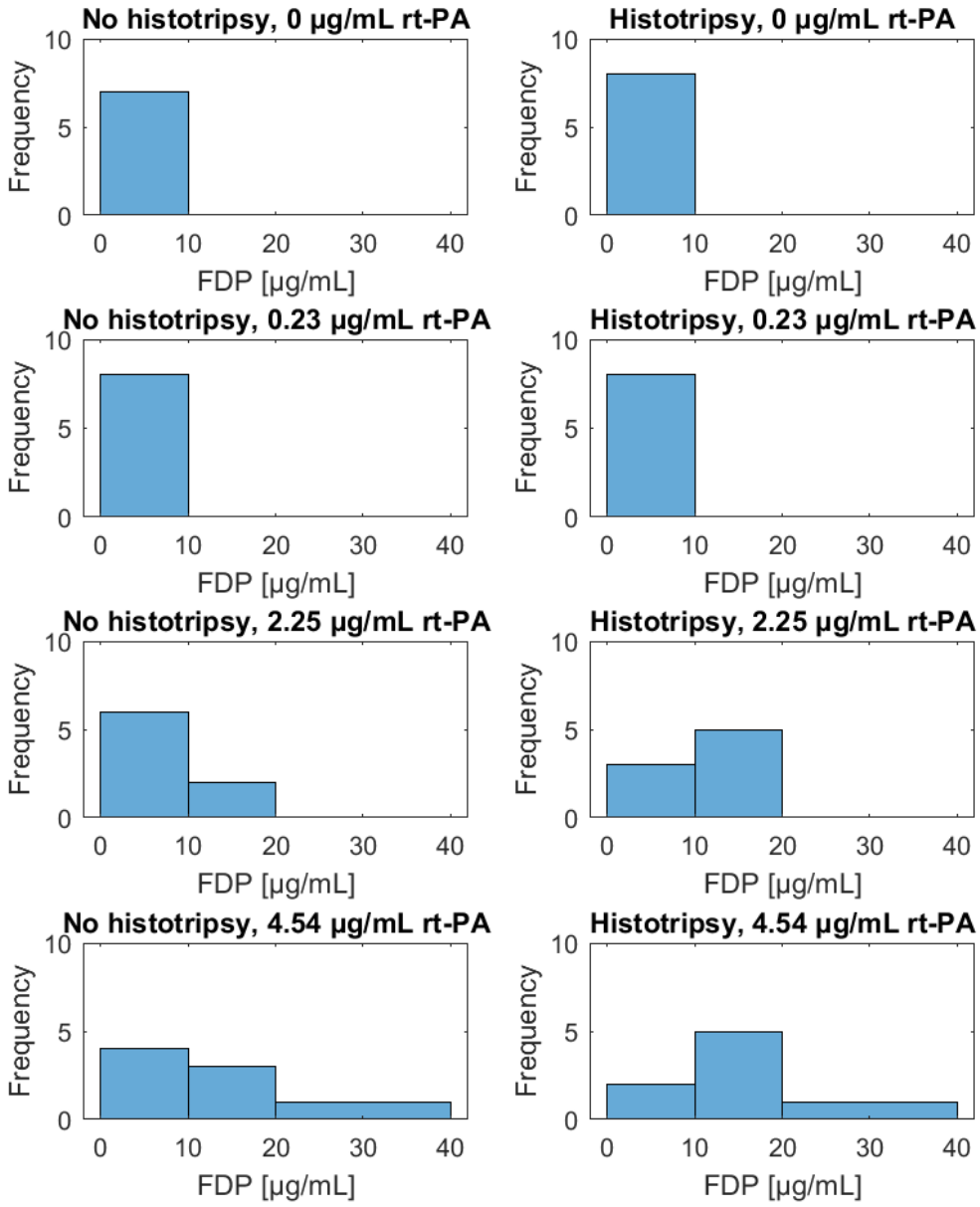

Figure 5.6: Histograms of fibrin degradation products for all eight experimental arms. The left column of subfigures corresponds to lytic-only arms, and the right column of subfigures corresponds to histotripsy and lytic. Each row of subfigures corresponds to a single concentration of lytic. Bins were created according to the semi-quantitative nature of the FDP assay.

5.3.4 Linear regression between debris components and mass loss

Multiple linear regression analysis was used to compare the normalized relationship between hemoglobin concentration, red blood cell count, platelet count, D-dimer concentration, and mass loss, as described previously[25]. As a result of the normalization process, the slopes of the linear regression have units of percent mass loss (%) and are presented as 95% confidence intervals (Table 5.1). Clots exposed to lytic alone (no histotripsy) exhibited a significant relationship between hemoglobin, D-dimer, and mass loss. Clots exposed to histotripsy and lytic showed a connection between hemoglobin, D-dimer, red blood cell content, and mass loss. Compared to lytic alone, histotripsy enhanced the relationship between mass loss, D-dimer, and red blood cells. The slopes of the linear regression were not significantly different when comparing mass loss and clot components (i.e. comparing mass loss vs. hemoglobin, mass loss vs. red blood cells, mass loss vs. D-dimer, and mass loss vs. platelets).

Table 5.1: Influence of clot component on mass loss for clots exposed to histotripsy and lytic or lytic alone. The slopes of the linear regression between mass loss and clot components were computed. These slopes are reported as 95% confidence intervals. As a result of the normalization process these values have units of percent mass loss (%). The middle column represents regression slopes for clots exposed to lytic alone, and the right column represents slopes for clots exposed to lytic and histotripsy.

	Effect of clot component on mass loss [%]	
Clot component	**No histotripsy**	**Histotripsy**
Hemoglobin	(3.1, 11.0)	(3.3, 9.0)
D-dimer	(1.2, 6.7)	(4.0, 8.0)
Red blood cell	(-0.7, 6.0)	(1.8, 6.5)
Platelet	(-3.9, 1.9)	(-4.0, 1.4)

5.3.5 Location and strength of bubble cloud activity

Acoustic emissions were acquired and beamformed via the Robust Capon beamformer to gauge the strength of the histotripsy bubble cloud. The location of maximum acoustic emissions at each treatment site was collected and compared to the location of the catheter. The average Euclidean distance between acoustic emissions maxima and catheter location was 3.05 ± 2.69 mm. On average the maximum acoustic emissions were detected 1.16 ± 3.29 mm below the catheter. The acoustic maxima were located within the clot for 99.2% of all treatment locations. The average pressure emitted by the bubble cloud and received by the imaging array was 19 ± 5 kV.

5.4 Discussion

5.4.1 Histotripsy and treatment efficacy

Previous work has shown that combining histotripsy with a systemic lytic administration scheme is effective at destroying clot tissue[24,25]. However, these studies only utilized a fixed lytic dose and did not investigate the effect of catheter-directed thrombolytics. An adjuvant therapy that reduces the lytic dose will reduce patient risk. In our study we have shown that histotripsy reduces the amount of catheter-delivered lytic necessary to achieve thrombolysis. Combining histotripsy with $1/20^{th}$ the standard dose for CDT was as effective as using the standard CDT treatment scheme alone. Besides reducing patient risk, lowering the dose of lytic would decrease the treatment time and would significantly lessen the cost per treatment. By using $1/20^{th}$ of the lytic dose and assuming a 2 hour treatment time, this treatment would reduce the treatment cost by $3700 (nearly an 80% reduction in cost)[166]. It should be noted that restoration of flow is the clinical endpoint, but

our study used mass loss and D-dimer as measurement of treatment efficacy and fibrinolysis, respectively. D-dimer is correlated with vessel patency during thrombolysis[186], so there is evidence to suggest that our results are generalizable to the clinic.

There was no observed increase in mass loss with or without histotripsy for clots not exposed to lytic. This finding is in contradiction to a previous similar study[25]. Furthermore, the average acoustic pressure detected by the imaging array was 40% smaller for our study despite using the same insonation parameters. Clot size may affect acoustic emissions and histotripsy efficacy. Our study used a clot size of 10 mm in diameter to accommodate the diameter of the catheter and to replicate the size of lower-extremity venous occlusions[187,188]. This is more than double the diameter of the clots used in the previous study, and an increase in size results in more attenuation. Attenuation affects shock wave formation[140], and could affect the shock scattering histotripsy mechanism used here. Likewise, histotripsy did not significantly affect clot mass loss for the highest (4.54 μg/mL) lytic dose. Cavitation is associated with drug delivery, and a reduction in bubble activity will negatively affect drug delivery. Higher peak negative pressures can be used to overcome the effect of attenuation and to generate stronger bubble activity[32].

5.4.2 Histotripsy and mechanisms of clot disintegration

The mechanisms of clot disintegration were examined by using linear regression to compare clot debris to mass loss. When histotripsy is combined with lytic, clot mass loss was linked to D-dimer, hemoglobin, and viable red blood cell counts (Table 5.1). Although hemolysis was associated with increases in mass loss, histotripsy did not increase hemoglobin production compared to lytic alone. Furthermore, hemoglobin was associated with mass loss even when clots were not exposed to histotripsy. This finding contrasts with a previous study which found that histotripsy does result in

significant hemolysis[25]. The placement of the catheter could potentially affect the amount of measured hemoglobin. In our study, the clot is punctured with the catheter and results in mechanical damage to the clot prior to treatment. Variations in catheter position will then result in different amounts of hemoglobin, and this variability may hide the effect of histotripsy on hemolysis. The choice of histotripsy parameters may also affect the perfusate concentration. Increasing the peak negative pressure might increase the mechanical activity of the bubble cloud[24,25] and may lead to greater hemolysis[25].

Histotripsy enhances thrombolysis by improving the efficacy of the lytic and not by mechanically cleaving the fibrin mesh. Fibrin is individual composed of monomers that are polymerized. Fibrin is cleaved at discrete locations during thrombolysis and divides into chains of fibrin degradation products with varying lengths. Typical sizes of soluble products range from 260 kDa (D-dimer) to at least 2300 kDa[189]. Histotripsy increases D-dimer and FDP levels in the presence of lytic. However, histotripsy does not affect the concentration of D-dimer or FDP if no lytic is present. Thus, the bubble cloud most likely destroys the fibrin mesh by enhancing lytic effectiveness.

5.4.3 Limitations

There are limitations to this study that limit the generalizability of these findings. The flow rate of plasma around the clot was held constant, whereas clot dissolution would normally change the flow rate and shear stress around the clot[180]. Using a catheter damages the clot before treatment and may affect measurements of mass loss and perfusate debris. The fibrin degradation assay used here was semi-quantitative, which may be insensitive to small changes in the breakdown of fibrin due to the treatment schemes tested here. The clots used in this study were homogenous[190], and do

not match the heterogeneity observed clinically[7]. This may result in differences in treatment response.

5.5 Conclusions

We have shown that histotripsy can reduce the dose of lytic by almost a factor of 20 in comparison to standard catheter-directed thrombolysis treatment. This treatment enhancement was shown by increases in mass loss and fibrinolysis. Although histotripsy does not remove the fibrin mesh on its own, it significantly enhances thrombolytic activity for the lytic doses examined in this study. Furthermore, catheter placement does not impede our ability to position the histotripsy bubble cloud. These results indicate that histotripsy is an effective adjuvant therapy for catheter-directed thrombolysis.

CHAPTER 6

CONCLUSIONS

6.1 Acute and chronic clots

The goal of this research is to combine histotripsy with thrombolytics to improve upon current DVT treatment schemes while reducing patient risk. Catheter-directed thrombolytics are the frontline therapy for vessel recanalization in critical cases, but some thrombi do not respond readily to this potentially hazardous treatment. Studying the composition of these thrombi will help reveal when CDT might be effective and how the structure might affect histotripsy bubble activity. In this dissertation, the composition of ex vivo thrombi were examined. Chronic thrombi (> 7 days old) tended to have more collagen and fewer red blood cells than acute thrombi. Unlike the studies in chapters 4 and 5, hemoglobin might not be a good metric for monitoring chronic clot ablation because of the lack of erythrocyte content. The well-retracted clot model used in chapters 4 and 5 were similar in structure to the acute VTE samples and were primarily composed of erythrocytes and fibrin. The results in the *in vitro* studies may be a good indicator for how acute thrombi respond to treatment. Nevertheless, these results may not be applicable for the treatment of chronic deep vein thrombosis. Future work is needed to design an *in vitro* clot model that mimics chronic thrombi. Further *in vivo* work would also help replicate the complex clotting and fibrinolytic cascades.

6.2 Image guided therapy for deep vein thrombosis

Improvements in image guidance should improve treatment efficacy and clinical outcomes. As shown in chapter 2, thrombi exhibit significant heterogeneity. Histotripsy could be a complementary therapy to CDT and target the lytic-resistant chronic portions. Using histotripsy to

target sections that are not susceptible to lytics will reduce the overall treatment time for the combination approach. However, it is difficult to know *a priori* which, if any, portions of the thrombus are susceptible to lytic. To overcome this gap in knowledge, we have shown that QSM may be able to predict thrombolytic susceptibility.

Overall, QSM, B-mode imaging, and PCI are powerful tools that will help guide treatment for deep vein thrombosis. Quantitative susceptibility mapping is able to predict thrombolytic susceptibility. B-mode imaging provides a fast way to localize target tissue and histotripsy bubble activity. Passive cavitation imaging (PCI) can be used to quantify histotripsy bubble activity, gauge treatment progress, and ensure sufficient mechanical activity. Despite significant variation in thrombus stiffness (53 kPa – 122 kPa) a single PCI threshold might be sufficient for detecting ablation if the stiffness is below 142 kPa, as shown in chapter 3. This imaging technique could also be used to gauge lytic enhancement in real time because PCI correlates with fibrinolysis, as measured by D-dimer. Combining these imaging modalities, however, may be difficult. Catheter labs typically include fluoroscopy and ultrasound systems, but not MR scanners. One option is to use QSM to scan the patient for chronic clot portions. Then, an image fusion algorithm could be used to overlay the QSM data with the fluoroscopic images in the catheter lab. However, this is challenging and is not fully automated as of yet[191]. An alternative would be to include an MR scanner in a radiographic cardiac catheter laboratory. There are MR catheter labs in specialist centers in the United States and Europe, but this technology is not yet widespread[192]. An advantage of using an MR catheter lab is that histotripsy devices can be made out of MR-compatible materials[193]. These imaging techniques are also non-ionizing, and would reduce the radiation dose to the patient.

6.3 Effect of focal volume on treatment

Iliofemoral thrombi can exceed 9 cm in length[194] and 1.5 cm in diameter[188]. The volumes of these thrombi are much larger than the focal volume of the histotripsy transducer used in these studies. This may lead to undertreatment for certain treatment conditions. Chapter 4 showed that multicycle pulses resulted in greater mass loss than single cycle pulses. Prior studies have demonstrated multicycle pulses produce larger bubble clouds[32,163], which may explain the increase in efficacy. If the clot is larger than the focal volume, then histotripsy will be less successful for the schemes tested in these studies. Histotripsy treatment volume should not be smaller than the clot volume. The histotripsy treatment volume can be increased by mechanically translating the source throughout more locations. A recent study has shown that a robotic arm is able to guide histotripsy treatments beyond the natural focus of the transducer with submillimeter accuracy[167]. Another option is to electronically steer the focus to expose multiple locations simultaneously[160]. Alternatively, the size of the bubble cloud can be increased by designing alternative sources. Such modifications might include increasing the f-number[195], changing the number and position of elements, or changing the shape of the transducer[196].

6.4 Histotripsy as an adjuvant therapy

Previous studies have shown that therapeutic ultrasound can be used to destroy clot tissue[23,24,168]. However these studies only examined treatment efficacy via mass loss. For the first time, we have used biomarkers to quantify how histotripsy energy facilitates clot degradation. This information yields deeper insights into the mechanisms of thrombus destruction. As shown in chapter 4, histotripsy breaks down clots by mechanically rupturing the red blood cells and by enhancing lytic activity. This result suggests that histotripsy will be effective for acute thrombi. Although the effect of histotripsy has not been tested on chronic thrombi, *in vivo* porcine studies have shown that

histotripsy bubble activity can damage a variety of tissues including heart, muscle, liver, and kidney[135]. Histotripsy will likely be able to damage stiff, chronic thrombi also. Histotripsy can enhance lytic activity in the acute thrombi and can mechanically destroy the lytic-resistant chronic thrombi. Moreover, we have shown that histotripsy can reduce the amount of lytic by a factor of 20 compared to the standard CDT treatment scheme. These results indicate that histotripsy is a promising adjuvant therapy for deep vein thrombosis.

6.5 Future work

There are several research avenues that will help enhance our understanding of histotripsy thrombolysis and facilitate its transition to the clinic. The clot model used in these studies utilizes the electrostatic charge on borosilicate glass pipettes to activate platelets within whole blood to produce a well-retracted clot[190]. As opposed to chronic thrombi, these clots have a higher proportion of red blood cells and do not contain detectible amounts of collagen. The next leap forward in thrombosis research is the development of a replicable *in vitro* chronic clot model. This will enable a high degree of experimental control that other *in vivo* models may not be able to provide. Plasminogen activator inhibitor-1 is a primary component of thrombolytic resistance and is secreted by platelets, among other cells[197,198]. Doping clots with additional platelets may encourage the release of more PAI-1, with the added benefit of increasing the degree of fibrin retraction[199]. Collagen deposition can be initialized by adding cardiac fibroblasts[87], which would add an additional extracellular structure. Transforming growth factor β-1 has also been shown to increase fibroblast growth[200], which will help stimulate collagen production. Furthermore, collagen production can be enhanced indirectly by stimulating TGF-β-1 by the addition of MCP-1[201].

In vivo animal studies are a prerequisite for clinical trials. Previous work has explored the use of histotripsy without lytic in a porcine model of DVT[26,37]. However, the combination of lytic and histotripsy has not been examined *in vivo*. The metric of success will be recanalization as determined by post-treatment blood flow and clinical scores such as the vascular clinical severity score (VCSS)[202]. Because of biological differences between pigs and humans, standard D-dimer measurements cannot be used as metrics of thrombolysis. Furthermore, pigs are less susceptible to thrombolysis because porcine blood contains less plasminogen than human blood[203]. Post-treatment necropsy would help determine the effect of histotripsy on the endothelium and if there are significant off-target effects. Based on the results of chapters 4 and 5, multi-cycle pulses at 35 MPa peak negative pressure should be used. Collaborative robotics would enable the translation of the histotripsy source along the volume of the thrombus. This would allow for submillimeter accuracy for a variety of anatomies[167].

Moore's law states that the number of transistors per integrated circuit doubles approximately every two years. The rise of cheap yet powerful computing resources has helped usher in the age of machine learning. Machine learning is especially useful in performing medical imaging tasks[204] and could help improve histotripsy treatment planning. In chapters 4 and 5, the treatment path was established by sending test pulses at the distal, middle, and proximal portions of the clot. If cavitation was not fully contained within the target, then the histotripsy source was moved. This process would repeat until the cavitation was contained fully within the target volume. This process is even more difficult *in vivo*, and the boundaries between tissue inhomogeneities could reflect histotripsy pulses to cause off-target cavitation. One could train a neural network on dataset consisting of B-mode images and the location of maximum bubble activity. This algorithm would then be able to predict the region of maximum bubble activity without firing any test pulses.

This would expedite the pre-treatment process and reduce the amount of time spent trying to place the focus within the target. Furthermore, it would avoid off-target cavitation and mitigate the possibility of overtreatment.

This dissertation explored using histotripsy as an adjuvant therapy for deep vein thrombosis. The results of these studies offer insight into the mechanisms of histotripsy-enhanced thrombolysis and the optimal parameters for successful treatment. Further investigation based on the results of these studies will help facilitate the introduction of histotripsy to the clinic to help treat intractable DVT.

REFERENCES

1. Waheed SM, Kudaravalli P, Hotwagner DT. Deep Vein Thrombosis (DVT). In: *StatPearls*. StatPearls Publishing; 2020. Accessed April 2, 2020. http://www.ncbi.nlm.nih.gov/books/NBK507708/
2. Office of the Surgeon General (US), National Heart, Lung, and Blood Institute (US). *The Surgeon General's Call to Action to Prevent Deep Vein Thrombosis and Pulmonary Embolism*. Office of the Surgeon General (US); 2008. Accessed April 2, 2020. http://www.ncbi.nlm.nih.gov/books/NBK44178/
3. Spencer FA, Emery C, Lessard D, et al. The Worcester Venous Thromboembolism study: a population-based study of the clinical epidemiology of venous thromboembolism. *J Gen Intern Med*. 2006;21(7):722-727. doi:10.1111/j.1525-1497.2006.00458.x
4. Fleck D, Albadawi H, Shamoun F, Knuttinen G, Naidu S, Oklu R. Catheter-directed thrombolysis of deep vein thrombosis: literature review and practice considerations. *Cardiovasc Diagn Ther*. 2017;7(Suppl 3):S228-S237. doi:10.21037/cdt.2017.09.15
5. Beckman MG, Hooper WC, Critchley SE, Ortel TL. Venous Thromboembolism: A Public Health Concern. *American Journal of Preventive Medicine*. 2010;38(4):S495-S501. doi:10.1016/j.amepre.2009.12.017
6. Stone J, Hangge P, Albadawi H, et al. Deep vein thrombosis: pathogenesis, diagnosis, and medical management. *Cardiovasc Diagn Ther*. 2017;7(Suppl 3):S276-S284. doi:10.21037/cdt.2017.09.01
7. Czaplicki C, Albadawi H, Partovi S, et al. Can thrombus age guide thrombolytic therapy? *Cardiovasc Diagn Ther*. 2017;7(Suppl 3):S186-S196. doi:10.21037/cdt.2017.11.05
8. Thaler J, Pabinger I, Ay C. Anticoagulant Treatment of Deep Vein Thrombosis and Pulmonary Embolism: The Present State of the Art. *Front Cardiovasc Med*. 2015;2:30. doi:10.3389/fcvm.2015.00030
9. Streiff MB, Agnelli G, Connors JM, et al. Guidance for the treatment of deep vein thrombosis and pulmonary embolism. *J Thromb Thrombolysis*. 2016;41:32-67. doi:10.1007/s11239-015-1317-0
10. Jaff MR, McMurtry MS, Archer SL, et al. Management of massive and submassive pulmonary embolism, iliofemoral deep vein thrombosis, and chronic thromboembolic pulmonary hypertension: a scientific statement from the American Heart Association. *Circulation*. 2011;123(16):1788-1830. doi:10.1161/CIR.0b013e318214914f
11. Jilani TN, Siddiqui AH. Tissue Plasminogen Activator. In: *StatPearls*. StatPearls Publishing; 2020. Accessed April 13, 2020. http://www.ncbi.nlm.nih.gov/books/NBK507917/
12. Gong M, He X, Song J, et al. Catheter-Directed Thrombolysis With a Continuous Infusion of Low-Dose Alteplase for Subacute Proximal Venous Thrombosis: Efficacy and Safety Compared to Urokinase. *Clin Appl Thromb Hemost*. 2018;24(8):1333-1339. doi:10.1177/1076029618775514
13. Brandt K, McGinn K, Quedado J. Low-Dose Systemic Alteplase (tPA) for the Treatment of Pulmonary Embolism: *Annals of Pharmacotherapy*. Published online April 9, 2015. doi:10.1177/1060028015579988

14. Roth JM. Recombinant tissue plasminogen activator for the treatment of acute ischemic stroke. *Proc (Bayl Univ Med Cent)*. 2011;24(3):257-259.
15. Mewissen MW, Seabrook GR, Meissner MH, Cynamon J, Labropoulos N, Haughton SH. Catheter-directed thrombolysis for lower extremity deep venous thrombosis: report of a national multicenter registry. *Radiology*. 1999;211(1):39-49. doi:10.1148/radiology.211.1.r99ap4739
16. Chen JX, Sudheendra D, Stavropoulos SW, Nadolski GJ. Role of Catheter-directed Thrombolysis in Management of Iliofemoral Deep Venous Thrombosis. *Radiographics*. 2016;36(5):1565-1575. doi:10.1148/rg.2016150138
17. Hirsh J, Hoak J. Management of deep vein thrombosis and pulmonary embolism. A statement for healthcare professionals. Council on Thrombosis (in consultation with the Council on Cardiovascular Radiology), American Heart Association. *Circulation*. 1996;93(12):2212-2245. doi:10.1161/01.cir.93.12.2212
18. Cornman-Homonoff J, Kishore S, Camacho JC, Winokur RS. Intravascular Ultrasound-Guided Extraction of Free-Floating Inferior Vena Cava Tumor Thrombus Using the ClotTriever Mechanical Thrombectomy Device. *Journal of Vascular and Interventional Radiology*. 2019;30(10):1679-1682.e1. doi:10.1016/j.jvir.2019.04.035
19. Weinberg AS, Dohad S, Ramzy D, Madyoon H, Tapson VF. Clot Extraction With the FlowTriever Device in Acute Massive Pulmonary Embolism. *J Intensive Care Med*. 2016;31(10):676-679. doi:10.1177/0885066616666031
20. Benarroch-Gampel J, Pujari A, Aizpuru M, Rajani RR, Jordan WD, Crawford R. Technical success and short-term outcomes after treatment of lower extremity deep vein thrombosis with the ClotTriever system: A preliminary experience. *Journal of Vascular Surgery: Venous and Lymphatic Disorders*. 2020;8(2):174-181. doi:10.1016/j.jvsv.2019.10.024
21. Vlaisavljevich E, Kim Y, Allen S, et al. Image-guided non-invasive ultrasound liver ablation using histotripsy: feasibility study in an in vivo porcine model. *Ultrasound Med Biol*. 2013;39(8):1398-1409. doi:10.1016/j.ultrasmedbio.2013.02.005
22. Knott EA, Swietlik JF, Longo KC, et al. Robotically-Assisted Sonic Therapy for Renal Ablation in a Live Porcine Model: Initial Preclinical Results. *J Vasc Interv Radiol*. 2019;30(8):1293-1302. doi:10.1016/j.jvir.2019.01.023
23. Bader KB, Haworth KJ, Shekhar H, et al. Efficacy of histotripsy combined with rt-PA in vitro. *Phys Med Biol*. 2016;61(14):5253-5274. doi:10.1088/0031-9155/61/14/5253
24. Bollen V, Hendley SA, Paul JD, et al. In Vitro Thrombolytic Efficacy of Single- and Five-Cycle Histotripsy Pulses and rt-PA. *Ultrasound in Medicine & Biology*. 2020;46(2):336-349. doi:10.1016/j.ultrasmedbio.2019.10.009
25. Hendley SA, Paul JD, Maxwell AD, Haworth KJ, Holland CK, Bader KB. Clot degradation under the action of histotripsy bubble activity and a lytic drug. *IEEE Trans Ultrason Ferroelectr Freq Control*. 2021;PP. doi:10.1109/TUFFC.2021.3052393
26. Zhang X, Macoskey JJ, Ives K, et al. Noninvasive Thrombolysis using Microtripsy in a Porcine Deep Vein Thrombosis Model. *Ultrasound Med Biol*. 2017;43(7):1378-1390. doi:10.1016/j.ultrasmedbio.2017.01.028
27. Sukovich JR, Cain CA, Pandey AS, et al. In vivo histotripsy brain treatment. *Journal of Neurosurgery*. 2018;131(4):1331-1338. doi:10.3171/2018.4.JNS172652
28. Mild hyperthermia by MR-guided focused ultrasound in an ex vivo model of osteolytic bone tumour: optimization of the spatio-temporal control of the delivered temperature | Journal of

Translational Medicine | Full Text. Accessed March 28, 2021. https://translational-medicine.biomedcentral.com/articles/10.1186/s12967-019-2094-x
29. Zhou Y-F. High intensity focused ultrasound in clinical tumor ablation. *World J Clin Oncol*. 2011;2(1):8-27. doi:10.5306/wjco.v2.i1.8
30. Haar GT, Coussios C. High intensity focused ultrasound: physical principles and devices. *Int J Hyperthermia*. 2007;23(2):89-104. doi:10.1080/02656730601186138
31. Lake AM, Hall TL, Kieran K, Fowlkes JB, Cain CA, Roberts WW. Histotripsy: A Minimally Invasive Technology for Prostate Tissue Ablation in an In-vivo Canine Model. *Urology*. 2008;72(3):682-686. doi:10.1016/j.urology.2008.01.037
32. Maxwell AD, Wang T-Y, Cain CA, et al. Cavitation clouds created by shock scattering from bubbles during histotripsy. *J Acoust Soc Am*. 2011;130(4):1888-1898. doi:10.1121/1.3625239
33. Riesz P, Kondo T. Free radical formation induced by ultrasound and its biological implications. *Free Radic Biol Med*. 1992;13(3):247-270. doi:10.1016/0891-5849(92)90021-8
34. Weiss HL, Selvaraj P, Okita K, et al. Mechanical clot damage from cavitation during sonothrombolysis. *J Acoust Soc Am*. 2013;133(5):3159-3175. doi:10.1121/1.4795774
35. Collis J, Manasseh R, Liovic P, et al. Cavitation microstreaming and stress fields created by microbubbles. *Ultrasonics*. 2010;50(2):273-279. doi:10.1016/j.ultras.2009.10.002
36. Elder SA. Cavitation Microstreaming. *The Journal of the Acoustical Society of America*. 1959;31(1):54-64. doi:10.1121/1.1907611
37. Noninvasive Treatment of Deep Venous Thrombosis Using Pulsed Ultrasound Cavitation Therapy (Histotripsy) in a Porcine Model. *Journal of Vascular and Interventional Radiology*. 2011;22(3):369-377. doi:10.1016/j.jvir.2010.10.007
38. Bader KB, Vlaisavljevich E, Maxwell AD. For whom the bubble grows: Physical principles of bubble nucleation and dynamics in histotripsy ultrasound therapy. *Ultrasound Med Biol*. 2019;45(5):1056-1080. doi:10.1016/j.ultrasmedbio.2018.10.035
39. Gateau J, Aubry J-F, Pernot M, Fink M, Tanter M. Combined passive detection and ultrafast active imaging of cavitation events induced by short pulses of high-intensity ultrasound. *IEEE Trans Ultrason Ferroelectr Freq Control*. 2011;58(3):517-532. doi:10.1109/TUFFC.2011.1836
40. Smith CAB, Coussios CC. Spatiotemporal Assessment of the Cellular Safety of Cavitation-Based Therapies by Passive Acoustic Mapping. *Ultrasound in Medicine & Biology*. 2020;46(5):1235-1243. doi:10.1016/j.ultrasmedbio.2020.01.009
41. Hall TL, Fowlkes JB, Cain CA. A real-time measure of cavitation induced tissue disruption by ultrasound imaging backscatter reduction. *IEEE Transactions on Ultrasonics, Ferroelectrics, and Frequency Control*. 2007;54(3):569-575. doi:10.1109/TUFFC.2007.279
42. Bader KB, Haworth KJ, Maxwell AD, Holland CK. Post Hoc Analysis of Passive Cavitation Imaging for Classification of Histotripsy-Induced Liquefaction in Vitro. *IEEE Trans Med Imaging*. 2018;37(1):106-115. doi:10.1109/TMI.2017.2735238
43. Anthony GJ, Bollen V, Hendley S, Antic T, Sammet S, Bader KB. Assessment of histotripsy-induced liquefaction with diagnostic ultrasound and magnetic resonance imaging in vitro and ex vivo. *Phys Med Biol*. 2019;64(9):095023. doi:10.1088/1361-6560/ab143f
44. Bader KB, Bouchoux G, Holland CK. Sonothrombolysis. *Adv Exp Med Biol*. 2016;880:339-362. doi:10.1007/978-3-319-22536-4_19

45. Chen W-S, Brayman AA, Matula TJ, Crum LA, Miller MW. The pulse length-dependence of inertial cavitation dose and hemolysis. *Ultrasound in Medicine & Biology*. 2003;29(5):739-748. doi:10.1016/S0301-5629(03)00029-2
46. Datta S, Coussios C-C, Ammi AY, Mast TD, de Courten-Myers GM, Holland CK. Ultrasound-Enhanced Thrombolysis Using Definity® as a Cavitation Nucleation Agent. *Ultrasound in Medicine & Biology*. 2008;34(9):1421-1433. doi:10.1016/j.ultrasmedbio.2008.01.016
47. Sutton JT, Haworth KJ, Pyne-Geithman G, Holland CK. Ultrasound-mediated drug delivery for cardiovascular disease. *Expert Opin Drug Deliv*. 2013;10(5):573-592. doi:10.1517/17425247.2013.772578
48. Adam SS, Key NS, Greenberg CS. D-dimer antigen: current concepts and future prospects. *Blood*. 2009;113(13):2878-2887. doi:10.1182/blood-2008-06-165845
49. Amin VB, Lookstein RA. Catheter-directed interventions for acute iliocaval deep vein thrombosis. *Tech Vasc Interv Radiol*. 2014;17(2):96-102. doi:10.1053/j.tvir.2014.02.006
50. Gagne P, Khoury T, Zadeh BJ, Rajasinghe HA. A Multicenter, Retrospective Study of the Effectiveness of the Trellis-8 System in the Treatment of Proximal Lower-Extremity Deep Vein Thrombosis. *Ann Vasc Surg*. 2015;29(8):1633-1641. doi:10.1016/j.avsg.2015.05.029
51. Barros D'Sa AAB, Chant ADB. *Emergency Vascular and Endovascular Surgical Practice*. Hodder Arnold ; Distributed in the U.S.A. by Oxford University Press; 2005. Accessed April 13, 2020. http://site.ebrary.com/id/10397204
52. Wells PS, Forgie MA, Rodger MA. Treatment of venous thromboembolism. *JAMA*. 2014;311(7):717-728. doi:10.1001/jama.2014.65
53. Mozaffarian Dariush, Benjamin Emelia J., Go Alan S., et al. Executive Summary: Heart Disease and Stroke Statistics—2016 Update. *Circulation*. 2016;133(4):447-454. doi:10.1161/CIR.0000000000000366
54. Go Alan S., Mozaffarian Dariush, Roger Véronique L., et al. Heart Disease and Stroke Statistics—2013 Update. *Circulation*. 2013;127(1):e6-e245. doi:10.1161/CIR.0b013e31828124ad
55. Lin SC, Mousa A, Bernheim J, et al. Endoluminal recanalization in a patient with phlegmasia cerulea dolens using a multimodality approach-a case report. *Vasc Endovascular Surg*. 2005;39(3):273-279. doi:10.1177/153857440503900309
56. Oğuzkurt L, Ozkan U, Gülcan O, Koca N, Gür S. Endovascular treatment of acute and subacute iliofemoral deep venous thrombosis by using manual aspiration thrombectomy: long-term results of 139 patients in a single center. *Diagn Interv Radiol*. 2012;18(4):410-416. doi:10.4261/1305-3825.DIR.5175-11.1
57. Patel NH, Plorde JJ, Meissner M. Catheter-directed thrombolysis in the treatment of phlegmasia cerulea dolens. *Ann Vasc Surg*. 1998;12(5):471-475. doi:10.1007/s100169900187
58. Hood DB, Weaver FA, Modrall JG, Yellin AE. Advances in the treatment of phlegmasia cerulea dolens. *Am J Surg*. 1993;166(2):206-210. doi:10.1016/s0002-9610(05)81057-8
59. Benjamin Emelia J., Virani Salim S., Callaway Clifton W., et al. Heart Disease and Stroke Statistics—2018 Update: A Report From the American Heart Association. *Circulation*. 2018;137(12):e67-e492. doi:10.1161/CIR.0000000000000558
60. Grosse SD. Incidence-based cost estimates require population-based incidence data. A critique of Mahan et al. *Thromb Haemost*. 2012;107(1):192-193; author reply 194-195. doi:10.1160/TH11-09-0666

61. Benjamin Emelia J., Blaha Michael J., Chiuve Stephanie E., et al. Heart Disease and Stroke Statistics—2017 Update: A Report From the American Heart Association. *Circulation*. 2017;135(10):e146-e603. doi:10.1161/CIR.0000000000000485
62. Horne III MK. Thrombolytic Therapy for Deep Venous Thrombosis? *JAMA*. 1999;282(22):2164. doi:10.1001/jama.282.22.2164
63. Enden T, Haig Y, Kløw N-E, et al. Long-term outcome after additional catheter-directed thrombolysis versus standard treatment for acute iliofemoral deep vein thrombosis (the CaVenT study): a randomised controlled trial. *Lancet*. 2012;379(9810):31-38. doi:10.1016/S0140-6736(11)61753-4
64. Grunwald MR, Hofmann LV. Comparison of Urokinase, Alteplase, and Reteplase for Catheter-directed Thrombolysis of Deep Venous Thrombosis. *Journal of Vascular and Interventional Radiology*. 2004;15(4):347-352. doi:10.1097/01.RVI.0000121407.46920.15
65. Shortell CK, Queiroz R, Johansson M, et al. Safety and efficacy of limited-dose tissue plasminogen activator in acute vascular occlusion. *J Vasc Surg*. 2001;34(5):854-859. doi:10.1067/mva.2001.118589
66. Sugimoto K, Hofmann LV, Razavi MK, et al. The safety, efficacy, and pharmacoeconomics of low-dose alteplase compared with urokinase for catheter-directed thrombolysis of arterial and venous occlusions. *J Vasc Surg*. 2003;37(3):512-517. doi:10.1067/mva.2003.41
67. Vedantham S, Piazza G, Sista AK, Goldenberg NA. Guidance for the use of thrombolytic therapy for the treatment of venous thromboembolism. *J Thromb Thrombolysis*. 2016;41:68-80. doi:10.1007/s11239-015-1318-z
68. Chiasakul T, Cuker A. The case for catheter-directed thrombolysis in selected patients with acute proximal deep vein thrombosis. *Blood Advances*. 2018;2(14):1799-1802. doi:10.1182/bloodadvances.2018018622
69. Ngo TH, Declerck PJ. Immunological quantitation of rabbit plasminogen activator inhibitor-1 in biological samples: evidence that rabbit platelets do not contain PAI-1. *Thromb Haemost*. 1999;82(5):1510-1515.
70. Flight SM, Masci PP, Lavin MF, Gaffney PJ. Resistance of porcine blood clots to lysis relates to poor activation of porcine plasminogen by tissue plasminogen activator. *Blood Coagul Fibrinolysis*. 2006;17(5):417-420. doi:10.1097/01.mbc.0000233374.79593.57
71. Siller-Matula JM, Plasenzotti R, Spiel A, Quehenberger P, Jilma B. Interspecies differences in coagulation profile. *Thromb Haemost*. 2008;100(3):397-404.
72. Vedantham S, Goldhaber SZ, Julian JA, et al. Pharmacomechanical Catheter-Directed Thrombolysis for Deep-Vein Thrombosis. *New England Journal of Medicine*. 2017;377(23):2240-2252. doi:10.1056/NEJMoa1615066
73. Hoang P, Wallace A, Sugi M, et al. Elastography techniques in the evaluation of deep vein thrombosis. *Cardiovasc Diagn Ther*. 2017;7(Suppl 3):S238-S245. doi:10.21037/cdt.2017.10.04
74. Beythien C, Terres W, Gutensohn K, Meinertz T. [Thrombus age as a determinant of lysis efficacy of in vitro produced platelet-fibrin thrombi]. *Z Kardiol*. 1996;85(9):661-667.
75. Jang I K, Gold H K, Ziskind A A, et al. Differential sensitivity of erythrocyte-rich and platelet-rich arterial thrombi to lysis with recombinant tissue-type plasminogen activator. A possible explanation for resistance to coronary thrombolysis. *Circulation*. 1989;79(4):920-928. doi:10.1161/01.CIR.79.4.920

76. Castaigne P, Lhermitte F, Gautier JC, Escourolle R, Derouesné C. Internal carotid artery occlusion. A study of 61 instances in 50 patients with post-mortem data. *Brain*. 1970;93(2):231-258. doi:10.1093/brain/93.2.231
77. Chang S, Zhang J, Liu T, et al. Quantitative Susceptibility Mapping of Intracerebral Hemorrhages at Various Stages. *J Magn Reson Imaging*. 2016;44(2):420-425. doi:10.1002/jmri.25143
78. Shaw GJ, Dhamija A, Bavani N, Wagner KR, Holland CK. Arrhenius temperature dependence of in vitro tissue plasminogen activator thrombolysis. *Phys Med Biol*. 2007;52(11):2953-2967. doi:10.1088/0031-9155/52/11/002
79. Bucciolini M, Ciraolo L, Lehmann B. Simulation of Biologic Tissues by Using Agar Gels at Magnetic Resonance Imaging. *Acta Radiol*. 1989;30(6):667-669. doi:10.3109/02841858909174735
80. Nonlinear regularization for per voxel estimation of magnetic susceptibility distributions from MRI field maps - PubMed. Accessed March 15, 2021. https://pubmed.ncbi.nlm.nih.gov/19502123/
81. Deng Y, Rouze NC, Palmeri ML, Nightingale KR. Ultrasonic Shear Wave Elasticity Imaging (SWEI) Sequencing and Data Processing Using a Verasonics Research Scanner. *Ultrasonics, Ferroelectrics and Frequency Control, IEEE Transactions on*. Published online January 2017:1.
82. Mercado-Shekhar KP, Kleven RT, Aponte Rivera H, et al. Effect of Clot Stiffness on Recombinant Tissue Plasminogen Activator Lytic Susceptibility in Vitro. *Ultrasound in Medicine & Biology*. Published online September 2018.
83. Nosaka M, Ishida Y, Kimura A, Kondo T. Time-dependent appearance of intrathrombus neutrophils and macrophages in a stasis-induced deep vein thrombosis model and its application to thrombus age determination. *Int J Legal Med*. 2009;123(3):235-240. doi:10.1007/s00414-009-0324-0
84. Mueller HS, Roberts R, Teichman SL, Sobel BE. Thrombolytic therapy in acute myocardial infarction: Part II--rt-PA. *Med Clin North Am*. 1989;73(2):387-407. doi:10.1016/s0025-7125(16)30679-4
85. Tsikouris JP, Tsikouris AP. A Review of Available Fibrin-Specific Thrombolytic Agents Used in Acute Myocardial Infarction. *Pharmacotherapy: The Journal of Human Pharmacology and Drug Therapy*. 2001;21(2):207-217. doi:https://doi.org/10.1592/phco.21.2.207.34103
86. Sikora-Skrabaka M, Skrabaka D, Ruggeri P, Caramori G, Skoczyński S, Barczyk A. D-dimer value in the diagnosis of pulmonary embolism—may it exclude only? *Journal of Thoracic Disease*. 2019;11(3). doi:10.21037/jtd.2019.02.88
87. Mirshahi M, Azzarone B, Soria J, Mirshahi F, Soria C. The role of fibroblasts in organization and degradation of a fibrin clot. *J Lab Clin Med*. 1991;117(4):274-281.
88. Tracy LE, Minasian RA, Caterson EJ. Extracellular Matrix and Dermal Fibroblast Function in the Healing Wound. *Adv Wound Care (New Rochelle)*. 2016;5(3):119-136. doi:10.1089/wound.2014.0561
89. Zorio E, Gilabert-Estellés J, España F, Ramón LA, Cosín R, Estellés A. Fibrinolysis: the key to new pathogenetic mechanisms. *Current Medicinal Chemistry*. 2008;15(9):923-929. doi:10.2174/092986708783955455
90. Detection of an unusually stable fibrinolytic inhibitor produced by bovine endothelial cells - PubMed. Accessed October 6, 2020. https://pubmed.ncbi.nlm.nih.gov/6574465/

91. Raimondo F, Azzaro MP, Palumbo GA, et al. Elevated vascular endothelial growth factor (VEGF) serum levels in idiopathic myelofibrosis. *Leukemia*. 2001;15(6):976-980. doi:10.1038/sj.leu.2402124
92. Bannish BE, Chernysh IN, Keener JP, Fogelson AL, Weisel JW. Molecular and Physical Mechanisms of Fibrinolysis and Thrombolysis from Mathematical Modeling and Experiments. *Sci Rep*. 2017;7. doi:10.1038/s41598-017-06383-w
93. Weisel JW, Litvinov RI. Mechanisms of fibrin polymerization and clinical implications. *Blood*. 2013;121(10):1712-1719. doi:10.1182/blood-2012-09-306639
94. Xie H, Kim K, Aglyamov SR, et al. Staging deep venous thrombosis using ultrasound elasticity imaging: Animal model. *Ultrasound in Medicine and Biology*. 2004;30(10):1385-1396. doi:10.1016/j.ultrasmedbio.2004.08.015
95. Xie H, Kim K, Aglyamov SR, et al. Correspondence of Ultrasound Elasticity Imaging to Direct Mechanical Measurement in Aging DVT in Rats. *Ultrasound Med Biol*. 2005;31(10):1351-1359. doi:10.1016/j.ultrasmedbio.2005.06.005
96. Emelianov SY, Chen X, O'Donnell M, et al. Triplex ultrasound: elasticity imaging to age deep venous thrombosis. *Ultrasound in Medicine & Biology*. 2002;28(6):757-767. doi:10.1016/S0301-5629(02)00516-1
97. Jain V, Abdulmalik O, Joy Propert K, Wehrli FW. Investigating the Magnetic Susceptibility Properties of Fresh Human Blood for Non Invasive Oxygen Saturation Quantification. *Magn Reson Med*. 2012;68(3):863-867. doi:10.1002/mrm.23282
98. Khokhlova VA, Fowlkes JB, Roberts WW, et al. Histotripsy methods in mechanical disintegration of tissue: Towards clinical applications. *International Journal of Hyperthermia*. 2015;31(2):145-162. doi:10.3109/02656736.2015.1007538
99. Xu Z, Ludomirsky A, Eun LY, et al. Controlled Ultrasound Tissue Erosion. *IEEE Transactions on Ultrasonics, Ferroelectrics and Frequency Control*. 2004;51(6):726-736. doi:10.1109/TUFFC.2004.1308731
100. Bader KB. The influence of medium elasticity on the prediction of histotripsy-induced bubble expansion and erythrocyte viability. *Phys Med Biol*. 2018;63(9):095010. doi:10.1088/1361-6560/aab79b
101. Maxwell AD, Wang T-Y, Cain CA, et al. Cavitation clouds created by shock scattering from bubbles during histotripsy. *The Journal of the Acoustical Society of America*. 2011;130(4):1888-1898. doi:10.1121/1.3625239
102. Vlaisavljevich E, Maxwell A, Mancia L, Johnsen E, Cain C, Xu Z. Visualizing the Histotripsy Process: Bubble Cloud-Cancer Cell Interactions in a Tissue-Mimicking Environment. *Ultrasound Med Biol*. 2016;42(10):2466-2477. doi:10.1016/j.ultrasmedbio.2016.05.018
103. Bader KB. The influence of medium elasticity on the prediction of histotripsy-induced bubble expansion and erythrocyte viability. *Physics in Medicine & Biology*. 2018;63(9):095010. doi:10.1088/1361-6560/aab79b
104. Hirsh J, Hoak J. Management of Deep Vein Thrombosis and Pulmonary Embolism : A Statement for Healthcare Professionals From the Council on Thrombosis (in Consultation With the Council on Cardiovascular Radiology), American Heart Association. *Circulation*. 1996;93(12):2212-2245. doi:10.1161/01.CIR.93.12.2212
105. Samani A, Zubovits J, Plewes D. Elastic moduli of normal and pathological human breast tissues: an inversion-technique-based investigation of 169 samples. *Physics in Medicine and Biology*. 2007;52(6):1565-1576. doi:10.1088/0031-9155/52/6/002

106. Duck FA, TotalBoox, TBX. *Physical Properties of Tissues.* Elsevier Science; 2013. Accessed September 20, 2018. http://www.totalboox.com/book/id-5258306496708787708
107. Vlaisavljevich E, Lin K-W, Warnez MT, et al. Effects of tissue stiffness, ultrasound frequency, and pressure on histotripsy-induced cavitation bubble behavior. *Phys Med Biol*. 2015;60(6):2271-2292. doi:10.1088/0031-9155/60/6/2271
108. Gyongy M, Arora M, Noble JA, Coussios CC. Use of passive arrays for characterization and mapping of cavitation activity during HIFU exposure. In: *2008 IEEE Ultrasonics Symposium*. IEEE; 2008:871-874. doi:10.1109/ULTSYM.2008.0210
109. Salgaonkar VA, Datta S, Holland CK, Mast TD. Passive cavitation imaging with ultrasound arrays. *The Journal of the Acoustical Society of America*. 2009;126(6):3071-3083. doi:10.1121/1.3238260
110. Jensen CR, Ritchie RW, Gyöngy M, Collin JRT, Leslie T, Coussios C-C. Spatiotemporal Monitoring of High-Intensity Focused Ultrasound Therapy with Passive Acoustic Mapping. *Radiology*. 2012;262(1):252-261. doi:10.1148/radiol.11110670
111. Haworth KJ, Salgaonkar VA, Corregan NM, Holland CK, Mast TD. Using Passive Cavitation Images to Classify High-Intensity Focused Ultrasound Lesions. *Ultrasound in Medicine & Biology*. 2015;41(9):2420-2434. doi:10.1016/j.ultrasmedbio.2015.04.025
112. Arvanitis CD, McDannold N. Integrated ultrasound and magnetic resonance imaging for simultaneous temperature and cavitation monitoring during focused ultrasound therapies: Simultaneous temperature and cavitation mapping. *Medical Physics*. 2013;40(11):112901. doi:10.1118/1.4823793
113. Choi JJ, Carlisle RC, Coviello C, Seymour L, Coussios C-C. Non-invasive and real-time passive acoustic mapping of ultrasound-mediated drug delivery. *Physics in Medicine and Biology*. 2014;59(17):4861-4877. doi:10.1088/0031-9155/59/17/4861
114. Haworth KJ, Raymond JL, Radhakrishnan K, et al. Trans-Stent B-Mode Ultrasound and Passive Cavitation Imaging. *Ultrasound in Medicine & Biology*. 2016;42(2):518-527. doi:10.1016/j.ultrasmedbio.2015.08.014
115. Coviello C, Kozick R, Choi J, et al. Passive acoustic mapping utilizing optimal beamforming in ultrasound therapy monitoring. *The Journal of the Acoustical Society of America*. 2015;137(5):2573-2585. doi:10.1121/1.4916694
116. Kwan JJ, Myers R, Coviello CM, et al. Ultrasound-Propelled Nanocups for Drug Delivery. *Small*. 2015;11(39):5305-5314. doi:10.1002/smll.201501322
117. Gateau J, Aubry J-F, Pernot M, Fink M, Tanter M. Combined passive detection and ultrafast active imaging of cavitation events induced by short pulses of high-intensity ultrasound. *IEEE Transactions on Ultrasonics, Ferroelectrics and Frequency Control*. 2011;58(3):517-532. doi:10.1109/TUFFC.2011.1836
118. Bader KB, Haworth KJ, Shekhar H, et al. Efficacy of histotripsy combined with rt-PA *in vitro*. *Physics in Medicine and Biology*. 2016;61(14):5253-5274. doi:10.1088/0031-9155/61/14/5253
119. Bader KB, Haworth KJ, Maxwell AD, Holland CK. Post Hoc Analysis of Passive Cavitation Imaging for Classification of Histotripsy-Induced Liquefaction in Vitro. *IEEE Transactions on Medical Imaging*. 2018;37(1):106-115. doi:10.1109/TMI.2017.2735238
120. Mercado-Shekhar KP, Kleven RT, Aponte Rivera H, et al. Effect of Clot Stiffness on Recombinant Tissue Plasminogen Activator Lytic Susceptibility in Vitro. *Ultrasound in Medicine & Biology*. 2018;44(12):2710-2727. doi:10.1016/j.ultrasmedbio.2018.08.005

121. Maxwell AD, Wang T-Y, Yuan L, Duryea AP, Xu Z, Cain CA. A Tissue Phantom for Visualization and Measurement of Ultrasound-Induced Cavitation Damage. *Ultrasound in Medicine & Biology*. 2010;36(12):2132-2143. doi:10.1016/j.ultrasmedbio.2010.08.023
122. Sutton JT, Ivancevich NM, Perrin SR, Vela DC, Holland CK. Clot retraction affects the extent of ultrasound-enhanced thrombolysis in an ex vivo porcine thrombosis model. *Ultrasound Med Biol*. 2013;39(5):813-824. doi:10.1016/j.ultrasmedbio.2012.12.008
123. Nightingale K. Acoustic Radiation Force Impulse (ARFI) Imaging: A Review. *Current Medical Imaging Reviews*. 2011;7(4):328-339. doi:10.2174/157340511798038657
124. Deng Y, Rouze NC, Palmeri ML, Nightingale KR. Ultrasonic Shear Wave Elasticity Imaging Sequencing and Data Processing Using a Verasonics Research Scanner. *IEEE Transactions on Ultrasonics, Ferroelectrics, and Frequency Control*. 2017;64(1):164-176. doi:10.1109/TUFFC.2016.2614944
125. Hall T. A Low Cost Compact 512 Channel Therapeutic Ultrasound System For Transcutaneous Ultrasound Surgery. In: *AIP Conference Proceedings*. Vol 829. AIP; 2006:445-449. doi:10.1063/1.2205514
126. Bader KB, Holland CK. Predicting the growth of nanoscale nuclei by histotripsy pulses. *Phys Med Biol*. 2016;61(7):2947-2966. doi:10.1088/0031-9155/61/7/2947
127. Haworth KJ, Bader KB, Rich KT, Holland CK, Mast TD. Quantitative Frequency-Domain Passive Cavitation Imaging. *IEEE Trans Ultrason, Ferroelect, Freq Contr*. 2017;64(1):177-191. doi:10.1109/TUFFC.2016.2620492
128. Szabo TL. *Diagnostic Ultrasound Imaging: Inside Out*. Second edition. Elsevier/AP, Academic Press is an imprint of Elsevier; 2014.
129. Otsu N. A Threshold Selection Method from Gray-Level Histograms. *IEEE Transactions on Systems, Man, and Cybernetics*. 1979;9(1):62-66. doi:10.1109/TSMC.1979.4310076
130. Haworth KJ, Bader KB, Rich KT, Holland CK, Mast TD. Quantitative Frequency-Domain Passive Cavitation Imaging. *IEEE Transactions on Ultrasonics, Ferroelectrics, and Frequency Control*. 2017;64(1):177-191. doi:10.1109/TUFFC.2016.2620492
131. Zweig MH, Campbell G. Receiver-operating characteristic (ROC) plots: a fundamental evaluation tool in clinical medicine. *Clin Chem*. 1993;39(4):561-577.
132. DeLong ER, DeLong DM, Clarke-Pearson DL. Comparing the areas under two or more correlated receiver operating characteristic curves: a nonparametric approach. *Biometrics*. 1988;44(3):837-845.
133. Holland CK, Apfel RE. An improved theory for the prediction of microcavitation thresholds. *IEEE Transactions on Ultrasonics, Ferroelectrics and Frequency Control*. 1989;36(2):204-208. doi:10.1109/58.19152
134. Madsen EL, Sathoff HJ, Zagzebski JA. Ultrasonic shear wave properties of soft tissues and tissuelike materials. *The Journal of the Acoustical Society of America*. 1983;74(5):1346-1355. doi:10.1121/1.390158
135. Vlaisavljevich E, Kim Y, Owens G, Roberts W, Cain C, Xu Z. Effects of tissue mechanical properties on susceptibility to histotripsy-induced tissue damage. *Physics in Medicine and Biology*. 2014;59(2):253-270. doi:10.1088/0031-9155/59/2/253
136. Lin K-W, Kim Y, Maxwell AD, et al. Histotripsy beyond the intrinsic cavitation threshold using very short ultrasound pulses: microtripsy. *IEEE Transactions on Ultrasonics, Ferroelectrics, and Frequency Control*. 2014;61(2):251-265. doi:10.1109/TUFFC.2014.6722611

137. Maxwell AD, Cain CA, Hall TL, Fowlkes JB, Xu Z. Probability of Cavitation for Single Ultrasound Pulses Applied to Tissues and Tissue-Mimicking Materials. *Ultrasound in Medicine & Biology*. 2013;39(3):449-465. doi:10.1016/j.ultrasmedbio.2012.09.004
138. Normand V, Lootens DL, Amici E, Plucknett KP, Aymard P. New Insight into Agarose Gel Mechanical Properties. *Biomacromolecules*. 2000;1(4):730-738. doi:10.1021/bm005583j
139. Barrangou LM, Daubert CR, Allen Foegeding E. Textural properties of agarose gels. I. Rheological and fracture properties. *Food Hydrocolloids*. 2006;20(2-3):184-195. doi:10.1016/j.foodhyd.2005.02.019
140. Bader KB, Crowe MJ, Raymond JL, Holland CK. Effect of Frequency-Dependent Attenuation on Predicted Histotripsy Waveforms in Tissue-Mimicking Phantoms. *Ultrasound in Medicine & Biology*. 2016;42(7):1701-1705. doi:10.1016/j.ultrasmedbio.2016.02.010
141. Wang T-Y, Xu Z, Hall TL, Fowlkes JB, Cain CA. An Efficient Treatment Strategy for Histotripsy by Removing Cavitation Memory. *Ultrasound in Medicine & Biology*. 2012;38(5):753-766. doi:10.1016/j.ultrasmedbio.2012.01.013
142. Rubin JM, Xie H, Kim K, et al. Sonographic elasticity imaging of acute and chronic deep venous thrombosis in humans. *J Ultrasound Med*. 2006;25(9):1179-1186.
143. Bader KB, Bollen V. The influence of gas diffusion on bubble persistence in shock-scattering histotripsy. *The Journal of the Acoustical Society of America*. 2018;143(6):EL481-EL486. doi:10.1121/1.5043081
144. Czaplicki C, Albadawi H, Partovi S, et al. Can thrombus age guide thrombolytic therapy? *Cardiovasc Diagn Ther*. 2017;7(Suppl 3):S186-S196. doi:10.21037/cdt.2017.11.05
145. Palta S, Saroa R, Palta A. Overview of the coagulation system. *Indian Journal of Anaesthesia*. 2014;58(5):515. doi:10.4103/0019-5049.144643
146. O'Reilly MA, Jones RM, Hynynen K. Three-Dimensional Transcranial Ultrasound Imaging of Microbubble Clouds Using a Sparse Hemispherical Array. *IEEE Transactions on Biomedical Engineering*. 2014;61(4):1285-1294. doi:10.1109/TBME.2014.2300838
147. Rich KT, Mast TD. Methods to calibrate the absolute receive sensitivity of single-element, focused transducers. *The Journal of the Acoustical Society of America*. 2015;138(3):EL193-EL198. doi:10.1121/1.4929620
148. Gray MD, Coussios CC. Broadband Ultrasonic Attenuation Estimation and Compensation With Passive Acoustic Mapping. *IEEE Transactions on Ultrasonics, Ferroelectrics, and Frequency Control*. 2018;65(11):1997-2011. doi:10.1109/TUFFC.2018.2866171
149. Kearon C, Kahn SR, Agnelli G, Goldhaber S, Raskob GE, Comerota AJ. Antithrombotic therapy for venous thromboembolic disease: American College of Chest Physicians Evidence-Based Clinical Practice Guidelines (8th Edition). *Chest*. 2008;133(6 Suppl):454S-545S. doi:10.1378/chest.08-0658
150. Bělohlávek J, Dytrych V, Linhart A. Pulmonary embolism, part I: Epidemiology, risk factors and risk stratification, pathophysiology, clinical presentation, diagnosis and nonthrombotic pulmonary embolism. *Exp Clin Cardiol*. 2013;18(2):129-138.
151. Righini M, Perrier A, De Moerloose P, Bounameaux H. D-Dimer for venous thromboembolism diagnosis: 20 years later. *J Thromb Haemost*. 2008;6(7):1059-1071. doi:10.1111/j.1538-7836.2008.02981.x
152. Wang C, Zhai Z, Yang Y, et al. Efficacy and Safety of Low Dose Recombinant Tissue-Type Plasminogen Activator for the Treatment of Acute Pulmonary Thromboembolism. *Chest*. 2010;137(2):254-262. doi:10.1378/chest.09-0765

153. Maxwell AD, Park S, Vaughan BL, Cain CA, Grotberg JB, Xu Z. Trapping of embolic particles in a vessel phantom by cavitation-enhanced acoustic streaming. *Phys Med Biol*. 2014;59(17):4927-4943. doi:10.1088/0031-9155/59/17/4927
154. Sakharov DV, Hekkenberg RT, Rijken DC. Acceleration of fibrinolysis by high-frequency ultrasound: the contribution of acoustic streaming and temperature rise. *Thromb Res*. 2000;100(4):333-340. doi:10.1016/s0049-3848(00)00319-4
155. Khokhlova TD, Wang Y-N, Simon JC, et al. Ultrasound-guided tissue fractionation by high intensity focused ultrasound in an in vivo porcine liver model. *PNAS*. 2014;111(22):8161-8166. doi:10.1073/pnas.1318355111
156. Schuster TG, Wei JT, Hendlin K, Jahnke R, Roberts WW. Histotripsy Treatment of Benign Prostatic Enlargement Using the Vortx Rx System: Initial Human Safety and Efficacy Outcomes. *Urology*. 2018;114:184-187. doi:10.1016/j.urology.2017.12.033
157. Devanagondi R, Zhang X, Xu Z, et al. Hemodynamic and Hematologic Effects of Histotripsy of Free-Flowing Blood: Implications for US-mediated Thrombolysis. *J Vasc Interv Radiol*. 2015;26(10):1559-1565. doi:10.1016/j.jvir.2015.03.022
158. Frenkel V, Oberoi J, Stone MJ, et al. Pulsed High-Intensity Focused Ultrasound Enhances Thrombolysis in an in Vitro Model. *Radiology*. 2006;239(1):86-93. doi:10.1148/radiol.2391042181
159. Zhang X, Owens GE, Gurm HS, Ding Y, Cain CA, Xu Z. Noninvasive thrombolysis using histotripsy beyond the intrinsic threshold (microtripsy). *IEEE Transactions on Ultrasonics, Ferroelectrics, and Frequency Control*. 2015;62(7):1342-1355. doi:10.1109/TUFFC.2015.007016
160. Zhang X, Owens GE, Cain CA, Gurm HS, Macoskey J, Xu Z. Histotripsy Thrombolysis on Retracted Clots. *Ultrasound Med Biol*. 2016;42(8):1903-1918. doi:10.1016/j.ultrasmedbio.2016.03.027
161. Holland CK, Vaidya SS, Datta S, Coussios C-C, Shaw GJ. Ultrasound-enhanced tissue plasminogen activator thrombolysis in an in vitro porcine clot model. *Thromb Res*. 2008;121(5):663-673. doi:10.1016/j.thromres.2007.07.006
162. Shaw GJ, Sperling M, Meunier JM. Long-term stability of recombinant tissue plasminogen activator at -80 C. *BMC Res Notes*. 2009;2(1):117. doi:10.1186/1756-0500-2-117
163. Maxwell AD, Haworth KJ, Holland CK, Bader KB. Design of a focused ultrasound transducer for histotripsy-thrombolytic combination therapy. *The Journal of the Acoustical Society of America*. 2019;145(3):1747-1747. doi:10.1121/1.5101404
164. Maxwell AD, Yuldashev PV, Kreider W, et al. A Prototype Therapy System for Transcutaneous Application of Boiling Histotripsy. *IEEE Trans Ultrason Ferroelectr Freq Control*. 2017;64(10):1542-1557. doi:10.1109/TUFFC.2017.2739649
165. Jensen CT, Chahin A, Amin VD, et al. Qualitative Slow Blood Flow in Lower Extremity Deep Veins on Doppler Sonography: Quantitative Assessment and Preliminary Evaluation of Correlation With Subsequent Deep Venous Thrombosis Development in a Tertiary Care Oncology Center. *J Ultrasound Med*. 2017;36(9):1867-1874. doi:10.1002/jum.14220
166. Hilleman DE, Razavi MK. Clinical and economic evaluation of the Trellis-8 infusion catheter for deep vein thrombosis. *J Vasc Interv Radiol*. 2008;19(3):377-383. doi:10.1016/j.jvir.2007.10.027
167. Bader K, Hendley SA, Bollen V. Assessment of Collaborative Robot (Cobot)-Assisted Histotripsy for Venous Clot Ablation. *IEEE Trans Biomed Eng*. 2020;PP. doi:10.1109/TBME.2020.3023630

168. Datta S, Coussios C-C, McAdory LE, et al. CORRELATION OF CAVITATION WITH ULTRASOUND ENHANCEMENT OF THROMBOLYSIS. *Ultrasound Med Biol*. 2006;32(8):1257-1267. doi:10.1016/j.ultrasmedbio.2006.04.008
169. Drabkin DL, Austin JH. Spectrophotometric Studies Ii. Preparations from Washed Blood Cells; Nitric Oxide Hemoglobin and Sulfhemoglobin. *J Biol Chem*. 1935;112(1):51-65.
170. Kaufmann J, Schering AG. Analysis of Variance ANOVA. In: *Wiley StatsRef: Statistics Reference Online*. American Cancer Society; 2014. doi:10.1002/9781118445112.stat06938
171. Tukey JW. Comparing Individual Means in the Analysis of Variance. *Biometrics*. 1949;5(2):99-114. doi:10.2307/3001913
172. Laplace P. *Théorie analytique des probabilités*. Courcier; 1820.
173. Hendley SA, Bollen V, Anthony GJ, Paul JD, Bader KB. In vitro assessment of stiffness-dependent histotripsy bubble cloud activity in gel phantoms and blood clots. *Phys Med Biol*. 2019;64(14):145019. doi:10.1088/1361-6560/ab25a6
174. Rich KT, Holland CK, Rao MB, Mast TD. Characterization of cavitation-radiated acoustic power using diffraction correction. *J Acoust Soc Am*. 2018;144(6):3563. doi:10.1121/1.5083831
175. Wang Y-N, Khokhova TD, Buravkov S, et al. MECHANICAL DECELLULARIZATION OF TISSUE VOLUMES USING BOILING HISTOTRIPSY. *Phys Med Biol*. 2018;63(23):235023. doi:10.1088/1361-6560/aaef16
176. Xu Z, Fan Z, Hall TL, Winterroth F, Fowlkes JB, Cain CA. Size Measurement of Tissue Debris Particles Generated from Pulsed Ultrasound Cavitational Therapy – Histotripsy. *Ultrasound Med Biol*. 2009;35(2):245-255. doi:10.1016/j.ultrasmedbio.2008.09.002
177. Nyamekye I, Merker L. Management of proximal deep vein thrombosis. *Phlebology*. 2012;27 Suppl 2:61-72. doi:10.1258/phleb.2012.012s37
178. Jahanpanah N, Sharma S, Mercado-Shekhar KP, et al. Hemolysis resulting from acoustic droplet vaporization and inertial cavitation. *Proc Mtgs Acoust*. 2019;36(1):020001. doi:10.1121/2.0001240
179. Vlaisavljevich E, Durmaz YY, Maxwell A, Elsayed M, Xu Z. Nanodroplet-mediated histotripsy for image-guided targeted ultrasound cell ablation. *Theranostics*. 2013;3(11):851-864. doi:10.7150/thno.6717
180. Bajd F, Serša I. A Concept of Thrombolysis as a Corrosion–Erosion Process Verified by Optical Microscopy. *Microcirculation*. 2012;19(7):632-641. doi:10.1111/j.1549-8719.2012.00198.x
181. Chao FC, Tullis JL, Kenney DM, Conneely GS, Doyle JR. Concentration effects of platelets, fibrinogen and thrombin on platelet aggregation and fibrin clotting. *Thromb Diath Haemorrh*. 1974;32(1):216-231.
182. Hall T, Cain C. A Low Cost Compact 512 Channel Therapeutic Ultrasound System For Transcutaneous Ultrasound Surgery. *AIP Conference Proceedings*. 2006;829(1):445-449. doi:10.1063/1.2205514
183. Stoica P, Zhisong Wang, Jian Li. Robust Capon beamforming. *IEEE Signal Processing Letters*. 2003;10(6):172-175. doi:10.1109/LSP.2003.811637
184. Haynes W. Wilcoxon Rank Sum Test. In: Dubitzky W, Wolkenhauer O, Cho K-H, Yokota H, eds. *Encyclopedia of Systems Biology*. Springer; 2013:2354-2355. doi:10.1007/978-1-4419-9863-7_1185
185. Miller RGJ. *Simultaneous Statistical Inference*. 2nd ed. Springer-Verlag; 1981. doi:10.1007/978-1-4613-8122-8

186. Brenner B, Francis CW, Totterman S, et al. Quantitation of venous clot lysis with the D-dimer immunoassay during fibrinolytic therapy requires correction for soluble fibrin degradation. *Circulation*. 1990;81(6):1818-1825. doi:10.1161/01.cir.81.6.1818
187. Ouriel K, Greenberg RK, Green RM, Massullo JM, Goines DR. A volumetric index for the quantification of deep venous thrombosis. *Journal of Vascular Surgery*. 1999;30(6):1060-1066. doi:10.1016/S0741-5214(99)70044-3
188. Keiler J, Seidel R, Wree A. The femoral vein diameter and its correlation with sex, age and body mass index – An anatomical parameter with clinical relevance. *Phlebology*. 2019;34(1):58-69. doi:10.1177/0268355518772746
189. Walker JB, Nesheim ME. The Molecular Weights, Mass Distribution, Chain Composition, and Structure of Soluble Fibrin Degradation Products Released from a Fibrin Clot Perfused with Plasmin. *J Biol Chem*. 1999;274(8):5201-5212. doi:10.1074/jbc.274.8.5201
190. Mercado-Shekhar KP, Kleven RT, Rivera HA, et al. Effect of Clot Stiffness on Recombinant Tissue Plasminogen Activator Lytic Susceptibility in Vitro. *Ultrasound in Medicine and Biology*. 2018;44(12):2710-2727. doi:10.1016/j.ultrasmedbio.2018.08.005
191. Chinnadurai P, Bismuth J. Intraoperative Imaging and Image Fusion for Venous Interventions. *Methodist Debakey Cardiovasc J*. 2018;14(3):200-207. doi:10.14797/mdcj-14-3-200
192. Rogers T, Ratnayaka K, Lederman RJ. MRI Catheterization in Cardiopulmonary Disease. *Chest*. 2014;145(1):30-36. doi:10.1378/chest.13-1759
193. Allen SP, Hernandez-Garcia L, Cain CA, Hall TL. MR-based detection of individual histotripsy bubble clouds formed in tissues and phantoms. *Magnetic Resonance in Medicine*. 2016;76(5):1486-1493. doi:https://doi.org/10.1002/mrm.26062
194. Linkins L-A, Pasquale P, Paterson S, Kearon C. Change in Thrombus Length on Venous Ultrasound and Recurrent Deep Vein Thrombosis. *Arch Intern Med*. 2004;164(16):1793. doi:10.1001/archinte.164.16.1793
195. Vlaisavljevich E, Gerhardson T, Hall T, Xu Z. Effects of F-Number on the Histotripsy Intrinsic Threshold and Cavitation Bubble Cloud Behavior. *Phys Med Biol*. 2017;62(4):1269-1290. doi:10.1088/1361-6560/aa54c7
196. Rosnitskiy PB, Yuldashev PV, Sapozhnikov OA, et al. Design of HIFU transducers for generating specified nonlinear ultrasound fields. *IEEE Trans Ultrason Ferroelectr Freq Control*. 2017;64(2):374-390. doi:10.1109/TUFFC.2016.2619913
197. Cesari M, Pahor M, Incalzi RA. PLASMINOGEN ACTIVATOR INHIBITOR-1 (PAI-1): A KEY FACTOR LINKING FIBRINOLYSIS AND AGE-RELATED SUBCLINICAL AND CLINICAL CONDITIONS. *Cardiovasc Ther*. 2010;28(5):e72-e91. doi:10.1111/j.1755-5922.2010.00171.x
198. Morrow GB, Whyte CS, Mutch NJ. Functional plasminogen activator inhibitor 1 is retained on the activated platelet membrane following platelet activation. *Haematologica*. 2020;105(12):2824-2833. doi:10.3324/haematol.2019.230367
199. Katori N, Tanaka KA, Szlam F, Levy JH. The Effects of Platelet Count on Clot Retraction and Tissue Plasminogen Activator-Induced Fibrinolysis on Thrombelastography. *Anesthesia & Analgesia*. 2005;100(6):1781-1785. doi:10.1213/01.ANE.0000149902.73689.64
200. Petrov Victor V., Fagard Robert H., Lijnen Paul J. Stimulation of Collagen Production by Transforming Growth Factor-β1 During Differentiation of Cardiac Fibroblasts to Myofibroblasts. *Hypertension*. 2002;39(2):258-263. doi:10.1161/hy0202.103268

201. Gharaee-Kermani M, Denholm EM, Phan SH. Costimulation of fibroblast collagen and transforming growth factor beta1 gene expression by monocyte chemoattractant protein-1 via specific receptors. *J Biol Chem*. 1996;271(30):17779-17784. doi:10.1074/jbc.271.30.17779
202. Passman MA, McLafferty RB, Lentz MF, et al. Validation of Venous Clinical Severity Score (VCSS) with other venous severity assessment tools from the American Venous Forum, National Venous Screening Program. *J Vasc Surg*. 2011;54(6 Suppl):2S-9S. doi:10.1016/j.jvs.2011.05.117
203. Lewis JH. *Comparative Hemostasis in Vertebrates*. Springer US; 1996. doi:10.1007/978-1-4757-9768-8
204. Giger ML. Machine Learning in Medical Imaging. *Journal of the American College of Radiology*. 2018;15(3, Part B):512-520. doi:10.1016/j.jacr.2017.12.028